AALBORG UNIVERSITY
STUDENT REPORT

Masters thesis

Dual-band S- and X-band antenna for nano-satellites

Authors:

Robin Jess Williams

Daniel Edelgaard Serup

University Supervisor:
Shuai Zhang

Company supervisor:
Boyan Yanakiev

AALBORG UNIVERSITY
STUDENT REPORT

Wireless Communication Systems
Aalborg University
http://www.aau.dk

Title:
Dual-band S- and X-band antenna for nano-satellites

Theme:
Planar nano-satellite antenna design

Project Period:
Autumn 2018 -
Spring 2019

Project Group:
Group WCS 10-950

Participants:
Daniel Edelgaard Serup
Robin Jess Williams

University Supervisor:
Shuai Zhang

Company Supervisor:
Boyan Yanakiev

Number of Pages: 128

Date of Completion: June 31, 2019

Abstract:

This masters thesis designs, assembles, and testes two dual-band S- and X-band 1U nano-satellite antennas.
The antenna size is limited to a nano-satellite 1 U face of 100 by 100 mm. This makes the design a problem of finding a good compromise between S- and X-band performance or methods of sharing volume without sacrificing isolation.
Two different dual-band antenna topologies are used to propose two different antenna designs. The performance of the two proposed antenna designs is evaluated by simulations and measurements of assembled prototypes of the two antenna designs. The two prototype antennas are measured using a network analyzer and in an anechoic chamber. One antenna design shows good measured performance whilst the other shows a more lossy and inferior performance.
The measurements show one of the antenna prototype designs has a realized right hand circularly polarized gain of ≥ 6.0 dB in the S-band frequency range 2.00 to 2.12 GHz and a realized right hand circularly polarized gain of ≥ 12 dB in the X-band frequency range 8.2 to 9.0 GHz. The impedance bandwidth of both frequency bands exceeds these frequency ranges.
With the satisfactory measurement results, one of the proposed designs fulfils the set requirements for a dual-band S- and X-band 1 U nano-satellite antenna.

PREFACE

This student project is composed by Daniel E. Serup and Robin J. Williams during the 9th and 10th semester of the wireless communication systems masters programme at Aalborg University as part of a long master thesis.

This work is conducted in collaboration with the nano-satellite company GOMSpace.

For citations, the report employs the IEEE referencing method. If citations are not present by figures or tables, these are made by the authors of the report. Units are indicated according to the SI system.

References done with a number in square brackets are put before the punctuation for the statement they support. If a reference is just after punctuation it supports the entire paragraph. Some equations will be referenced with a reference page or equation number for the convenience of the reader.

Throughout this thesis, the Computer Simulation Technology (CST) simulation tool is used. For this thesis, the default CST 2018 mesh settings are chosen and will be used unless otherwise stated. The global mesh settings has however been increased to 30 cells per wavelength for all simulations in Chapters 5 and 6 to achieve accurate simulation results. A visual inspection of the mesh grid is used to determine if local mesh properties should be enforced to ensure accurate results. All simulations are allowed a simulation duration such that an accuracy of $-40\,\mathrm{dB}$ can be guaranteed, this is archived by increasing the simulation duration under special settings.

Aalborg University, June 5, 2019

Daniel Edelgaard Serup
<dserup14@student.aau.dk>

Robin Jess Williams
<rwilli14@student.aau.dk>

TABLE OF CONTENTS

1 INTRODUCTION

Mankind has always been fascinated by space exploration. The satellite and space industry is rapidly growing to meet the market demands for space exploration technology. In recent years the demand for smaller nano-satellites has grown significantly. This is because the smaller satellites have some advantages compared to bigger satellites.

Nano-satellites weigh between 1 to 10 kg and their size is usually denoted in units, where 1 U is one 1 dm^3 cube. Nano-satellites are often constructed from between one to eight units. Nano-satellites are typically put in low orbits, at altitudes between 450 to 600 km. This altitude results in 14 and 16 orbits a day and good conditions for earth observations and communication applications. [1]

Figure 1.1 shows an illustration of four 1 U nano-satellites orbiting the earth.Most of the sides of the satellites are covered by solar panels.

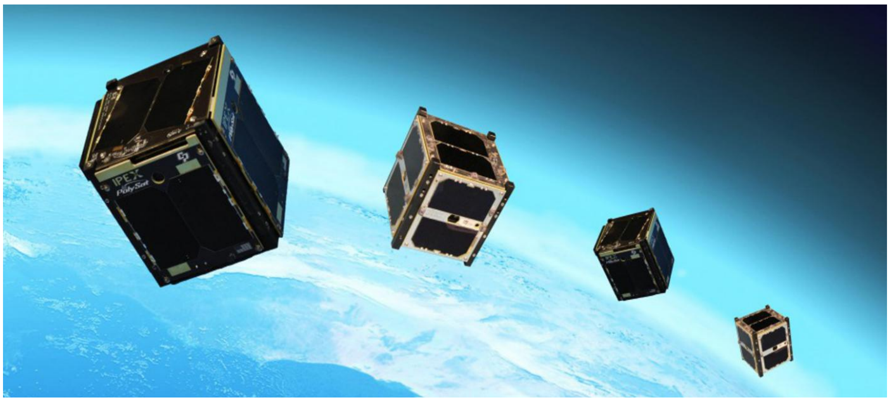

Figure 1.1: Illustration of four small nano-satellites orbiting earth [2].

One advantage of the smaller satellites is their lowered launch expenses due to their small footprint. Examples of nano-satellite applications are tracking of ships and airplanes in critical areas such as the Atlantic ocean, cattle tracing in remote rural areas, and delivering communications network coverage to remote areas or in cases of emergency. Demands for nano-satellites with high data transfer speeds between satellites and ground stations are increasing. Higher data rates are important for many new use-cases of nano-satellites, such as cellular networking.

One of the key components of a nano-satellite is its communication system. The system should be efficiency due to the limited available power, and should ensure a communication link between the satellite and the ground station that supports the required data rate.

GOMSpace is a company that specializes in both nano-satellite design and manufacturing. They currently have satellite applications that use two antennas modules to establish the satellite-earth communication link. An S-band antenna for the communication uplink and an X-band antenna for the communication downlink. [3]

The cost of launching a satellite into space is a big portion of the cost of deploying a satellite. Therefore, reducing physical size and weight is a design parameter of high importance. To accommodate this goal of reducing the total cost of the satellite it would be beneficial to combine the two aforementioned S- and X-band antennas into one single product capable of supporting both frequency bands.

In general only a limited amount of space is allocated to the antennas, as it is also seen from Figure 1.1, where the four satellites are almost entirely covered by solar panels. Therefore it would be very beneficial to reduce the antenna surface area. This could potentiality reduce the volume of the satellite or allow for more space to be used for cameras or solar panels.

The objective of this thesis is to design a dual-band antenna solution. The antenna should enable uplink and downlink in the S- and X-band respectively. The focus of this thesis is:

Design of dual-band S- and X-band antennas for nano-satellites

The antenna has to comply with a variety of requirements and specifications. For space applications, it is typical to have both electrical, mechanical, and environmental requirements. The antenna must be tested to ensure it satisfies the specified requirements.

Many different nano-satellite antenna designs have been proposed, among these are very high gain deployable antennas with gains above for example 20 dB in the X-band [4, 5]. Deployable antennas are both mechanical and electrical challenges, and ensuring reliable deployment becomes a big part of the design. To limit the scope of this thesis, it is chosen to focus entirely on non-deployable planar antennas as to keep the focus of the thesis to electrical design.

The remainder of this masters thesis is structured as follows:
Chapter 2 investigates relevant antenna theory and antenna performance metrics. Chapter 3 presents a short state of the art literature study.
Chapters 4 to 6 presents antenna requirements and design.
Chapters 7 to 9 cover prototyping, a measurement campaign, and considerations in regards to satellite installation.
Lastly, a discussion and conclusion in Chapters 10 and 11 finalize the work of this masters thesis.

2 ANTENNA THEORY

This chapter presents the antenna theory relevant for this master thesis. The chapter presents different antenna performance metrics that are used in this thesis to evaluate the performance of antenna prototypes. The later parts of this chapter summarizes patch antenna design and principals because patch antenna designs are proposed later in this thesis.

2.1 COORDINATE SYSTEM

A spherical coordinate system is convenient when describing the radiation behaviour of an antenna. A coordinate system can be defined and oriented differently. For the entirety of this thesis, the coordinate system is defined according to IEEE standards [6].

Figure 2.1 shows the chosen coordinate system. With points distributed linearly on the θ and ϕ axis, the point density is highest at the poles and lowest at the equator. Directional antennas are oriented with the radiation pointing in the Y-axis direction unless otherwise indicated ($\theta = 90°$ and $\phi = 90°$).

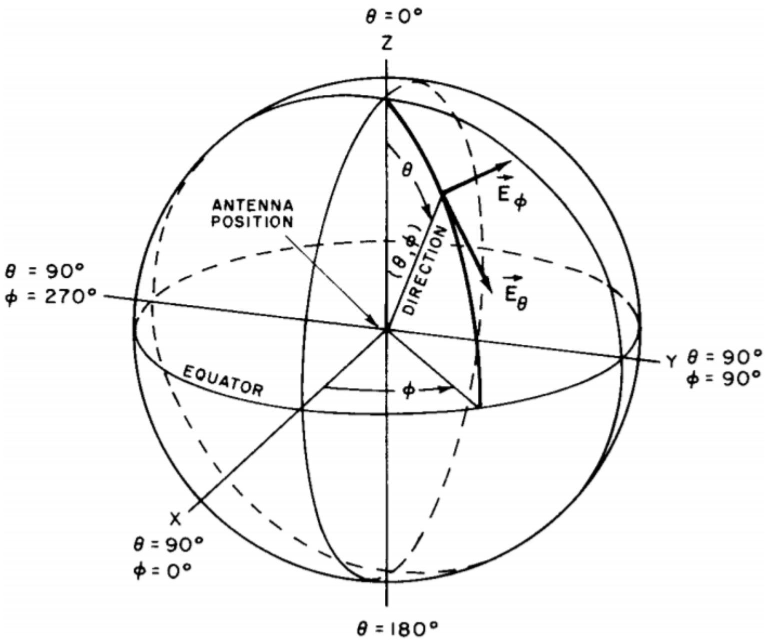

Figure 2.1: Illustration of the IEEE spherical coordinate system [6, p. 5].

2.2 S-PARAMETERS AND RETURN LOSS

The S-parameters are used to describe the behaviour of electrical circuits such as amplifiers, filters, and antennas. With antennas, the S-parameters are used to describe the return loss caused by impedance mismatch at the antenna input port. In structures with multiple antenna elements, the S-parameters are also used to describe the cross-coupling between different antenna ports.

S-parameters are defined by Equation (2.1). The condition $V_k^+ = 0 \ \forall \ k \neq m$ means that all ports, except port m, have to be terminated in a matched loads.

$$\mathrm{S}_{nm} = \left. \frac{V_n^-}{V_m^+} \right|_{\mathrm{V_k^+=0 \ \forall \ k \neq m}} \qquad [1] \quad (2.1)$$

Where:

V_n^-	=	outgoing wave at port n	[V]
V_m^+	=	ingoing wave at port m	[V]

As an example, Figure 2.2 shows a diagram of a two-port network. The reflection coefficients are given by Equations (2.2) and (2.3) [7, p. 197].

$$\Gamma_1 = \mathrm{S}_{11} + \frac{\mathrm{S}_{12}\mathrm{S}_{21}\Gamma_{\mathrm{p2}}}{1 - \mathrm{S}_{22}\Gamma_{\mathrm{p2}}} \qquad [1] \quad (2.2)$$

$$\Gamma_2 = \mathrm{S}_{22} + \frac{\mathrm{S}_{12}\mathrm{S}_{21}\Gamma_{\mathrm{p1}}}{1 + \mathrm{S}_{11}\Gamma_{\mathrm{p1}}} \qquad [1] \quad (2.3)$$

Where:

S_{nm}	=	the S-parameter from port m to port n	[1]
Γ_n	=	reflection coefficient looking into the network from port n	[1]
Γ_{pn}	=	reflection coefficient looking into port n from the network	[1]

Equations (2.2) and (2.3) illustrate the difference between the S_{nn}-parameters and reflection coefficients. The reflection coefficient is only equal the S_{nn}-parameter if the other ports are terminated in matched loads. The reflection coefficient observed depends on the application of the network, whereas the S-parameters are constant.

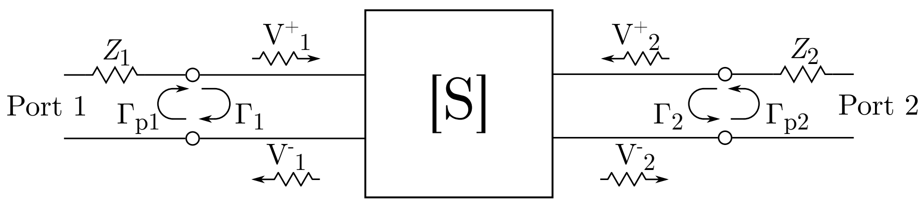

Figure 2.2: Diagram showing a two-port network. Γ_n is the n'th reflection coefficient, V_n^+ and V_n^- are the in- and outgoing waves of port n respectively.

The time-averaged power accepted by the network from port n is given by Equation (2.4). [7, p. 57]

$$P_{\mathrm{in,n}} = \frac{\left(|V_n^+|^2 - |V_n^-|^2\right)}{2Z_n} = \frac{|V_n^+|^2}{2Z_n}\left(1 - |\Gamma_n|^2\right) \qquad [\mathrm{W}] \quad (2.4)$$

Equation (2.4) shows that $|\Gamma_n|^2$ is the fraction of power reflected out of the system.

This reflected power is regarded as a loss, called the return loss, and is often measured in dB: $\mathrm{RL}_n = -20\log_{10}\left(|\Gamma_n|\right)$ [7, p. 58]. A return loss $\mathrm{RL} = 0\,\mathrm{dB}$ indicates that no power is accepted by the network and a return loss $\mathrm{RL} = \infty$ indicates that all the supplied power is accepted by the network.

If all ports or the network are perfectly matched in a given application, the S_{nn} parameter is equal the reflection coefficient Γ_n. In this case, the return loss simplifies to Equation (2.5).

$$RL = -20 \cdot \log_{10}(|S_{nn}|) \qquad \text{[dB]} \quad (2.5)$$

2.2.1 IMPEDANCE BANDWIDTH

The impedance bandwidth is a performance metric based on the frequency dependency of the return loss. Impedance bandwidth is defined as either the absolute or fractional bandwidth relative to a center frequency, in which the return loss $\mathrm{RL}_n \geq p$, where p is a set threshold.

In this thesis, the threshold is chosen as $\mathrm{RL}_n \geq 10\,\mathrm{dB} \implies \mathrm{S}_{nn} \leq -10\,\mathrm{dB}$. Thus the impedance bandwidth is the bandwidth in which the reflection coefficient S_{nn} is below $-10\,\mathrm{dB}$.

2.3 ANTENNA EFFICIENCY

Antenna efficiency is a measure of how efficient an antenna accepts and radiates supplied power. While antenna efficiency is often not used directly as a performance metric, it directly affects the realized gain of the antenna, as presented in Section 2.5.

The total efficiency of an antenna is split into multiple parts dependent on the cause of the loss. The total antenna efficiency is given by Equation (2.6).

$$e_0 = e_r \cdot e_c \cdot e_d \qquad [1] \quad (2.6)$$

Where:

e_0	=	total antenna efficiency	[1]
e_r	=	reflection efficiency	[1]
e_c	=	conduction efficiency	[1]
e_d	=	dielectric efficiency	[1]

As per Section 2.2, the reflection efficiency is defined as expressed in Equation (2.7).

$$e_r = 1 - |\Gamma|^2 \qquad [1] \quad (2.7)$$

Where:

Γ	=	reflection coefficient	[1]

The reflection coefficient Γ at the interface between two networks can be calculated by Equation (2.8) [7, eq. (2.35)].

$$\Gamma = \frac{Z_{\text{in}} - Z_0}{Z_{\text{in}} + Z_0} \qquad [1] \quad (2.8)$$

Where:

Z_{in}	=	load impedance	[1]
Z_0	=	source impedance	[1]

The conduction and dielectric efficiency details the fraction of the power converted to heat in the dielectric and conductor as a wave propagates through the antenna. In practice, they are difficult to distinguish so they are here denoted as a single constant $e_{cd} = e_c \cdot e_d$.

2.4 POLARIZATION

Polarization is a way to characterize the orientation of the fields in electromagnetic radiation. Three classifications of polarisation exist: Linear, circular, and elliptical. Linear and circular are special cases of elliptical.

The polarization is said to be linear if the time-dependent electrical field vector only varies along a single axis.

For circular polarisation, the magnitudes of the two angular components should be equal in strength and the phase difference between the components has to be an odd multiple of $\frac{\pi}{2}$rad.

The circular polarization can either be Right Hand Circular Polarized (RHCP) or Left Hand Circular Polarized (LHCP). An antenna is LHCP if the electrical field vector rotates clockwise along the direction of propagation, and RHCP if the vector rotates counterclockwise. Alternatively, the surface current of the antenna can be considered. Counterclockwise rotation of the surface current indicates a RHCP antenna.

2.5 ANTENNA DIRECTIVITY, GAIN, AND AXIAL RATIO

If an antenna radiates a continuous sine-wave with arbitrary polarization, the complex representation of the E- and H-fields at a given point in the farfield, can be written as Equations (2.9) and (2.10). In the farfield the radial field components are approximately zero [8].

The field components are highly frequency dependent, but this is omitted from the following equations for notational simplicity.

$$\bar{\mathbf{E}}(r,\theta,\phi,t) = \begin{bmatrix}0 & E_\theta(r,\theta,\phi,t) & E_\phi(r,\theta,\phi,t)\end{bmatrix}^T \qquad [\mathrm{V\,m^{-1}}] \tag{2.9}$$

$$\bar{\mathbf{H}}(r,\theta,\phi,t) = \begin{bmatrix}0 & -E_\phi(r,\theta,\phi,t) & E_\theta(r,\theta,\phi,t)\end{bmatrix}^T \frac{1}{\eta} \qquad [\mathrm{A\,m^{-1}}] \tag{2.10}$$

Where:

E_n	=	$A_n(r,\theta,\phi)\cdot \mathrm{e}^{j\left(\omega t+\varphi_n\right)}$	$\left[\mathrm{V\,m^{-1}}\right]$
η	=	the impedance of free space	$[\Omega]$
x^T	=	transpose of x	[1]

The total instantaneous and total time-averaged surface power density are given by Equations (2.11) and (2.12) respectively.

$$\begin{aligned}\bar{\mathbf{W}}(r,\theta,\phi,t) &= \mathrm{Re}\left(\bar{\mathbf{E}}\right) \times \mathrm{Re}\left(\bar{\mathbf{H}}\right) = \begin{bmatrix}\mathrm{Re}\left(E_\theta\right)^2 + \mathrm{Re}\left(E_\phi\right)^2 \\ 0 \\ 0\end{bmatrix}\frac{1}{\eta} \\ &= \begin{bmatrix}\frac{A_\theta^2+A_\phi^2}{2} + \frac{A_\theta^2\cos\left(2\left(\omega t+\varphi_\theta\right)\right)+A_\phi^2\cos\left(2\left(\omega t+\varphi_\phi\right)\right)}{2} \\ 0 \\ 0\end{bmatrix}\frac{1}{\eta} \qquad [\mathrm{W\,m^{-2}}]\end{aligned} \tag{2.11}$$

$$W_A(r,\theta,\phi) = \frac{A_\theta^2 + A_\phi^2}{2\eta} = \frac{|E_\theta|^2 + |E_\phi|^2}{2\eta} \qquad [\mathrm{W\,m^{-2}}] \tag{2.12}$$

The amplitudes A_θ and A_ϕ together with the phases φ_θ and φ_ϕ determines the polarization. For linear polarization, the radial components are in-phase or counter-phase $\varphi_\phi = \varphi_\theta + n\pi$. For circular polarization, the radial components are orthogonal $\varphi_\phi = \varphi_\theta + \frac{\pi}{2} + n\pi$ and has equal amplitudes $A_\theta = A_\phi$

For a given rotation angle φ the E-field can be represented as a parallel and orthogonal component shown in Equation (2.13).

A linearly polarized antenna only receives and transmits in the parallel component, discarding the orthogonal component. The linearly polarized time-averaged surface power density is therefore given by Equation (2.14).

$$\bar{\mathbf{E}}_L(r,\theta,\phi,t) = \begin{bmatrix} 0 \\ \cos(\varphi)\, E_\phi(r,\theta,\phi,t) + \sin(\varphi)\, E_\theta(r,\theta,\phi,t) \\ \sin(\varphi)\, E_\phi(r,\theta,\phi,t) - \cos(\varphi)\, E_\theta(r,\theta,\phi,t) \end{bmatrix} \quad [\mathrm{V\,m^{-1}}] \quad (2.13)$$

$$W_L(r,\theta,\phi) = \frac{|\cos(\varphi)\, E_\phi(r,\theta,\phi,t) + \sin(\varphi)\, E_\theta(r,\theta,\phi,t)|^2}{2\eta} \quad [\mathrm{W\,m^{-2}}] \quad (2.14)$$

Similarly, for circular polarization, the E-field can be expressed as two orthogonal circular components as given in Equations (2.15) and (2.16). The circular E-field vector is then given by Equation (2.17). As with linearly polarized antennas, RHCP antennas only receive and transmit in the RHCP component, discarding the LHCP component, and vice versa. The RHCP time-averaged surface power density is therefore given by Equation (2.18)

$$E_{\mathrm{RC}}(r,\theta,\phi,t) = \frac{\mathrm{e}^{j0}}{\sqrt{2}} E_\theta(r,\theta,\phi,t) + \frac{\mathrm{e}^{-j\frac{\pi}{2}}}{\sqrt{2}} E_\phi(r,\theta,\phi,t) \quad [\mathrm{V\,m^{-1}}] \quad (2.15)$$

$$E_{\mathrm{LC}}(r,\theta,\phi,t) = \frac{\mathrm{e}^{j0}}{\sqrt{2}} E_\theta(r,\theta,\phi,t) + \frac{\mathrm{e}^{j\frac{\pi}{2}}}{\sqrt{2}} E_\phi(r,\theta,\phi,t) \quad [\mathrm{V\,m^{-1}}] \quad (2.16)$$

$$\bar{\mathbf{E}}_C(r,\theta,\phi,t) = \begin{bmatrix} 0 & E_{\mathrm{RC}}(r,\theta,\phi,t) & E_{\mathrm{LC}}(r,\theta,\phi,t) \end{bmatrix}^T \quad [\mathrm{V\,m^{-1}}] \quad (2.17)$$

$$W_{\mathrm{RC}}(r,\theta,\phi) = \frac{|E_{\mathrm{RC}}(r,\theta,\phi,t)|^2}{2\eta} \quad [\mathrm{W\,m^{-2}}] \quad (2.18)$$

Based on Equation (2.14) it can be derived that if the field is linearly polarized ($\varphi_\theta = \varphi_\phi$), the linearly polarized time-averaged surface power density varies from 0 to $W_A(r,\theta,\phi)$ as the rotation angle φ varies. This means that rotational alignment is very important for linearly polarized antenna systems.

The circularly polarized time-averaged surface power density of a linearly polarized field is however independent of the rotation φ and has value $\frac{W_A(r,\theta,\phi)}{2}$. Receiving a linearly polarized field with a circularly polarized antenna and vice versa introduces a 3 dB polarization loss.

AXIAL RATIO

Axial ratio is a metric describing how pure the polarization of the field radiated by an antenna is. Axial ratio is given by Equation (2.19) [8, eq. (2-65)]. The major axis E-field is the maximum linear E-field component obtained when scanning the rotation angle φ and the minor axis is its orthogonal component.

$$\mathrm{AR} = \frac{E_{\text{major}}}{E_{\text{minor}}} = \sqrt{\frac{A_\theta^2 + A_\phi^2 + \sqrt{A_\theta^4 + A_\phi^4 + 2A_\theta^2 A_\phi^2 \cos\left(2\left(\varphi_\theta - \varphi_\phi\right)\right)}}{A_\theta^2 + A_\phi^2 - \sqrt{A_\theta^4 + A_\phi^4 + 2A_\theta^2 A_\phi^2 \cos\left(2\left(\varphi_\theta - \varphi_\phi\right)\right)}}} \quad [1] \quad (2.19)$$

Where:

A_x	=	amplitude of the x E-field component	$\left[\mathrm{V\,m^{-1}}\right]$
φ_x	=	phase of the x E-field component	$\left[\mathrm{V\,m^{-1}}\right]$
E_{major}	=	amplitude of major axis E-field	$\left[\mathrm{V\,m^{-1}}\right]$
E_{minor}	=	amplitude of minor axis E-field	$\left[\mathrm{V\,m^{-1}}\right]$

If the axial ratio is 1, the field is perfectly circularly polarized. If the axial ratio is ∞, the field is perfectly linearly polarized.

RADIATION INTENSITY

Since radiation in free space is spherical, the surface power density $W_x \propto \frac{1}{r^2}$ as the surface area of a sphere is $A_{\text{sphere}} = 4\pi r^2$.

The radiation intensity is defined as the surface power per unit solid angle and is given by Equation (2.20) [8].

$$U_x(\theta, \phi) = r^2 \cdot W_x(r, \theta, \phi) \quad [\mathrm{W}] \quad (2.20)$$

Where:

r	=	distance from the antenna	[m]
W_x	=	total or polarization dependent surface power density	$\left[\mathrm{W\,m^{-2}}\right]$

The total radiated power is therefore given as the total surface power density integrated over the whole sphere, Equation (2.21).

$$P_{\text{rad}} = \int_0^{2\pi} \int_0^{\pi} U_A(\theta, \phi) \sin\theta \, \mathrm{d}\theta \, \mathrm{d}\phi \quad [\mathrm{W}] \quad (2.21)$$

Where:

U_A	=	total radiation intensity	[W]

DIRECTIVITY

Directivity is a measure of how directional the radiation of antenna is, and is defined by Equation (2.22) [8].

$$D_x(\theta, \phi) = \frac{U_x(\theta, \phi)}{U_0} = \frac{4\pi U_x(\theta, \phi)}{P_{\text{rad}}} \quad [1] \quad (2.22)$$

Where:

D_x	=	total or polarization dependent directivity	[1]
U_0	=	total radiation intensity averaged over the sphere	[1]
P_{rad}	=	total radiated power	[W]

An isotropic antenna is an idealized antenna model with no loss and uniform radiation for all directions. As a result an isotropic antenna has directivity $D_{\text{isotropic}} = 1$. The directivity of an antenna is often expressed in logarithmic scale relative to the directivity of a isotropic antenna.

GAIN

The gain is a measure of the radiation intensity is in a given direction relative to either the accepted power (IEEE gain) or supplied power (realized gain). The gain can be viewed as the performance of an antenna compared to a lossless isotropic antenna.

The IEEE gain and Realized gain are given by Equations (2.23) and (2.24) respectively.

$$G_{\text{IE,x}}(\theta,\phi) = \frac{4\pi \cdot U_x(\theta,\phi)}{P_{\text{in}}} = e_{cd} \cdot \frac{4\pi \cdot U_x(\theta,\phi)}{P_{\text{rad}}} = e_{cd} \cdot D_x(\theta,\phi) \qquad [1] \tag{2.23}$$

$$G_{\text{Rl,x}}(\theta,\phi) = \frac{4\pi \cdot U_x(\theta,\phi)}{P_{\text{sup}}} = e_0 \cdot \frac{4\pi \cdot U_x(\theta,\phi)}{P_{\text{rad}}} = e_0 \cdot D_x(\theta,\phi) \qquad [1] \tag{2.24}$$

Where:

$G_{\text{IE,x}}$	=	total or polarization dependent IEEE antenna gain	[1]
$G_{\text{Rl,x}}$	=	total or polarization dependent realized antenna gain	[1]
P_{in}	=	power accepted by the antenna	[W]
P_{sup}	=	power supplied to the antenna	[W]
e_{cd}	=	antenna radiation efficiency	[1]
e_0	=	antenna total efficiency	[1]

GAIN BANDWIDTH

As mentioned in Section 2.5, the field strength at a given point is frequency dependent. As a result of this, the gain is also frequency dependent. The gain bandwidth is a performance metric detailing the width of the frequency band in which the gain in a certain direction is above a set threshold.

GAIN BEAMWIDTH

The beamwidth is a performance metric related to the antenna gain pattern. The gain beamwidth is the two-sided angular distance within which the gain is higher than a set threshold. The threshold can be defined relative to the direction of maximum gain or an arbitrary direction.

The Half Power Beam Width (HPBW) is a special case of the gain beamwidth metric. The HPBW is the continuous angular distance in which the antenna power gain is higher than half the maximum power gain of the antenna ($G_{\text{max,dB}} - 3\,\text{dB}$).

2.6 TRANSVERSE MODES

Transverse modes are usually used to describe the distribution of the H- and E-fields in objects such as waveguides and transmission lines. There are four different modes:

- **Transverse electric (TE) mode** - No electric field in the direction of propagation.
- **Transverse magnetic (TM) mode** - No magnetic field in the direction of propagation.
- **Transverse electromagnetic (TEM) mode** - No electric or magnetic field in the direction of propagation.
- **Hybrid mode** - Both electric and magnetic fields in the direction of propagation.

The modes are often denoted with a subscript to describe the order of the mode, e.g. TM_{nm}. For linear modes with propagation along the Z-axis, n denotes the number of half-wave patters across the X-axis and m denotes the number of half-waves across the Y-axis.

If the Mode is circular, n denotes the number of full-waves across the circumference and m denotes the half-waves across the diameter.

A third number is sometimes added to the subscript, e.g. TM_{knm}. At least one of the numbers should be zero the for transverse modes.

The remainder of this section describes relevant modes in the context that they are later used in.

2.6.1 TEM MODE – STRIPLINE

For TEM the E- and H -fields are perpendicular to the direction of propagation. Two examples of TEM mode are the coaxial transmission line and the embedded stripline. In both the two examples an inner conductor is embedded in a homogeneous dielectric region. In both examples, the E-fields lines lie between the inner conductor and the surrounding shield, while the H-field forms concentric circles around the inner conductor.

Figure 2.3 shows an example of how the E- and H-fields are arranged for a TEM stripline.

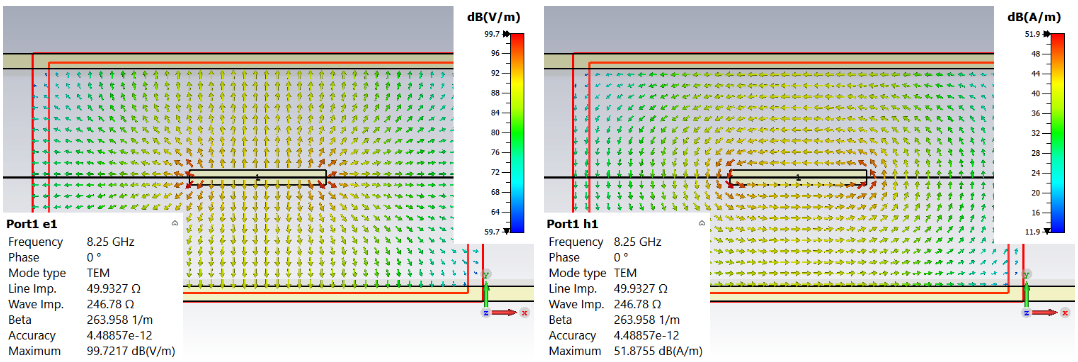

(a) The E-fields of a stripline carrying a TEM mode.

(b) The H-fields of a stripline carrying a TEM mode.

Figure 2.3: The E- and H-fields of a stripline carrying a TEM mode.

2.6.2 QUASI TEM MODE – MICROSTRIP

Quasi TEM is similar to TEM. A Quasi TEM wave propagates in two different media, as opposed to TEM that it travels in a homogeneous dielectric region.

A microstrip line supports the Quasi TEM mode. For a microstrip, the conductor is at the interface between two different media. On one side it has a substrate and on the other side it has air. The wave propagates with different speeds in the two media.

Figure 2.4 shows an example of how the E- and H-fields are arranged for a Quasi TEM microstrip.

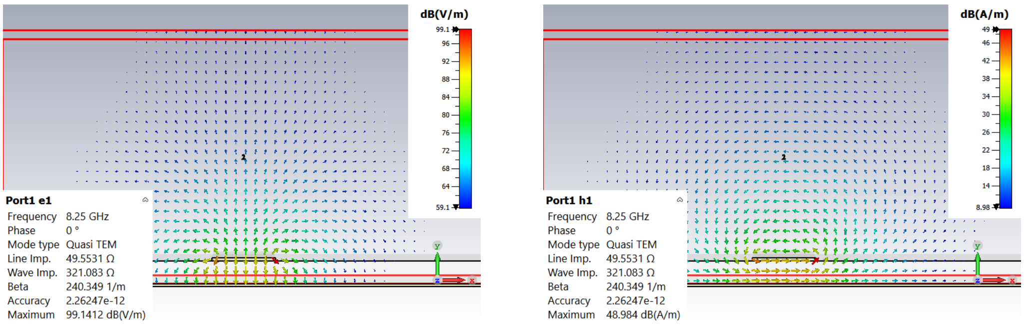

(a) The E-fields of a microstrip carrying a quasi TEM mode.

(b) The H-fields of a microstrip carrying a quasi TEM mode.

Figure 2.4: The E-and H-fields of a microstrip carrying a quasi TEM mode.

2.6.3 TM MODE – MICROSTRIP PATCH ANTENNA

Defining the propagation direction as the Y-axis, the fundamental mode of a rectangular patch antenna is TM_{100} or TM_{001} depending on the orientation. The first number in the subscript denotes the number of half-waves across the X-dimension of the patch and the third number denotes the number of half-waves across the Z-dimension of the patch.

Figure 2.5 shows two cross-sections of a patch antenna, with arrows showing the E-field strength and direction. Figure 2.5a shows that the E-field forms a half-wave.

Figure 2.5b shows that the E-field is constant across the width of the patch. The mode of the patch shown in Figure 2.5 is TM_{001}.

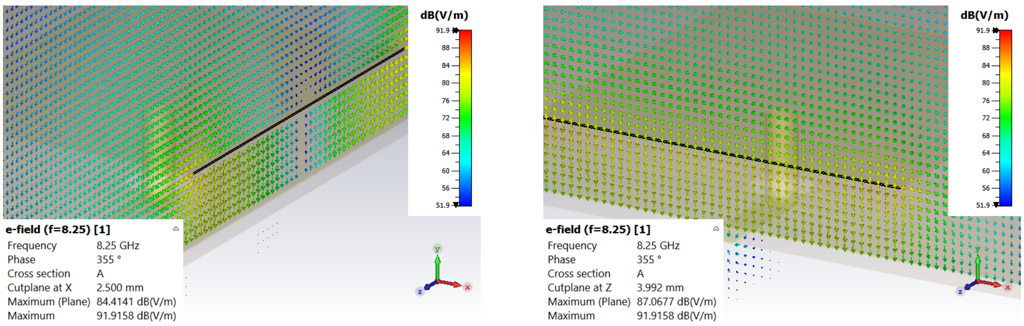

(a) Cross sections showing the E-field of a microstrip patch antenna in TM_{001} mode.

(b) Cross sections showing the E-field of a microstrip patch antenna in TM_{001} mode.

Figure 2.5: Illustration showing the E- and H-fields of a microstrip patch antenna in TM_{001} mode.

2.7 PATCH ANTENNA DESIGN

This section presents the relevant theory for designing linear polarized patch antenna elements. Section 2.8 presents the different methods of feeding patch antennas and Section 2.9 presents different methods of achieving circular polarization with a patch antennas.

Figure 2.6 shows a drawing of a rectangular patch antenna on a substrate.

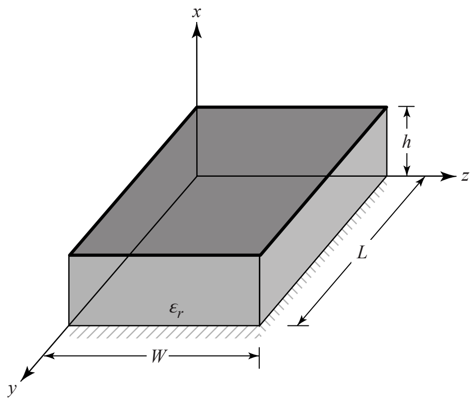

Figure 2.6: drawing of patch antenna [8, p. 801].

The width of the patch antenna can be calculated with Equation (2.25). Alternatively a different width can be chosen, however, this equation shows good results. [8, p. 791]

$$W = \frac{c}{2f_r}\sqrt{\frac{2}{\epsilon_r + 1}} \qquad [\mathrm{m}] \tag{2.25}$$

Where:

c	=	speed of light in vaccum	[m/s]
f_r	=	resonant frequency	[Hz]
ϵ_r	=	the relative permittivity of the substrate	[1]

The length of the patch L can be calculated using Equation (2.26) [8, p. 791].

$$L = \frac{1}{2f_r\sqrt{\epsilon_{\text{reff}}}\sqrt{\mu_0\epsilon_0}} - 2\Delta L \qquad [\mathrm{m}] \tag{2.26}$$

Where:

ΔL	=	length extension of patch due to fringing fields	[m]
ϵ_0	=	vacuum permittivity $\approx 8.854 \cdot 10^{-12}\,\mathrm{F\,m^{-1}}$	$\left[\mathrm{F\,m^{-1}}\right]$
μ_0	=	vacuum permeability $= 4\pi \cdot 10^{-7}\,\mathrm{H\,m^{-1}}$	$\left[\mathrm{H\,m^{-1}}\right]$

Where the patch length extension due to fringing fields ΔL is calculated using Equation (2.27) [8, p. 790].

$$\Delta L = h \cdot 0.412 \frac{(\epsilon_{\text{reff}} + 0.3)\left(\frac{W}{h} + 0.264\right)}{(\epsilon_{\text{reff}} - 0.258)\left(\frac{W}{h} + 0.8\right)} \quad [\text{m}] \quad (2.27)$$

$$\epsilon_{\text{reff}} = \frac{\epsilon_r + 1}{2} + \frac{\epsilon_r - 1}{2}\left[1 + 12\frac{h}{W}\right]^{-0.5} \quad [1] \quad (2.28)$$

Where:

ϵ_{reff}	=	effective relative permittivity	[1]
h	=	height of the substrate	[m]

Figure 2.7 shows the relationship between the patch width and patch length. A lower relative permittivity results in a larger patch antenna. Additionally, it is seen that as the width of the patch increases, the patch length decreases towards an asymptotic value dependent on the height h and the relative permittivity ϵ_r of the substrate.

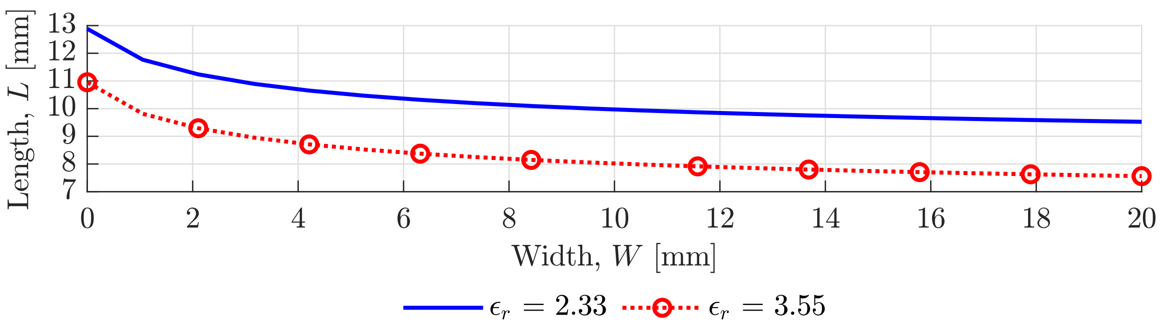

Figure 2.7: Relationship between Patch length and patch width for $h = 3.15$ mm and $f = 8.25$ GHz.

Figure 2.8 shows the patch length as a function of the frequency. The resonant frequency of the patch increases with a decreasing in patch length.

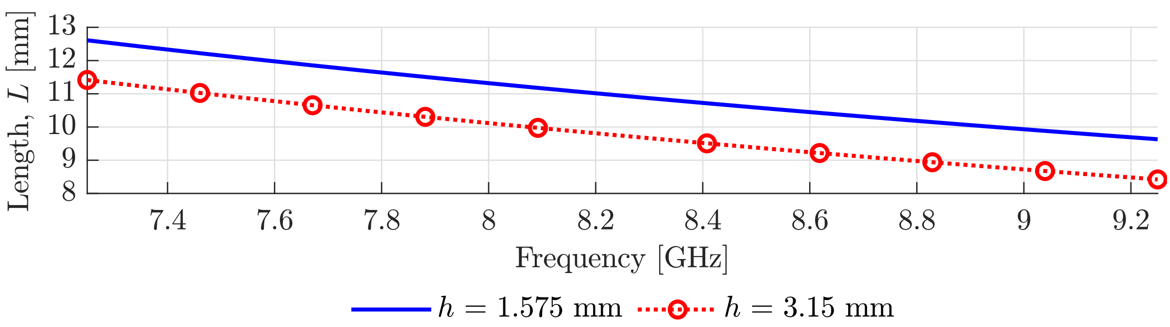

Figure 2.8: Relationship between patch length and frequency for $\epsilon_r = 2.33$ and W calculated with Equation (2.25).

2.7.1 PATCH ANTENNA DIRECTIVITY

The complex farfield E-field originating from a patch antenna in its first order resonant mode, ignoring the time-phase dependency, is approximately given by Equation (2.29) [8, eq. (14-43)].

$$\bar{\mathbf{E}}(r,\theta,\phi) \approx \begin{bmatrix} 0 \\ j\frac{k_0 W V_0 \mathrm{e}^{-jk_0 r}}{\pi r} \sin(\theta) \frac{\sin(X)}{X} \frac{\sin(Z)}{Z} \cos\left(\frac{k_0 L_e}{2} \sin(\theta) \sin(\phi)\right) \\ 0 \end{bmatrix} \quad [\mathrm{V\,m^{-1}}] \qquad (2.29)$$

Where:

X	=	$\frac{k_0 h}{2} \sin(\theta) \sin(\phi)$	[rad]
Z	=	$\frac{k_0 W}{2} \cos(\theta)$	[rad]
k_0	=	free space wave number $k_0 = \frac{2\pi}{\lambda}$	$\left[\mathrm{rad\,m^{-1}}\right]$
L_e	=	effective length $L_e = L + 2\Delta L$	[m]
V_0	=	the voltage from patch edge to ground	[V]

Figure 2.9 shows the directivity of a patch antenna tuned to frequency $f = 2\,\mathrm{GHz}$ with a substrate height $h = 3.15\,\mathrm{mm}$ and varying width W for four different relative permittivities ϵ_r. The directivity is calculated using the theory presented in this section, more specifically Equations (2.12), (2.20) to (2.22), (2.25), (2.26) and (2.29).

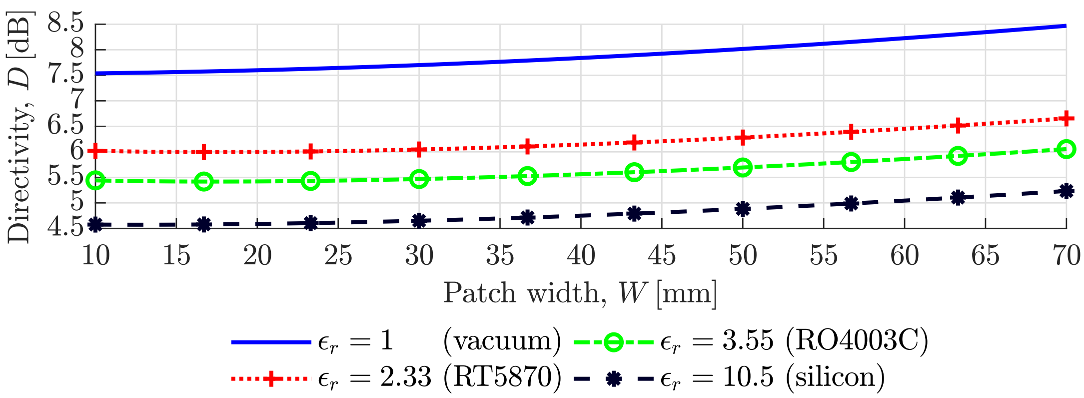

Figure 2.9: Theoretical directivity of a patch antenna tuned to a frequency $f = 2$ GHz with a substrate height $h = 3.15$ mm.

Figure 2.9 shows that the directivity can be improved by making the patch wider or decreasing the relative permittivity which in turn increases the resonant length of the patch antenna. To increase the directivity, the patch antenna must have a larger surface area.

2.7.2 PATCH CAVITY FIELD DISTRIBUTION

The field distribution for different TM_{0n0} modes is given by Equations (2.30) to (2.33) [8, p. 803].

$$E_x = -j\omega A_{0n0} \cos\left(\frac{n\pi y}{L}\right) \qquad [\mathrm{V\,m^{-1}}] \quad (2.30)$$

$$E_y = E_z = 0 \qquad [\mathrm{V\,m^{-1}}] \quad (2.31)$$

$$H_z = \frac{n\pi}{L\mu} A_{0n0} \sin\left(\frac{n\pi y}{L}\right) \qquad [\mathrm{A\,m^{-1}}] \quad (2.32)$$

$$H_x = H_y = 0 \qquad [\mathrm{A\,m^{-1}}] \quad (2.33)$$

Where:

E_i	=	i-component of the E-field	$\left[\mathrm{V\,m^{-1}}\right]$
H_i	=	i-component of the H-field	$\left[\mathrm{A\,m^{-1}}\right]$
A_{0n0}	=	amplitude coefficient of the TM_{0n0} mode	$\left[\mathrm{V\,m^{-1}}\right]$
n	=	TM mode order	[1]
y	=	y-coordinate and $y \in [0; L]$, see Figure 2.6	[1]

Since the absolute value of the field is not of importance for this section, normalized E- and H-fields are designed by Equations (2.34) and (2.35).

$$E_n = \frac{\|\bar{\mathbf{E}}\|_2}{\max_y \|\bar{\mathbf{E}}\|_2} = \left|\cos\left(\frac{n\pi y}{L}\right)\right| \qquad [1] \quad (2.34)$$

$$H_n = \frac{\|\bar{\mathbf{H}}\|_2}{\max_y \|\bar{\mathbf{H}}\|_2} = \left|\sin\left(\frac{n\pi y}{L}\right)\right| \qquad [1] \quad (2.35)$$

Where:

E_n	=	normalized E-field amplitude	[1]
H_n	=	normalized H-field amplitude	[1]

Figure 2.10 shows the field distributions for a patch antenna in the first and fourth order resonant mode (TM_{010} and TM_{040}). For the fundamental TM_{010} mode, the E-field is strongest on the radiating edge of the patch, while it is zero in the middle of the patch. The H-field is opposite the E-field, with a maximum in the middle of the patch and zero at the radiating edge.

The H-field coupling between the patch and a feed can be altered by moving the coupling point across the resonant length of the patch. This can be utilized in aperture feeding where a slot is cut in the ground plane below the middle of a patch to create a strong H-field coupling to a microstrip below the ground layer.

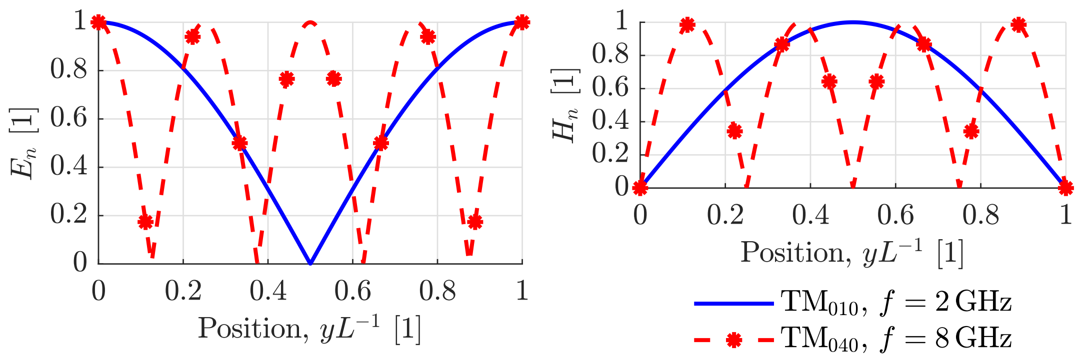

Figure 2.10: Analytical normalized E- and H-field magnitude between patch and ground plane for a 2 GHz patch antenna in its first and fourth order resonant mode.

The electrical potential between the middle of the patch and the ground plane is zero at the fundamental TM_{010} mode, meaning the patch can be grounded without altering the TM_{010} mode field distribution. In Chapters 5 and 6 this is exploited to ground the antenna elements without effecting the radiation of the antenna elements.

2.7.3 PATCH Q-FACTOR AND BANDWIDTH

The bandwidth of a patch antenna can be expressed based on allowed input Voltage Standing Wave Ratio (VSWR) and the quality factor Q_{tot}, as shown in Equation (2.36) [9, p. 294].

$$B = \frac{\mathrm{VSWR} - 1}{Q_{\mathrm{tot}}\sqrt{\mathrm{VSWR}}} \quad [1] \qquad (2.36)$$

Where:

B	=	fractional bandwidth	[1]
VSWR	=	allowable VSWR	[1]
Q_{tot}	=	total quality factor	[1]

The quality factor is the inverse sum of different contributions as shown in Equation (2.37).

$$\frac{1}{Q_{\mathrm{tot}}} = \frac{1}{Q_R} + \frac{1}{Q_{\mathrm{SW}}} + \frac{1}{Q_d} + \frac{1}{Q_c} \quad [1] \qquad (2.37)$$

Where:

Q_R	=	space-wave radiation Q-factor	[1]
Q_{SW}	=	surface-wave radiation Q-factor	[1]
Q_d	=	dielectric loss Q-factor	[1]
Q_c	=	conductive loss Q-factor	[1]

Approximate formulas for Q_R and Q_{SW} are given in the literature [8, 9, 10]. Both Q_R and Q_{SW} decreases with increasing substrate height and antenna width.

The dielectric and conductive loss Q-factors Q_d and Q_c are given by Equations (2.38) and (2.39) [9, p. 296].

$$Q_d = \frac{1}{\tan\delta} \quad [1] \qquad (2.38)$$

$$Q_c = h\sqrt{\pi f \mu_0 \sigma} \quad [1] \qquad (2.39)$$

Where:

h	=	substrate height	[m]
$\tan\delta$	=	substrate loss tangent	[1]
f	=	frequency	[Hz]
σ	=	patch conductivity	$\left[\mathrm{S\,m^{-1}}\right]$
μ_0	=	vacuum permeability	$\left[\mathrm{H\,m^{-1}}\right]$

From Equations (2.38) and (2.39) it can be seen that increasing the loss tangent (choosing a lossy substrate) and decreasing the conductivity (choosing a bad conductor) of the patch, increases the impedance bandwidth. Increasing thermal losses does however decrease antenna efficiency, so it should be considered a last resort for improving the impedance bandwidth.

Figure 2.11 shows VSWR = 2 patch antenna impedance bandwidths for different substrate heights and patch widths. The 2 GHz patch length is adjusted to its resonant length using Equation (2.26) for every substrate height and patch width combination.

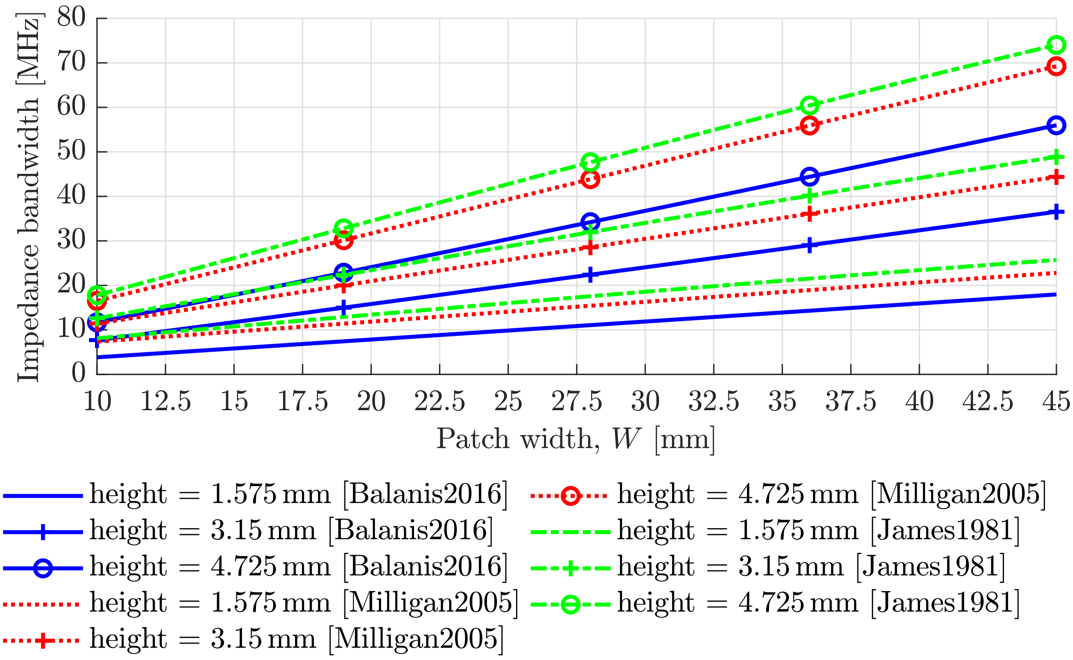

Figure 2.11: Approximate impedance bandwidth of a 2 GHz patch antenna of length given by Equation (2.26). Equations from [8, 9, 10].

As shown in Figure 2.11, to obtain a bandwidth of at least 60 MHz, as required in Chapter 4, the substrate height has to be $h \geq 4.752$ mm and the patch width has to be $W \geq 35$ mm. These equations are however only approximations and will not be precise in practice.

Appendices B and C confirms the bandwidth dependency on substrate height and patch width through simulations.

2.7.4 INPUT IMPEDANCE

To approximate the input impedance at a point along the resonant length, the patch is commonly modelled as a low-impedance transmission line. The transmission line has an admittance Y_m of length L separating two radiating slots of width W (or W_e denoting the effective width due to fringing fields) [8, 10]. The radiating slots are represented as equivalent parallel admittances $Y_s = G_s \pm G_m + jB$, where G_s is the slot self conductance and G_m is the mutual conductance between the two slots. The contribution from the susceptance B is usually assumed negligible and the conductances G_s and G_m are approximated by different means.

The input impedance at the n'th order resonance at a point y along the resonant length of the patch is then given as Equation (2.40) assuming $Y_m \gg (G_r \pm G_m)$ and B. [8, 10]

$$Z_{\text{in}} = \frac{1}{2\left(G_s - G_m \cos\left(n\pi\right)\right)} \cos^2\left(n\pi y L^{-1}\right) \qquad [1] \quad (2.40)$$

Where:

Z_{in}	=	input impedance	[Ω]
G_s	=	slot self conductance	[S]
G_m	=	slot mutual conductance	[S]
y	=	feed position	[m]
n	=	order of resonance	[1]

The self conductances and mutual conductances can be approximated as Equations (2.41) and (2.42) [10, p. 87-88].

$$G_s = \frac{1}{120\pi^2} F_2\left(\frac{2\pi}{\lambda_0} \cdot W_e\right) \qquad [\text{S}] \quad (2.41)$$

$$F_2(x) = x \cdot \int_0^x \frac{\sin\left(t\right)}{t}\,\mathrm{d}t - 2\sin^2\left(\frac{x}{2}\right) - 1 + \frac{\sin\left(x\right)}{x}$$

$$G_m = \frac{1}{120\pi^2} \int_0^\pi \frac{\sin^2\left(\frac{\pi W_e}{\lambda_0}\cos\left(\theta\right)\right)}{\cos^2\left(\theta\right)} \sin^3\left(\theta\right) J_0\left(\frac{2\pi\sin\left(\theta\right)}{\lambda_0}\right) \mathrm{d}\theta \qquad [\text{S}] \quad (2.42)$$

Where:

λ_0	=	free space wavelength	[m]
W_e	=	$\frac{120\pi \cdot h}{Z_m \cdot \sqrt{\epsilon_{\text{reff}}}}$, effective patch width	[m]
$J_0(x)$	=	zero'th order bessel function of the first kind	[1]

For thin substrates $\left(\frac{W}{h} > 1\right)$, the characteristic impedance of the microstrip Z_m making up the patch antenna, which is used to approximate W_e, is estimated as Equation (2.43) [8, eq. (14-19b)].

$$Z_m = \frac{120\pi}{\sqrt{\epsilon_{\text{reff}}}\left(\frac{W}{h} + 1.393 + 0.667\ln\left(\frac{W}{h} + 1.444\right)\right)} \qquad [\Omega] \quad (2.43)$$

Where:

h	=	substrate height	[m]
W	=	patch width	[m]

An alternative expression for the slot self conductance is given by Equation (2.44) [8, eq. (14-8a)].

$$G_s = \frac{W}{120\lambda_0}\left(1 - \frac{1}{24}\left(\frac{2\pi}{\lambda_0}h\right)^2\right) \quad [\mathrm{S}] \qquad (2.44)$$

Figure 2.12 shows the input impedance of a 2 GHz patch antenna with $W = 35\,\mathrm{mm}$ and $h = 4.752\,\mathrm{mm}$ for the first order resonance at 2 GHz and forth order resonance at 8 GHz.

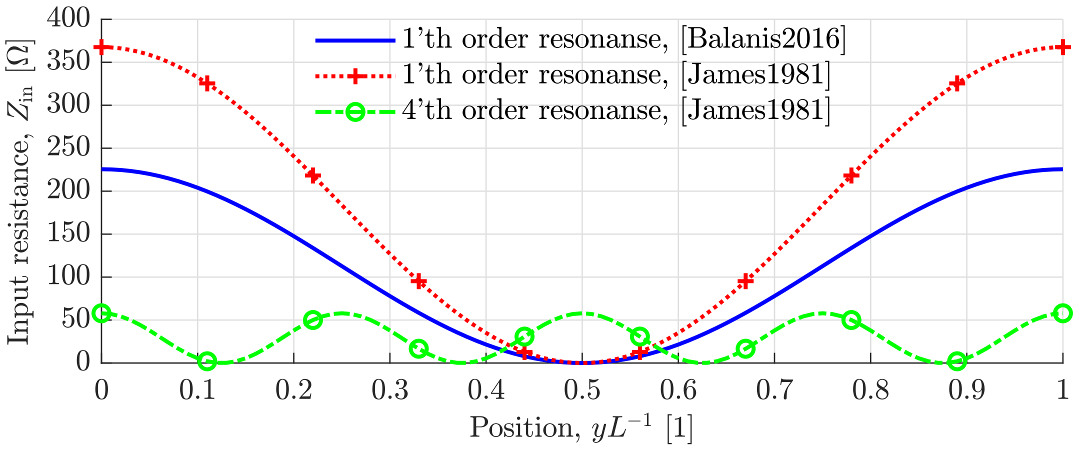

Figure 2.12: Analytically estimated input impedance along the resonant length of the 2 GHz tuned patch at frequencies 2 GHz and 8 GHz. Formulas from [8, 10].

Figure 2.12 shows that choosing a specific impedance for the feed, the fourth order mode can be suppressed while having a good match for the first order mode.

If a feed impedance of $Z_0 = 50\,\Omega$ and a feed point at $y \approx 0.38L$ is chosen in the example shown in Figure 2.12, the reflection coefficient between the patch and the feed can be calculated as shown by Equations (2.45) and (2.46).

$$\Gamma_{2\,\mathrm{GHz}} = \frac{Z_{\mathrm{in},2\,\mathrm{GHz}} - Z_0}{Z_{\mathrm{in},2\,\mathrm{GHz}} + Z_0} \approx \frac{50-50}{50+50} = 0 \quad [1] \qquad (2.45)$$

$$\Gamma_{8\,\mathrm{GHz}} = \frac{Z_{\mathrm{in},8\,\mathrm{GHz}} - Z_0}{Z_{\mathrm{in},8\,\mathrm{GHz}} + Z_0} \approx \frac{0.21-50}{0.21+50} = -0.9916 \quad [1] \qquad (2.46)$$

Where:

Z_0 = impedance of feed [Ω]

2.8 ANTENNA FEEDING

With the dimensions of the patch antenna determined, the next step is excite the desired mode. Some commonly used patch antenna excitation methods are:

- Edge feed: A microstrip feeding line directly connected to the edge of the patch element.
- Probe feed: A feed line with a probe connecting the feeding line and the patch element.
- Aperture feed: A feed line which couples to the patch element through a slot in the ground plane.
- Proximity coupled: A feed line is placed in proximity of the patch and thereby couples to the patch element.

Common for all these four methods is, that they can be realized using either microstrip or stripline.

Equations (2.47) and (2.48) can be used to calculate the width of a microstrip to realize a desired characteristic impedance [8, p. 789, 797].

$$Z_0 = \frac{\frac{\eta}{\sqrt{\epsilon_{\mathrm{reff}}}}}{\frac{W_{\mathrm{ms}}}{h} + 1.393 + 0.667 \cdot \ln\left(\frac{W_{\mathrm{ms}}}{h} + 1.444\right)}, \text{for } \frac{W_{\mathrm{ms}}}{h} \geq 1 \qquad [\Omega] \quad (2.47)$$

$$\epsilon_{\mathrm{reff}} = \frac{\epsilon_r + 1}{2} + \frac{\epsilon_r - 1}{2}\left(1 + 12 \cdot \frac{W_{\mathrm{ms}}}{h}\right)^{-\frac{1}{2}} \qquad [1] \quad (2.48)$$

Where:

W_{ms}	=	width of the microstrip	[m]
η	=	impedance of free space, $\eta = 120\pi\,\Omega$	[Ω]
h	=	height of the substrate	[m]
ϵ_r	=	the relative permittivity of the substrate	[1]
ϵ_{reff}	=	effective relative permittivity	[1]

Equation (2.49) can be used to calculate the width of a stripline to realize a desired characteristic impedance. The equation is only for striplines with equal substrate thickness above and below the line [7].

$$W_{\mathrm{sl}}(Z_0) = h \cdot \begin{cases} x(Z) & \text{if } Z_0 \cdot \sqrt{\epsilon_r} < 120 \\ 0.85 - \sqrt{0.6 - x(Z_0)} & \text{if } Z_0 \cdot \sqrt{\epsilon_r} > 120 \end{cases} \qquad [\mathrm{m}] \quad (2.49)$$

$$x(Z_=) = \frac{30\pi}{\sqrt{\epsilon_r} Z_0} - 0.441$$

Where:

W_{sl}	=	width of the stripline	[m]
Z_0	=	intrinsic impedance of the stripline	[Ω]
h	=	sum of substrate thicknesses	[m]

2.9 ACHIEVING CIRCULAR POLARIZATION WITH PATCH ANTENNAS

A multi-antenna topology can also be used to achieve circular polarization. If two patch antennas are arranged such that the linear polarized mode of the patches are orthogonal to each other, the patches can be combined with a $\pm 90°$ phase shift to produce circular polarization. Section 2.10 discusses how multi element antenna arrays can be arranged and how they can achieve circular polarization.

This remainder of this section is dedicated to different methods of achieving circular polarization with a single patch antenna element.

Circular polarisation is achieved with a single patch antenna by exiting two orthogonal modes with a $90°$ phase difference. This section investigates the following methods of achieving circular polarization [8]:

- Using two feeding points
- Feeding the corner of a nearly square patch
- Trimming two opposite corners of a square patch
- Cutting a rotated rectangular slot in a square patch

Appendix A simulates the four mentioned methods of achieving circular polarization. The appendix utilizes time domain simulations to evaluate the four methods. All four methods result in similarly sized patch antennas with comparable radiation performance.

2.9.1 DUAL FED SQUARE PATCH

Excitation the two orthogonal modes of a patch can be done using two feeds, one for each mode. One feed is placed along the length L of the patch, centred on the width W. The other feed is placed along the width W, centred on the length L. The two feeds carries waves with a $90°$ phase delay between them.

Figure 2.13 shows how two microstrip lines and two feeding probes can be used to feed the two orthogonal resonant modes of a patch antenna. The antenna achieves RHCP if the rightmost microstrip carries a relative phase of $-90°$ compared to the leftmost microstrip, and LHCP if it carries a relative phase of $+90°$.

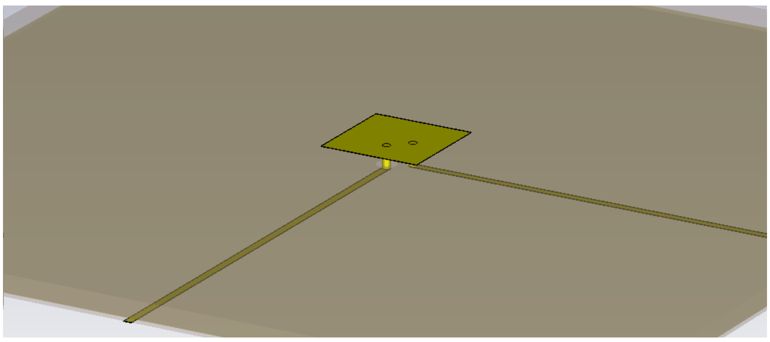

Figure 2.13: Dual fed patch antenna.

If the patch is square, both modes has the same resonance frequency. This results in both modes being of equal strength and results in a good axial ratio if the feeds carries the correct phase difference.

2.9.2 CORNER FED NEARLY SQUARE PATCH

The two orthogonal modes of a patch antenna can be excited with a single feeding line and a single feeding probe. This is done by having the feeding point along the patch diagonal and by having a difference between the antenna length and the antenna width. The length and width are adjusted to support two modes at two different frequencies.

To find the supported modes, a CST multilayer Characteristic Mode Analysis (CMA) simulation is used. The CMA provides characteristic angles ϕ_n and modal significances A_n for N requested modes. The modular significance is a metric for the relative strength of a resonance, while the characteristic angle is its phase.

To achieve circular polarization, the phase difference between the two orthogonal modes must be $\Delta\phi = \phi_1 \pm \phi_2 = \pm\ 90°$. Where ϕ_n is the characteristic angle of the n'th mode. Since the two resonances are not necessarily the same strength at the frequencies where the phase criterion is fulfilled, excitation should be adjusted to compensate.

Figure 2.14 shows a 3D model of the nearly square patch and the two supported orthogonal modes. The proportional excitation of the two modes can be adjusted by changing the angle v, while the radius r determines the input impedance and coupling between the feed and the patch.

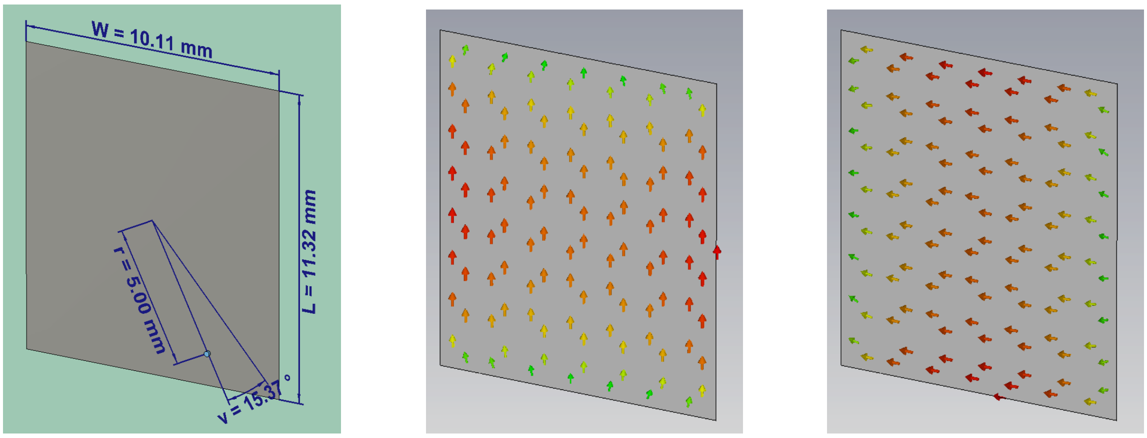

(a) 3D model of a nearly square corner fed patch antenna. The small blue cylinder marks the feeding position.

(b) Simulated current distribution for resonant mode 1 (lower frequency).

(c) Simulated current distribution for resonant mode 2 (higher frequency).

Figure 2.14: 3D model and simulated current distribution of nearly square patch antenna from CST multilayer CMA simulation.

This thesis has empirically found that rotating the feed point an angle v relative to the patch center, where v is given by Equation (2.50), achieves circular polarization.

$$v = 45° - \arctan\left(\frac{A_1}{A_2}\right) \qquad [°] \qquad (2.50)$$

Where:

A_n = the modal significance of the n'th mode [1]

Figure 2.15 shows the simulated characteristic angles, modal significances, and broadside axial ratio. At $f = 8.502\,\text{GHz}$ the phase difference is $\Delta\phi = 90°$ and the angle is $v \approx$

$45° - \arctan\left(\frac{0.49}{0.87}\right) \approx 15.37°$. These values are used in a time domain simulation to extract the axial ratio. There is a low axial ratio at $f = 8.15\,\text{GHz}$, showing a frequency offset between the CMA and time domain simulations.

Figure 2.15 also shows that circular polarization can be achieved at two different frequencies, implying that the axial ratio should have two minima at different frequencies as the angle v is swept in the range -45 to $45°$.

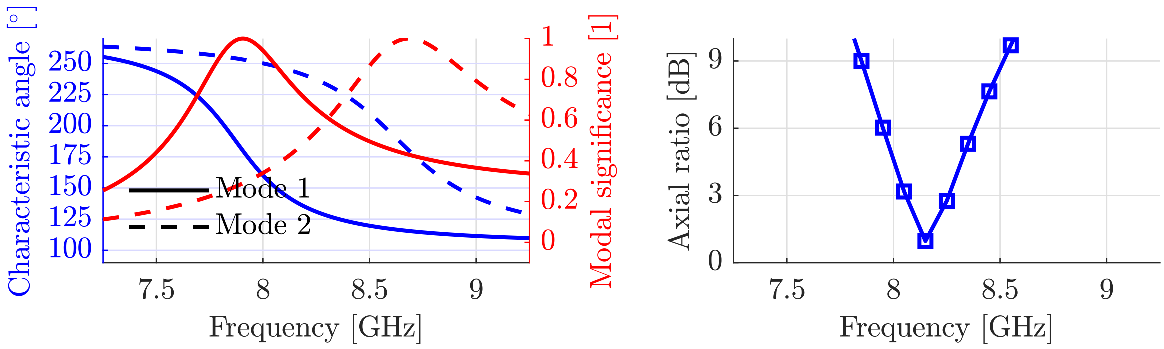

Figure 2.15: Simulated characteristic angle and modal significance of the two resonant modes from CST multilayer CMA simulation and axial ratio from CST time domain simulation of the nearly square patch in Figure 2.14a.

2.9.3 CORNER TRIMMED SQUARE PATCH

Circular polarization can be achieved by trimming two opposite corners of a square patch. The diagonal with cut corners supports a higher frequency mode and the orthogonal diagonal supports a lower frequency mode. If the lower left and upper right corners are trimmed, the patch is RHCP.

Following the same procedure as with the corner feed nearly square patch, Figure 2.16 shows a 3D model and the two orthogonal modes.

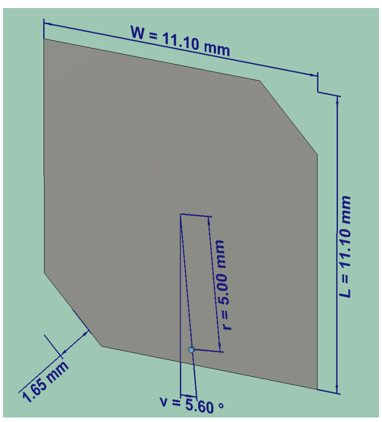

(a) 3D model of a corner trimmed square patch antenna. The small blue cylinder marks the feeding position.

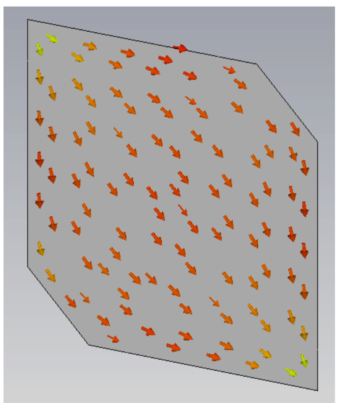

(b) Simulated current distribution for resonant mode 1 (lower frequency).

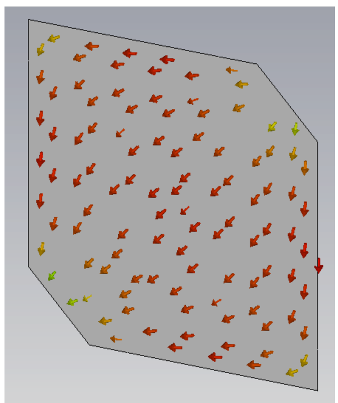

(c) Simulated current distribution for resonant mode 2 (higher frequency).

Figure 2.16: 3D model and simulated current distribution of corner trimmed square patch antenna from CST multilayer CMA simulation.

Figure 2.17 shows the simulated characteristic angle, modular significance, and broadside axial ratio. At $f = 8.378\,\text{GHz}$ the phase difference is $\Delta\phi = 90°$ and the angle is $\upsilon \approx 45° - \arctan\left(\frac{0.64}{0.77}\right) \approx 5.6°$. These values are used in a time domain simulation to extract the axial ratio. There is a low axial ratio at $f = 8.05\,\text{GHz}$, showing a frequency offset between the CMA and time domain simulations as was also the case with the nearly square design.

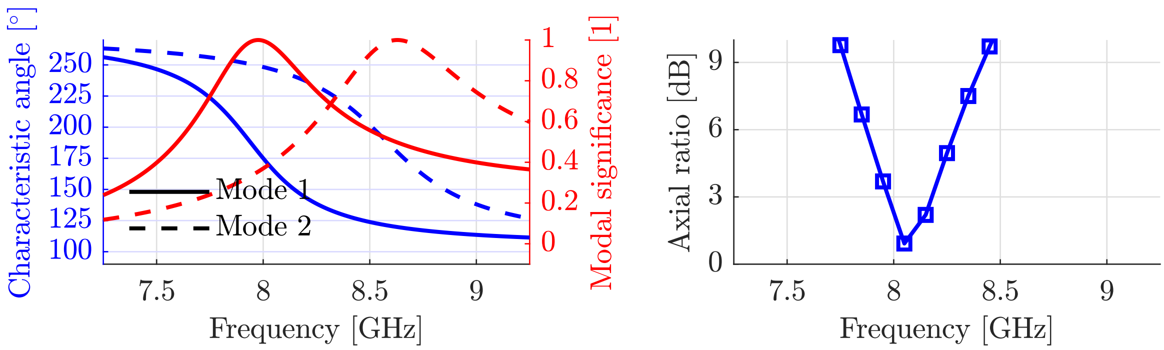

Figure 2.17: Simulated characteristic angle and modular significance of the two resonant modes from CST multilayer CMA simulation and axial ratio from CST time domain simulation of the corner trimmed square patch in Figure 2.16a.

2.9.4 ROTATED RECTANGULAR CUT-OUT IN THE PATCH

Circular polarisation can also be achieved by cutting a rotated rectangular slot on a square patch as seen in Figure 2.18a. This way the patch support two orthogonal modes along the diagonals at two different frequencies.

The literature provides a rough estimate of the slot dimensions for a square patch by Equations (2.51) and (2.52) [8, p. 831].

$$\text{slotL} = \frac{W}{2.72} \qquad [\text{m}] \qquad (2.51)$$

$$\text{slotW} = \frac{\text{slotL}}{10} \qquad [\text{m}] \qquad (2.52)$$

Where:

slotL	=	length of the slot	[m]
slotW	=	width of the slot	[m]
W	=	patch width	[m]

The slot seen in Figure 2.18a makes the patch RHCP given proper excitation. Figure 2.18 shows the 3D model and current distributions for the two orthogonal modes.

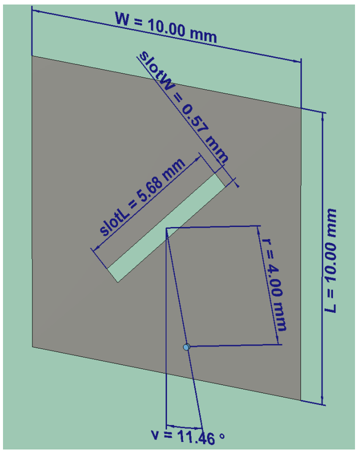

(a) 3D model of a slotted patch antenna. The small blue cylinder marks the feeding position.

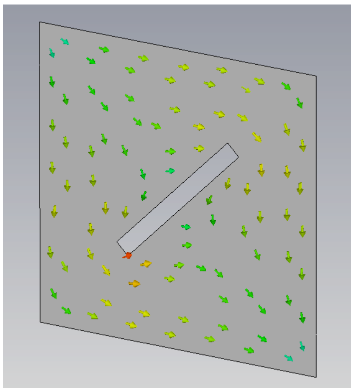

(b) Simulated current distribution for resonant mode 1 (lower frequency).

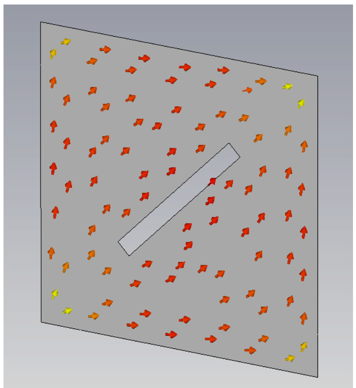

(c) Simulated current distribution for resonant mode 2 (higher frequency).

Figure 2.18: 3D model and simulated current distribution of slotted patch antenna from CST multilayer CMA simulation.

The dimensions of the patch has been fitted through simulations to provide phase the desired phase difference. The dimensions are shown in Figure 2.18a and the simulated characteristic angle, modal significance, and broadside axial ratio are shown in Figure 2.19. At $f = 8.464\,\text{GHz}$ the phase difference is $\Delta\phi = 90°$ and the angle is $v \approx 45° - \arctan\left(\frac{0.55}{0.83}\right) \approx 11.46°$. These values are used in a time domain simulation to extract the axial ratio.

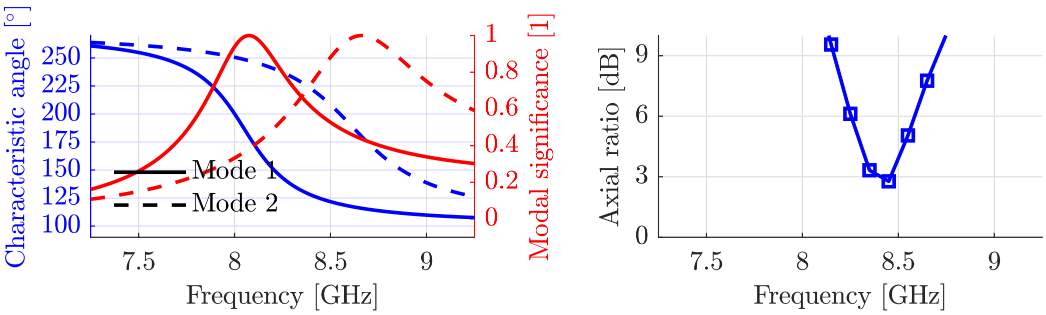

Figure 2.19: Simulated characteristic angle and modular significance of the two resonant modes from CST multilayer CMA simulation and axial ratio from CST time domain simulation of the slotted square patch in Figure 2.18a.

Figure 2.19 shows a minimum axial ratio at $f = 8.45\,\text{GHz}$ which fits well with the CMA simulation. The axial ratio is however higher for this simulation indicating that the two modes are either not excited properly, or the phase difference is not as expected. Equation (2.50) however still provides an initial estimate for further optimization.

2.10 ANTENNA ARRAY

This section introduces the term array factor (array gain when measured in dB), shows how circular polarization can be achieved by using two linearly polarized antennas, and considers different antenna array arrangements.

Antenna arrays can be construed in different shapes and sizes. Figure 2.20 shows three simple examples of how microstrip patch antennas can be arranged in an antenna array.

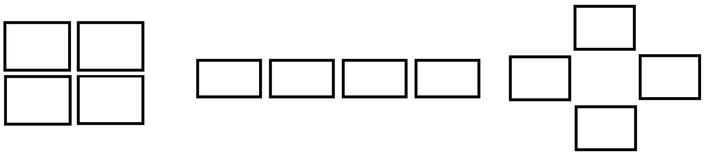

Figure 2.20: Examples of antenna array structures.

Given an array of N antennas each transmitting a weighted version $\bar{\mathbf{E}}_n$ of the same continuous wave $\bar{\mathbf{E}}$, the total E-field $\bar{\mathbf{E}}_T$ at a point in space is the sum of the contributions from all N antennas in the array. Given that the point is sufficiently far away from the antenna array, the spherically radiated wave can be approximated as a plane wave with a unit normal vector given by Equation (2.53).

$$\bar{\mathbf{N}} = \begin{bmatrix} \cos(\phi)\sin(\theta) \\ \sin(\phi)\sin(\theta) \\ \cos(\theta) \end{bmatrix} \qquad [1] \quad (2.53)$$

The distance from each antenna to the plane wave is given by Equation (2.54) [11].

$$r_n = r + \Delta r_n = r + \bar{\mathbf{P}}_n \bullet \bar{\mathbf{N}} \qquad [\mathrm{m}] \quad (2.54)$$

Where:

$\bar{\mathbf{P}}_n$	=	position vector of n'th antenna	[m]
Δr_n	=	$\bar{\mathbf{P}}_n \bullet \bar{\mathbf{N}}$ = relative distance to plane-wave from n'th antenna	[m]
$\bullet$	=	dot-product operator	[1]

The different distances to the plane wave constitute a relative phase shift as given by Equation (2.55).

$$v_n = \frac{2\pi}{\lambda}\Delta r_n \qquad [\mathrm{rad}] \quad (2.55)$$

The amplitude of the field contribution from antenna n to the total E-field is proportional to the distance r_n. A common assumption is that $r \gg \Delta r_n$ for all N antennas, so the field amplitude becomes independent of Δr_n. The total E-field and array factor (AF) is then given by Equation (2.56), which is a simplification under the assuming that all antennas radiate identically.

$$\bar{\mathbf{E}}_T = \sum_{n=1}^{N} \bar{\mathbf{E}}_n \mathrm{e}^{jv_n} = \bar{\mathbf{E}} \sum_{n=1}^{N} w_n \mathrm{e}^{jv_n} = \bar{\mathbf{E}} \cdot \mathrm{AF} \qquad [\mathrm{V\,m^{-1}}] \quad (2.56)$$

Where:

w_n	=	weight of n'th antenna	[1]
AF	=	$\sum_{n=1}^{N} w_n e^{jv_n}$	[1]

Assuming power is split equally among all N antenna elements, the array factor is given by Equation (2.57).

$$\mathrm{AF} = \frac{1}{\sqrt{N}} \sum_{n=1}^{N} e^{j(v_n + u_n)} \qquad [1] \quad (2.57)$$

Where:

u_n	=	$\angle w_n$ = phase of weight assigned to antenna n	[rad]

As an example, take a linear array of N antennas placed on the X-axis, pointing in the Z-axis direction, and spaced by distance d. The array factor for equally split power is given by Equation (2.58). For $\phi = u_n = 0$, the array factor is given by Equation (2.59)

$$\mathrm{AF} = \frac{1}{\sqrt{N}} \sum_{n=1}^{N} \exp\left(j\left(\frac{2\pi}{\lambda}(n-1)\, d\cos(\phi)\sin(\theta) + u_n\right)\right) \qquad [1] \quad (2.58)$$

$$\mathrm{AF} = \frac{1}{\sqrt{N}} \sum_{n=1}^{N} \exp\left(j\frac{2\pi}{\lambda}(n-1)\, d\sin(\theta)\right) \qquad [1] \quad (2.59)$$

Where:

d	=	distance between each antenna	[m]

Figure 2.21 shows the array gain ($\mathrm{AG} = 20\log_{10}|\mathrm{AF}|$) dependent on the number of antennas N, separation d, and θ. The main beam width and side lobe level are dependent on the distance d. The broadside array factor ($\theta = 0$) is independent of the separation d and equal $\mathrm{AF_{bs}} = \frac{N}{\sqrt{N}}$, which means that each time the number of antennas is doubled, the broadside gain increases by approximately 3 dB. The 3 dB rule is true for all planar arrays.

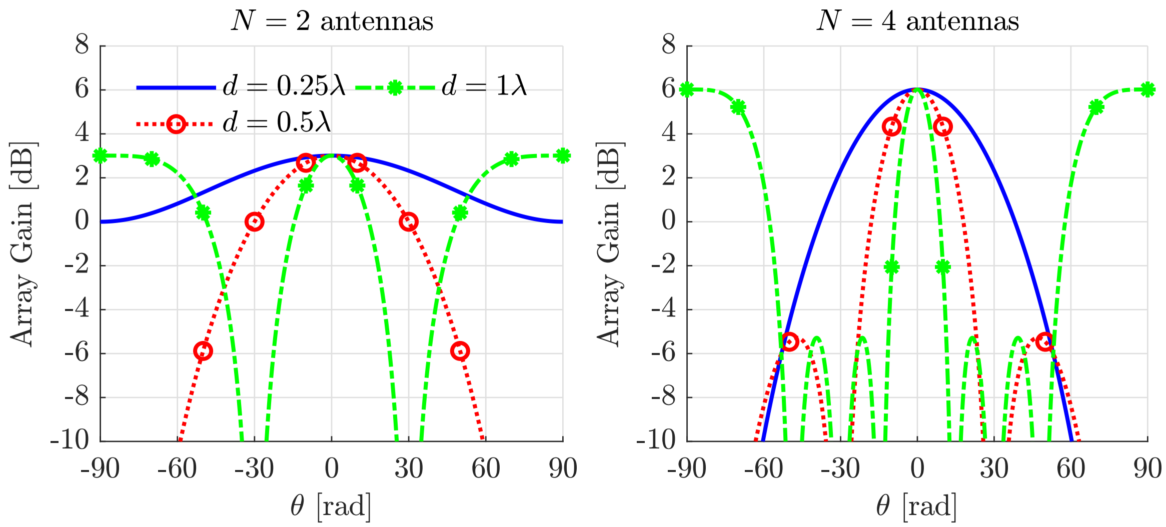

Figure 2.21: Array gain for different numbers of antennas N, antenna separation d, and angle θ. The broadside gain is visibly independent of the separation d and equal $\mathrm{AG_{bs}} = 20\log_{10}\left|\frac{N}{\sqrt{N}}\right|$.

Antenna arrays can also be used to alter the polarization of the radiated field. Circular polarization can for example be realized using two linearly polarized antennas, if one antenna is rotated $\phi = \frac{\pi}{2}$ rad and weighted with phase $u_2 = -\frac{\pi}{2}$ rad. The total broadside direction E-field is then given by Equation (2.60), assuming antennas are fully "θ-polarized" ($\bar{\mathbf{E}} = \begin{bmatrix}0 & E_\theta & 0\end{bmatrix}^T$).

$$\bar{\mathbf{E}}_T = \frac{1}{\sqrt{2}} \cdot \left(\begin{bmatrix}1 & 0 & 0\\0 & 1 & 0\\0 & 0 & 1\end{bmatrix} \bar{\mathbf{E}} + \begin{bmatrix}1 & 0 & 0\\0 & 0 & 1\\0 & -1 & 0\end{bmatrix} \mathrm{e}^{-j\frac{\pi}{2}} \bar{\mathbf{E}} \right) = \frac{1}{\sqrt{2}} \begin{bmatrix}0\\E_\theta\\-jE_\theta\end{bmatrix} \tag{2.60}$$

Using Equation (2.12), the relative change in absolute gain, by introducing the rotated antenna, is calculated as:
$\Delta G_A = 10\log_{10}\left(\frac{1}{2} + \frac{1}{2}\right) = 0\,\text{dB}$.

Using Equations (2.18) and (2.19), the axial ratio is $\text{AR} = 1$ and the relative change in RHCP gain is calculated as:
$\Delta G_{\text{RC}} = 10\log_{10}\left(|\frac{1}{\sqrt{2}} + \frac{1}{\sqrt{2}}|^2\right) \approx 3\,\text{dB}$.

In practice the radiation pattern of the individual antenna is altered by inserting adjacent antennas to form an array. There is cross-coupling between antenna elements causing energy to be absorbed by adjacent antennas instead of radiated. Due to these effects, the broadside gain will be dependent on the arrangement and separation in the antenna array. Appendix E investigates the broadside gain for different array arrangements and separations.

Appendix E shows that for a two-by-two planar antenna array the distance between the antenna elements is an important design parameter. The broadside gain is found to vary with up to 3 dB with antenna separation with a maximum gain at $d = 0.7\lambda$, illustrating the importance of the spacing within the array.

Appendix E also shows circular polarization being realized utilizing four sequentially rotated linearly polarized antennas.

2.11 POWER DIVISION

In an antenna array, the antenna elements have to be excited. A common way of doing this is to excite them individually by a stripline or waveguide network incorporating power dividers to split the power between the antenna elements. Alternatively, one could excite a single element which in turn excites adjacent elements through electromagnetic coupling. A feeding network from stripline with power dividers provides a simple and well-performing solution for the frequency range of interest and is, therefore, the focus of this section.

Ideally, a power divider should be lossless, matched on all ports, and have complete isolation between the two power divided ports (ports two and three). The S-parameters for a passive ideal equal 2-way power divider should be as shown in Equation (2.61).

$$S = \begin{bmatrix}0 & S_{12} & S_{13}\\S_{12} & 0 & 0\\S_{13} & 0 & 0\end{bmatrix} \tag{2.61}$$

Power conservation states among others Equations (2.62) and (2.63) [7, eq. (4.53)].

$$|S_{12}|^2 + |S_{13}|^2 = 1 \implies |S_{12}| = |S_{13}| = \frac{1}{\sqrt{2}} \qquad [1] \quad (2.62)$$

$$|S_{12}|^2 = 1 \quad , \quad |S_{13}|^2 = 1 \qquad [1] \quad (2.63)$$

Which shows that the ideal, passive, lossless, and matched power divider with complete isolation is not possible. Depending on the objective, different designs incorporate resistors, impedance mismatching, or low isolation to make the power divider realizable.

The T-junction power divider is a design with imperfect isolation and impedance matching on the two power divided ports (ports two and three). The T-junction power divider is made from striplines arranged to form a "T" shape. A model of the T-junction power divider is seen in Figure 2.22a.

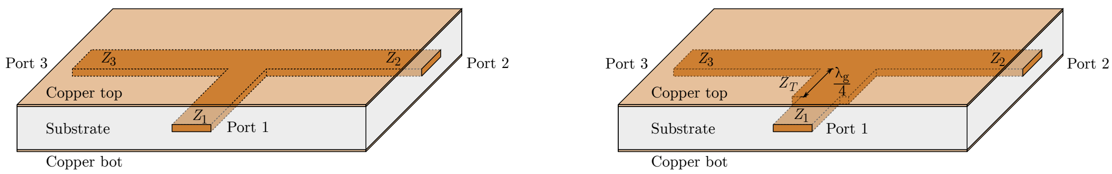

(a) Drawing of a T-junction power divider made in stripline.

(b) Drawing of a T-junction power divider with a quarter-wave impedance transformer made in stripline.

Figure 2.22: Drawings of two power divider models.

The input impedance seen from the three ports is given by Equation (2.64).

$$Z_{\text{in},1} = Z_2 \parallel Z_3 \quad , \quad Z_{\text{in},2} = Z_1 \parallel Z_3 \quad , \quad Z_{\text{in},3} = Z_1 \parallel Z_2 \qquad [\Omega] \quad (2.64)$$

Where:

$Z_{\text{in,X}}$	=	input impedance of port X	[Ω]
Z_X	=	characteristic impedance of stripline X	[Ω]

To have impedance matching at port 1, $Z_{\text{in},1} = Z_1$ has to be satisfied. For equal power division $Z_2 = Z_3 = 2Z_1$ should be satisfied. By this follows Equations (2.65) to (2.67) assuming all ports are perfectly terminated.

$$\Gamma_1 = \frac{(Z_2 \parallel Z_3) - Z_1}{(Z_2 \parallel Z_3) + Z_1} = 0 \qquad [1] \quad (2.65)$$

$$\Gamma_2 = \frac{(Z_1 \parallel Z_3) - Z_2}{(Z_1 \parallel Z_3) + Z_2} = -\frac{1}{2} \qquad [1] \quad (2.66)$$

$$\Gamma_3 = \frac{(Z_1 \parallel Z_2) - Z_3}{(Z_1 \parallel Z_2) + Z_3} = -\frac{1}{2} \qquad [1] \quad (2.67)$$

Where:

Γ_x	=	reflection coefficient into port x	[1]

The S-parameters are given by Equation (2.68).

$$S_{\mathrm{T-junction}} = \begin{bmatrix} 0 & \frac{1}{\sqrt{2}} & \frac{1}{\sqrt{2}} \\ \frac{1}{\sqrt{2}} & -\frac{1}{2} & \frac{1}{2} \\ \frac{1}{\sqrt{2}} & \frac{1}{2} & -\frac{1}{2} \end{bmatrix} \qquad [1] \quad (2.68)$$

In cases where specific input and output impedances are desired a quarter-wave impedance transformer can be used to match the impedances. Figure 2.22b shows how a quarter-wave impedance transformer can be added to the T-junction power divider, such that the port 1 reflection coefficient $\Gamma_1 = 0$ even though $Z_1 = Z_2 = Z_3$.

The impedance into the power divider at the end of the quarter-wave impedance transformer is given by Equation (2.69).

$$Z_{\mathrm{in,pd}} = Z_2 \parallel Z_3 \qquad [\Omega] \quad (2.69)$$

And the reflection coefficient is given by Equation (2.70).

$$\Gamma_{\mathrm{pd}} = \frac{Z_{\mathrm{in,pd}} - Z_T}{Z_{\mathrm{in,pd}} + Z_T} \qquad [\Omega] \quad (2.70)$$

For a terminated lossless transmission line, the impedance along the length of the transmission line is given by Equation (2.71) [7, p. 56-59].

$$Z_{\mathrm{in}} = Z_0 \cdot \frac{\mathrm{e}^{j\beta l} + \Gamma \mathrm{e}^{-j\beta l}}{\mathrm{e}^{j\beta l} - \Gamma \mathrm{e}^{-j\beta l}} \qquad [\Omega] \quad (2.71)$$

Where:

Z_0	=	characteristic impedance of lossless transmission line	$[\Omega]$
β	=	propagation constant $\beta = \frac{2\pi}{\lambda}$	$\left[\mathrm{rad\,m^{-1}}\right]$
l	=	distance from termination along transmission line	[m]
Γ	=	reflection coefficient at the termination	[1]

At the start of the quater-wave impedance transformer the input impedance is given by Equation (2.72).

$$Z_{\mathrm{in,T}} = Z_T \cdot \frac{1 - \Gamma_{\mathrm{pd}}}{1 + \Gamma_{\mathrm{pd}}} \implies Z_{\mathrm{in,T}} = \frac{Z_T^2}{Z_{\mathrm{in,pd}}} \qquad [\Omega] \quad (2.72)$$

For impedance matching $Z_1 = Z_{\mathrm{in,T}}$, and the characteristic impedance of the quarter-wave impedance transformer Z_T can be derived as Equation (2.73)

$$Z_T = \sqrt{Z_1 \cdot (Z_2 || Z_3)} \qquad [\Omega] \quad (2.73)$$

In the case of $Z_1 = Z_2 = Z_3 = 50\,\Omega$, Equation (2.73) yields $Z_T = \sqrt{50 \cdot (50||50)} = 35.355\,\Omega$.

3 STATE OF THE ART - LITERATURE STUDIES

This chapter presents different designs, techniques and technologies related to the scope of this thesis. Topics include excitation of circular polarized modes, compact single- and dual-band antenna element designs, and methods to alter the bandwidth of planar antennas.

3.1 EXCITATION OF CIRCULAR POLARIZED MODES

Section 2.9 presents different patch antenna excitation methods to achieve circular polarization. In this chapter some additional methods of achieving circular polarization with patch antennas are presented.

3.1.1 HAIRPIN RESONATOR FEED

Circular polarization can be achieved by exploiting that the coupling between two resonators acts as admittance inverters with $-90°$ phase shift [12]. Figure 3.1 shows an example where the path from the feed to the horizontal mode passes through a hairpin resonator and a non-resonant coupling slot (Slot-1), totalling $-180°$ phase shift. The path from the feed to the vertical mode passes through the same hairpin resonator as well as a resonant slot (Slot-2), totalling a $-270°$ phase shift. Through the shown feeding structure a $-90°$ phase shift is realized for the two orthogonal modes, resulting in circular polarization.

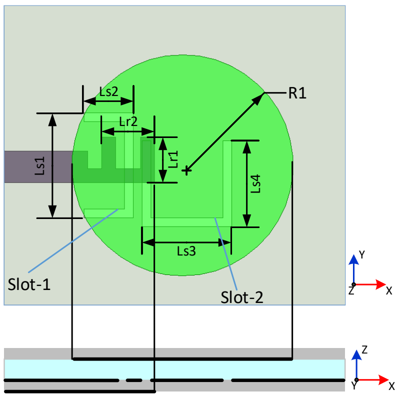

Figure 3.1: 3 layer circular patch antenna design with coupled hairpin feeding structure. The bottom layer is microstrip, middle layer is a slotted ground plane, and the top layer is a circular patch antenna. Slot-1 is non resonating and slot-2 is resonating causing a −90° phase shift to realize circular polarization. [12]

A similar design at X-band using a square patch and Rogers RT5870 laminate as substrate has been simulated. The design is found to achieve similar results compared to the other methods of achieving circular polarization.

3.1.2 GROUNDED PATCH

Circular polarization can be achieved by adding ground pins to the patch [13]. Figure 3.2 shows an illustration of the grounded patch antenna structure. By enlarging the patch and adding the ground pins it is possible to achieve a higher circular polarized gain. This is because the ground pins increases the resonant length of the two linear modes.

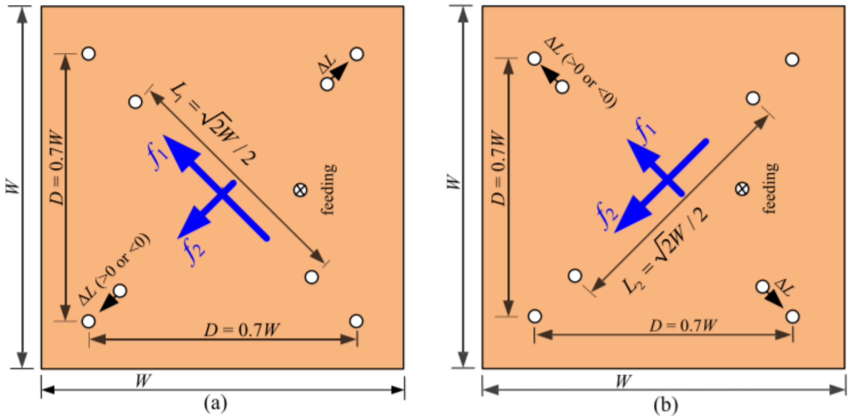

Figure 3.2: Patch antenna with groundning pins achieving circurlar polarization [13].

With this method of achieving circular polarization, it is possible to achieve a significant improvement in the antenna gain at the cost of a bigger antenna area.

3.2 ALTERING IMPEDANCE BANDWIDTH OF PLANAR PATCH ANTENNAS

The Impedance bandwidth of an antenna is an important performance metric.

Figure 3.3 shows two different designs implementing the antenna structure as a coupled filter.

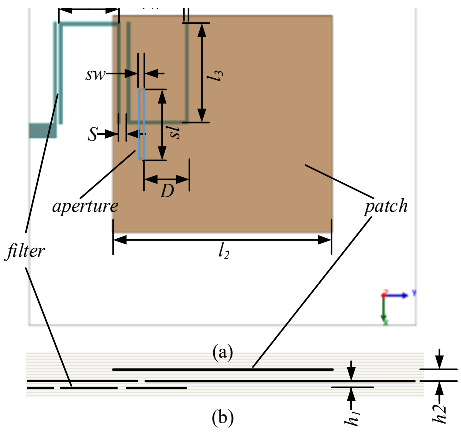

(a) Three layer filtering antenna. Top later is a patch antenna, middle layer is a slotted ground plane, and the bottom layer is a microstrip feed with two hairpin resonators. [14]

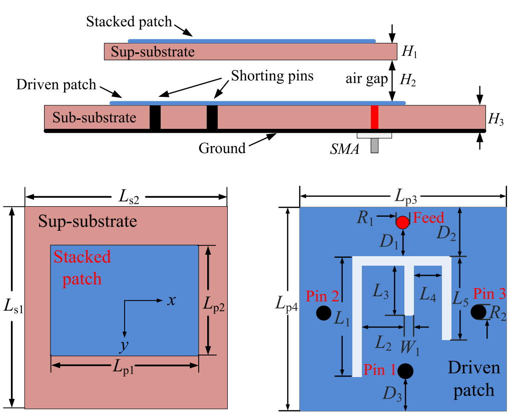

(b) Three layer filtering antenna. Top layer is patch antenna, middle layer is slotted and grounded patch antenna, and bottom layer is a full ground plane. [15]

Figure 3.3: Two different filtering antenna designs.

The design in Figure 3.3a [14] uses two hairpin resonators and a slotted ground plane to allow coupling between the second resonator and the patch antenna. These two hairpins adds two additional resonances, thus widening the impedance bandwidth. The presented design shows equal maximum gain, a wider bandwidth, and a higher out of band attenuation, compared to a traditional aperture feed design.

Figure 3.3 [15] shows a design without resonators in the feeding network. Two patches are stacked and the lower patch is exited by a feed probe. The lower patch is slotted and grounded through pins to introduce additional resonances. The design is optimised to attenuate out-of-band frequencies by achieving a sharp frequency dependent gain response.

3.3 DUAL-BAND ANTENNA DESIGNS AND STRUCTURES

Figure 3.4 shows two antenna element layouts which enables dual-band operation [16, 17].

In Figure 3.4a slim S-band patch antennas are placed along the edge of a nano-satellite face, leaving the center surface space free for other uses. The middle of the nano-satellite face can be used for X-band operation. The S-band patch antennas along the edge are too slim to support two orthogonal modes for circular polarization, so circular polarization is realized by feeding the elements A, B, C, and D with relative phases 0°, −90°, −180°, and −270° respectively.

Figure 3.4b shows an alternate layout with S-band elements centred on the nano-satellite face and X-band patch antennas placed in the corners. In [17] this layout is used to realize linear polarization, but antenna layout also allows supports circular polarization by altering excitation since all the patches have equal widths and lengths.

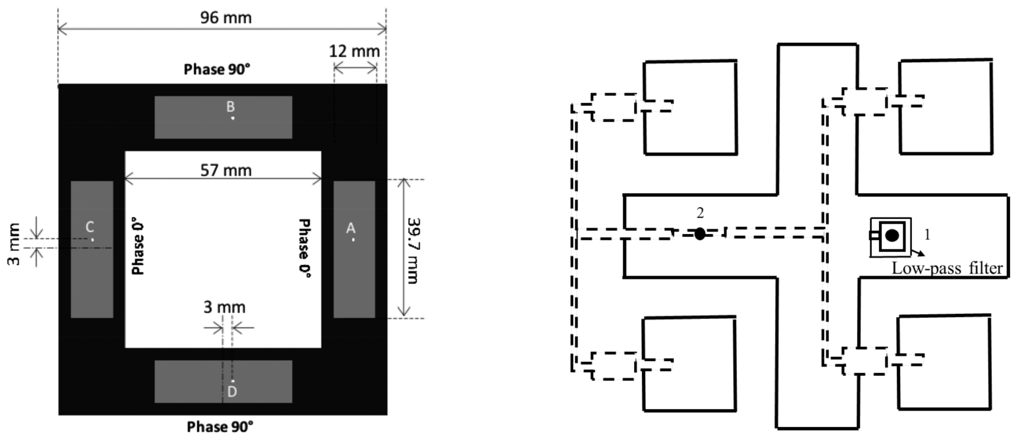

(a) Arrangement of slim S-band radiating elements. Space in middle is used for camera in intended application. [16]

(b) S- and X-band linearly polarized antenna design [17]. Similar antenna element layout is also presented in [18] however without higher-order mode suppression.

Figure 3.4: Two different antenna layouts enabling dual-band operation.

Figures 3.5 and 3.6 shows alternate dual-band designs where the same aperture is used for two different bands, either by exploiting the unused space in an annular slot antenna or by stacking patch antennas tuned for different frequencies [19, 20].

In Figure 3.5 two annular aperture antenna elements with a frequency ratio of approximately 1:1.5 are integrated into the same area. The higher frequency element is placed in the center of the lower frequency element.

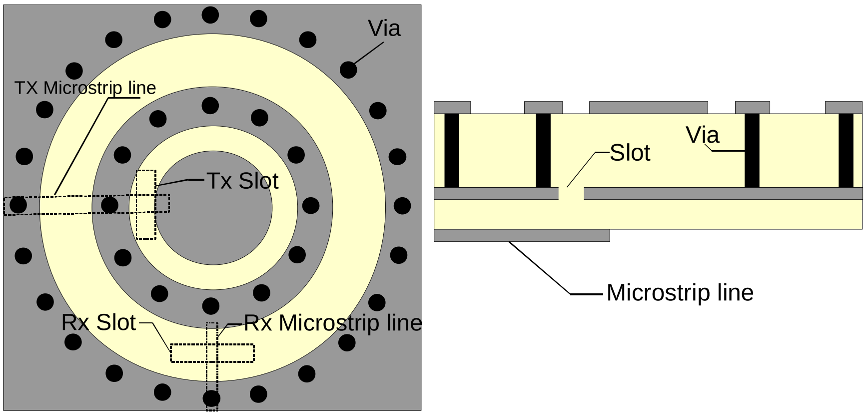

Figure 3.5: K and Ka (21 GHz and 30 GHz) Dual-band aperture antenna element design. Left picture shows the top layer with lower layers displayed as dotted lines. Right figure shows a cross-sectional view of the antenna element. Vias are connected to ground layer below to provide a conducting wall to minimize mutual coupling between the two radiating aperture rings. [19]

To combat the inherent mutual coupling between the two annular apertures, they are separated by a "conducting wall" consisting of grounded Vertical Interconnect Accesss (VIAs). An antenna gain of approximately 4.6 dB is achieved with an isolation of 30 dB between the two ports in both bands. [19]

In Figure 3.6 dual-band operation is achieved by stacking two patch antennas with a frequency ratio of 1:1.4, with the high frequency patch placed centred and above the low frequency patch.

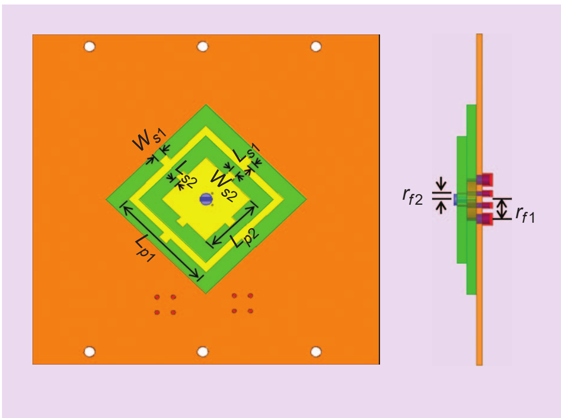

Figure 3.6: S- and L-band circularly polarized antenna design. [20]

Circular polarization of the stacked patches is achieved by using two feeds for each patch split by 90° hybrid couplers.

3.4 STATE OF THE ART CONCLUSION

As seen from Sections 2.9 and 3.1 circular polarization can be realized for patch antennas in different ways. Most methods are comparable i terms of performance. However it is noted that the methods which uses ground pins to achieve circular polarization has a larger antenna area thus also a higher realized gain.

Section 3.2 presents different methods of achieving a desired impedance bandwidth. Common for the different techniques are their added complexity. The desired impedance bandwidth is achieved by adding additional resonances to the antenna feed or the antenna structure.

Section 3.3 presents different dual-band antenna structures and designs. The dual band antenna designs in Figures 3.5 and 3.6 both show good performance. However the frequency ratio of the presented designs are 1.375 and 1.45. For an S- and X-band antenna the ratio is around 4.

The designs shown in Figure 3.4 are deemed as feasible for this thesis. The design shown in Figure 3.4b is presented with a frequency ratio in the desired range and the design shown in Figure 3.4a has an area of free space, which could be used for X-band antennas. As detailed in Section 4.1 these two designs are chosen as the inspiration of the proposed solutions.

4 REQUIREMENTS AND SOLUTION PROPOSALS

In this chapter, the antenna requirements are presented. For this thesis, a set of requirements is supplied. Table 4.1 shows an interpretation of the supplied requirements.

Table 4.1: Table with antenna requirement.

Performance metric	*Requirement*	
Band	S-Band	X-Band
Bandwidth	1.97 to 2.03 GHz	8 to 8.5 GHz
Realized RHCP gain	$\geq$ 6 dB	$\geq$ 12 dB
HPBW	$\pm$20 deg	$\pm$10 deg
Cross-coupling	≤ -25 dB	
Port reflection	≤ -10 dB	
Port input impedance	50 Ω	
Antenna dimensions (WxL)	100 by 100 mm	
Antenna height (incl. mounting fixture)	$\leq$ 7 mm	
Grounding	All metals $\geq$ 100 mm must be grounded	

A short analysis of the feasibility of the requirements is conducted. The feasibility analysis is conducted by comparing the requirements against the performance of a few selected commercially available products.

The S-Band antenna requirements are compared to the performance of a NanoCom ANT2000 [21]. The NanoCom ANT2000 is an S-band nano-satellite antenna produced by GOMspace. This antenna measures 82.6 by 100.5 mm. The antenna has a height of approximately 9.4 mm, excluding the bottom mounted lumped elements. This antenna achieves $\geq$ 7 dB realized RHCP gain in a wide S-band frequency range and has an impedance bandwidth of approximately 300 MHz.

The company Endurosat has different X-band antenna designs. They produce an antenna called X-Band 4 Element Patch Antenna Array [22]. The antenna measures 60 by 60 mm. It has an impedance bandwidth of around 500 MHz. It has a realized RHCP gain of around 12 dB in the 8.0 to 8.5 GHz frequency range.

The comparison of the commercially available antennas and the requirements shows that products which partially satisfies the requirements are available. No product which satisfies all the requirement was found to be available. The NanoCom ANT2000 antenna satisfies the S-band requirements and the X-band antenna available from Endurosat satisfies the X-band antenna requirements.

Since separate antennas for the two bands which satisfy the requirements, with a fair margin, are available the supplied requirement specification is deemed feasible.

4.1 SOLUTION PROPOSAL

With the requirement specification presented, this section presents two solution proposals.

Different antenna structures exist however for this thesis the two antenna structures shown in Figure 4.1 are chosen. Both these structures are constructed from patch antenna elements.

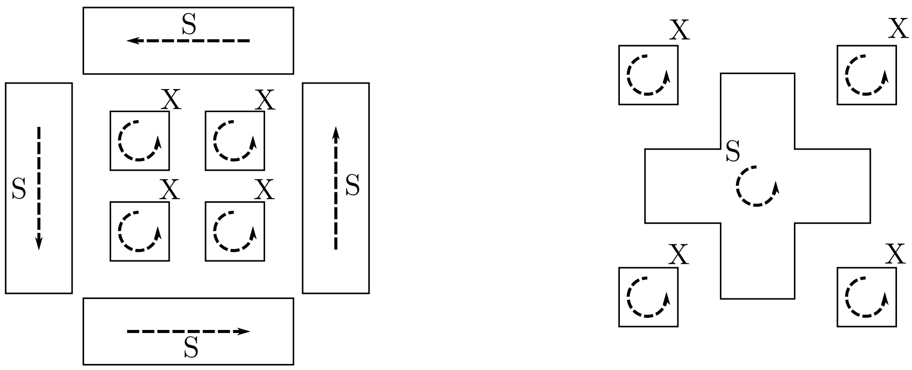

(a) Separate aperture topology. Four X-band antenna elements in the center of the board, and S-band antenna elements along the edge. The arrows indicate polarization. S-band antennas a linearly polarized, but excited sequentially to produce RHCP. X-band antennas are RHCP.

(b) Shared aperture topology. There are X-band antenna elements in the corners of the board, and S-band cross shaped antenna element in the center. The arrows indicate polarization. S-band antenna is RHCP by exciting the two supported linear modes sequentially. X-band antennas are RHCP.

Figure 4.1: Different possible topologies for the dual-band S- and X-band antenna.

Figure 4.1a shows a dual-band antenna structure with eight patch antenna elements. This structure is named "Separate aperture" (SepAp). This structure is an extension to the antenna seen in Figure 3.4a. The dual-band nature is achieved with this design by having a two-by-two X-band antenna array surrounded by four S-band patch antenna elements.

It is shown in Section 2.9 how patch antenna elements require two perpendicular standing waves excited with a 90° difference to achieve circular polarization. This layout only allows for placement of slim S-band antenna elements along the edge of the board. The narrow width of the S-band patch antenna does not allow the individual patch antenna elements to achieve circular polarization, since they do not support a half standing wave. Instead, RHCP is realized by exciting the vertically and horizontally polarized patches 90° apart. To fulfil the required 6 dB RHCP gain in the S-band, the individual S-band antenna elements must have a realized linear gain $\geq 3\,\text{dB}$.

Figure 4.1b shows an antenna structure topology with a cross-shaped S-band patch antenna element surrounded by a two-by-two array of X-band patch antenna elements. This antenna design structure is named "Shared aperture" (Cross). The cross-shaped S-Band antenna element achieves circular polarization by having two feeding points. One feeding point on each of the two perpendicular lengths. The two feeding points must be excited with a 90° phase shift to achieve circular polarization.

For both designs, a two-by-two patch antenna array is used for the X-band. As seen in Section 2.9, a square patch antenna can easily achieve circular polarization. As described in Section 2.10, a two-by-two antenna array will have a theoretical array gain in the broadside direction of 6 dB, since each time the number of antennas in a planar array is doubled, the broadside gain increases by approximately 3 dB. Thus the individual X-band antenna elements must have a realized RHCP gain $\geq$ 6 dB to satisfy the requirement specification.

Appendix A finds that the maximum broadside gain of a standard X-band RHCP patch antenna is approximately 7 dB on RO4003C substrate with a height of $h = 1.524$ mm. Thus it is estimated that the designs have the potential to satisfy the gain requirements. The X-band antenna arrays are arranged in a square shape because it is shown in Appendix E to yield better performance compared to a diamond-shaped arrangement.

The S-band patches of both designs shown in Figures 4.1a and 4.1b are narrow compared to the width given in Equation (2.25). Section 2.7.1 and Appendix C shows that the gain of a patch antenna is reduced when the width of the patch is reduced, however, simulations show that an S-band patch antenna on 1.524 mm of RT5870 substrate material and a width of 16 mm achieves a realized gain of 5.87 dB. This indicates that the S-band gain requirements can be satisfied by both antenna structures.

It is chosen to use probe feeds to excite the antenna elements for both designs due to their simplicity and nearly identical performance when compared to other common methods. Aperture or proximity feeds could, however, ease fabrication due to the need for fewer VIAs.

The feed network is made from stripline, to shield the feeding network from the antennas and the rest of the nano-satellite structure behind the antenna.

During the iterative design procedure, it is found that a substrate with a relative permittivity of $\epsilon_r = 2.33$ gives a good compromise between gain, size, and coupling between antenna elements. It is desired to use a substrate with as low a relative permittivity as possible to increase patch antenna surface area and thereby gain, while still having space to fit all the required elements onto the 1 U nano-satellite face. The Rogers RT5870 laminate [23] substrate is used for both of the two proposed designs.

With both the requirement specification and the two solution proposals presented, the next two chapters present the design of the proposed antenna structures.

5 SOLUTION 1: SHARED APERTURE (CROSS)

As detailed in Section 4.1 two antenna designs are to be designed. In this section, the first of the two designs called Shared aperture, Cross for short, is designed. As detailed in Section 4.1 this design consists of a cross-shaped S-band patch antenna and an array of four X-band patch antenna elements.

The S-band antenna has to be cross-shaped to allow space for the X-band array. The effect of reducing the width of a patch antenna is a lower gain and impedance bandwidth, as seen from Appendix C. However with the space limitations it is not feasible to have a full-sized S-band patch antenna. The primary goal of this design proposal is to find a good compromise between the size of the cross-shaped S-band antenna and the space allocated to the X-band array.

The X-band elements achieve circular polarisation by trimming the corners of the patches. The cross achieves circular polarization by having two feeding points exited with a 90° phase difference.

In order to satisfy the requirement specified in Chapter 4, it is found that a stacked antenna structure for both antenna frequency bands is required.

Figure 5.1 shows an illustration of the stack-up. The stack-up has five substrate and copper layers. Counting from the bottom, the first and the third copper layers are the ground layers. The second copper layer is the feed network. The fourth and the fifth layers are the two patch layers.

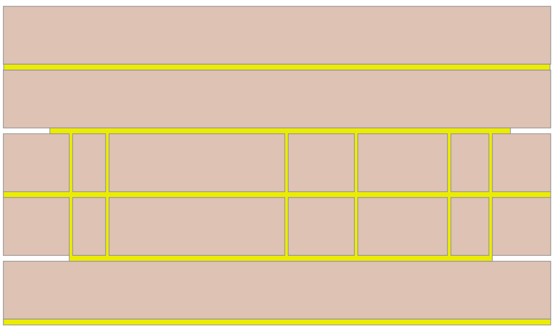

Figure 5.1: Cross-section of the antenna stack-up.

The final overall structure of this antenna design is shown in Figure 5.18 and the final evaluation of the achieved performance in Table 5.3.

To simplify the design of the antenna, the design is split into multiple parts. First, the S-band cross is designed. Secondly, the X-band antenna element is designed. Lastly, a feeding network is added and the performance of the combined antenna structure is presented.

5.1 S-BAND ANTENNA ELEMENT

The idea of stacking the S-Band cross is to have two slightly offset resonance frequencies, one for each cross-shaped patch.

Figure 5.2a shows the CST model of the antenna, with the antenna element and feeding striplines highlighted.

The dimensions of the stacked cross-shaped S-band patch antenna is seen in Table 5.1.

Table 5.1: Dimensions of the stacked cross-shaped S-band antennas.

Parameter	*Size*
Substrate Type	RT5870
Substrate Height (Under Lower Patch)	1.575 mm
Substrate Height (Between Patches)	1.575 mm
Substrate Height (Over Upper Patch)	0.305 mm
Substrate Height (Feeding)	0.203 mm
Feed Line Height	0.017 mm
Feed line Width	0.25 mm
Feed Line Length	To the edge of the board
Patch Length Upper	51.75 mm
Patch Width Upper	16 mm
Patch Length Lower	51.55 mm
Patch Width Lower	16 mm
Feeding point (Distance from center)	7.60 mm
Feed Pin radius	0.125 mm
Ground Cut out Radius	0.9 mm
Board Size	90 mm

Figure 5.2b shows the radiation pattern of the stacked S-band cross. The realized RHCP gain in the main direction is 6.45 dB. The 6.00 dB gain requirement is satisfied.

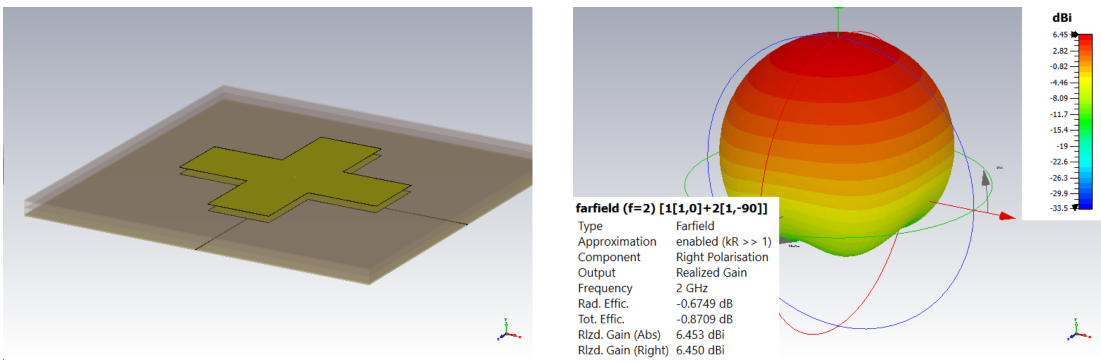

(a) Model of the stacked cross-shaped S-band antenna with the antenna element and feeding highlighted.

(b) Simulated radiation pattern of the stacked cross-shaped S-band antenna.

Figure 5.2: Model and simulated radiation pattern of the stacked cross-shaped S-band antenna.

Figure 5.3 shows the S-parameters of the stacked cross-shaped S-band patch antenna. The impedance bandwidth is 64 MHz. The 60 MHz impedance bandwidth requirement is satisfied.

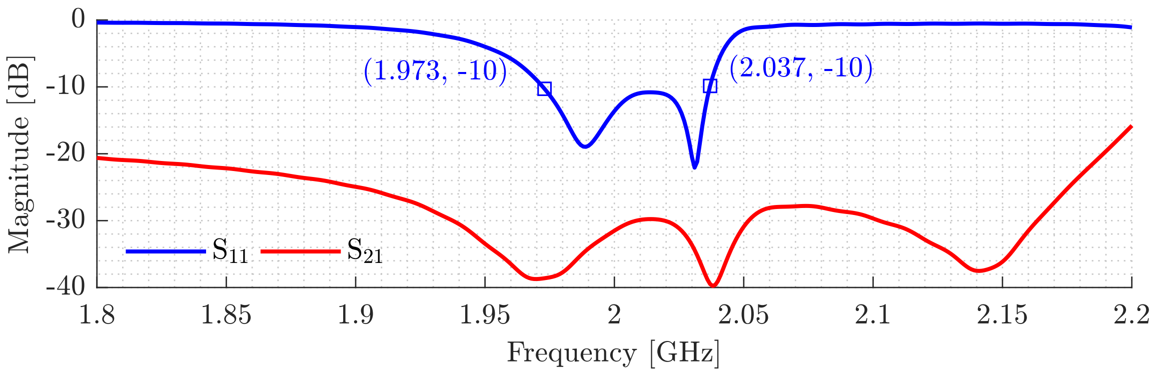

Figure 5.3: Simulated S-parameters of the stacked cross-shaped S-band antenna.

Figure 5.4 shows the realized gain of the stacked S-band cross-shaped patch antenna. From the figure, it is seen that the antenna design does not have the required realized RHCP gain of ≥ 6 dB in the full 1.97 to 2.03 GHz frequency range. However the effect of surrounding the cross-shaped antenna by the X-band antenna elements is still unknown, therefore the design of the S-band part of the antenna is deemed sufficient for the time being. If required the stacked cross-shaped S-band antenna is re-evaluated after the X-band part of the antenna proposal has been concluded.

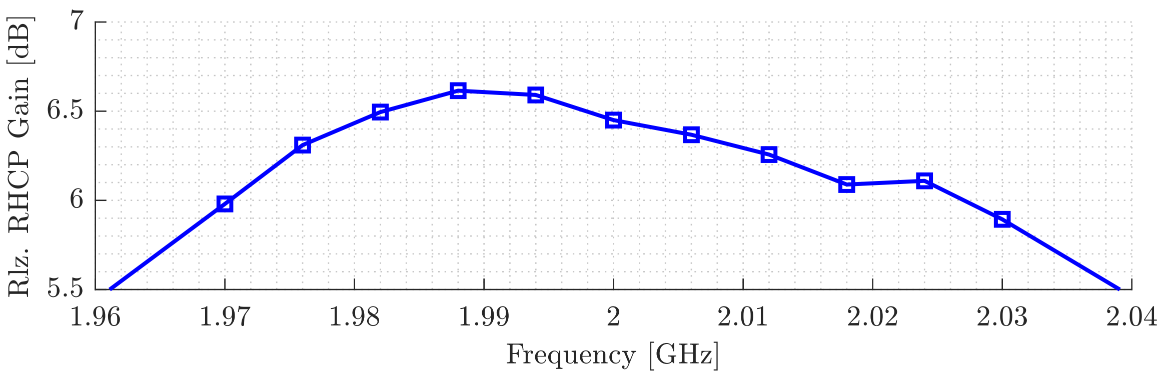

Figure 5.4: Simulated broadside realized RHCP gain of the stacked cross-shaped patch antenna.

With the S-band antenna element concluded, the next section designs the X-band patch antenna elements.

5.2 X-BAND ANTENNA ELEMENTS

A stacked corner trimmed X-band patch antenna is designed in this section.

By stacking two corner trimmed X-band patch antenna elements the radiation pattern of the patch antenna can be more guided and achieve a higher gain in the main direction, at the cost of beam width.

Figure 5.5a shows a CST model of the stacked corner trimmed X-band patch antenna.

The dimensions of the stacked corner trimmed X-band patch antenna is seen in Table 5.2.

Table 5.2: Dimensions of the stacked corner trimmed X-band patch antenna.

Parameter	*Size*
Substrate Type	RT5870
Substrate Height (Under Lower Patch)	1.575 mm
Substrate Height (Between Patches)	1.575 mm
Substrate Height (Over Upper Patch)	0.305 mm
Substrate Height (Feeding)	0.203 mm
Feed Line Height	0.017 mm
Untrimmed Patch Length (Upper)	9.70 mm
Untrimmed Patch Width (Upper)	9.70 mm
Patch Corner Trim (Upper)	4.55 mm
Untrimmed Patch Length (Lower)	10.3 mm
Untrimmed Patch Width (Lower)	10.3 mm
Patch Corner Trim (Lower)	4.50 mm
Feed line Width	0.25 mm
Feeding point (Distance from center)	3.80 mm
Feed Pin radius	0.125 mm
Ground Cut out Radius	0.70 mm
Feeding cut inner diameter	1.65 mm
Feeding cut outer diameter	1.95 mm
Board Size	95 mm

Figure 5.5b shows the radiation pattern of the stacked X-band patch. The antenna has a realized RHCP gain of 7.26 dB at 8.25 GHz. Thus the 6.0 dB gain requirement is satisfied.

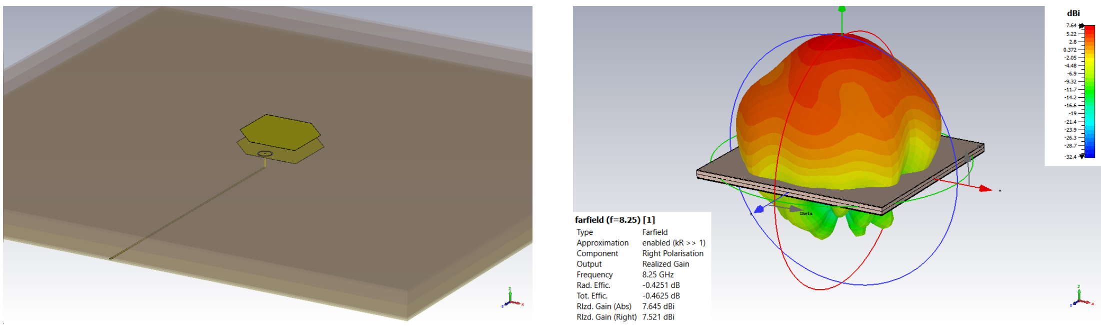

(a) Model of the stacked corner trimmed X-band patch antenna.

(b) Simulated radiation pattern of the stacked corner trimmed X-band antenna.

Figure 5.5: model and radiation pattern for the stacked corner trimmed X-band antenna.

Figure 5.6 shows the S_{11} parameter of the stacked corner trimmed patch antenna. The impedance bandwidth satisfies the $\geq 10\,\mathrm{dB}$ return loss in the 8 to 8.5 GHz frequency band.

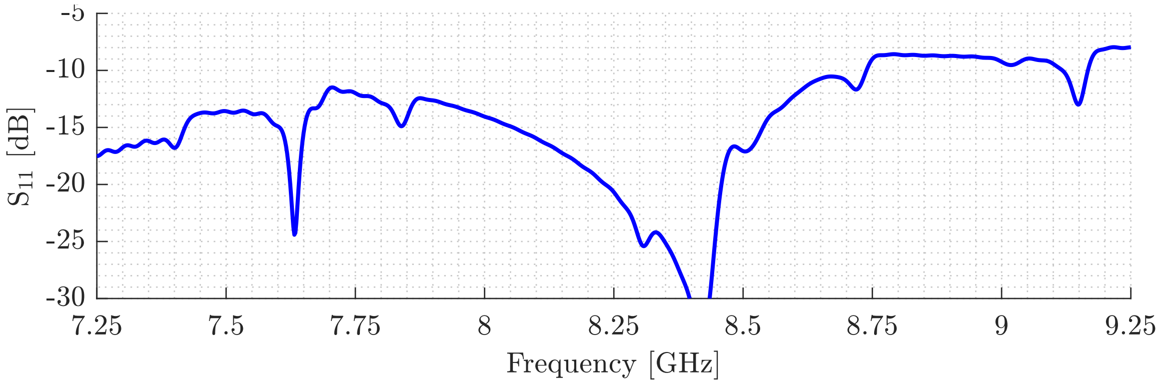

Figure 5.6: Simulated S-parameters of the stacked corner trimmed X-band antenna.

Figure 5.7 shows the realized RHCP gain of the antenna. The antenna has a realized RHCP gain between 7.3 to 7.5 dB in the full 8.0 to 8.5 GHz frequency range. The gain requirement is satisfied with a margin available for losses such as the feeding network loss.

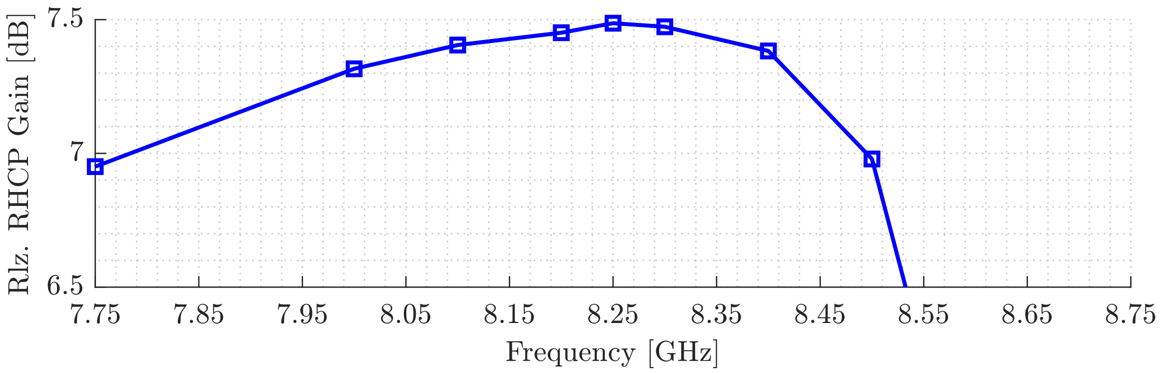

Figure 5.7: Simulated broadside realized RHCP gain of the stacked corner trimmed X-band patch antenna.

Figure 5.8 shows the simulated axial ratio of the stacked corner trimmed X-band patch antenna. The axial ratio is $\leq 3\,\mathrm{dB}$ in the desired frequency range.

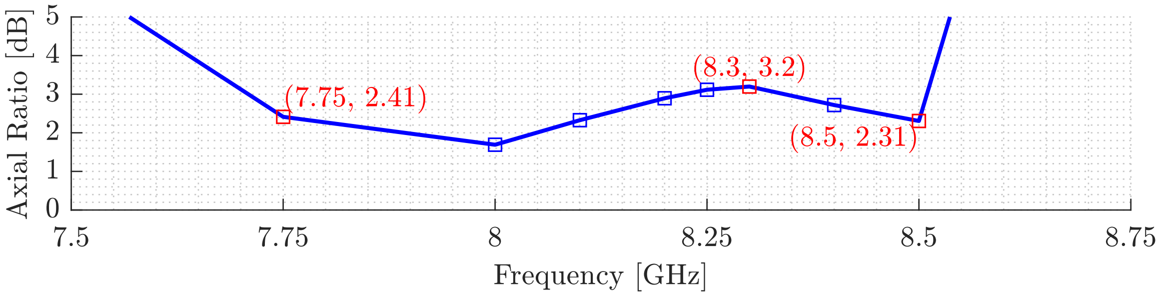

Figure 5.8: Simulated broadside axial ratio of the stacked corner trimmed X-band patch antenna.

With both the S- and X-band antenna elements designed the next chapter presents the performance of the combined antenna structure.

5.3 COMBINED ANTENNA STRUCTURE

Figure 5.9a shows the final combined antenna structure. The X-band antenna elements are separated with a center-to-center distance of 45 mm, which is approximately 1.25λ. This results in significant side-lobes when the radiation pattern of the four patch antenna elements are combined. Stronger side-lobes are undesired, however, it is a necessary compromise for this design topology.

As seen from Figure 5.9a copper guides are added at the corners of the board. These guides are used to guide the radiation of the X-band patch antennas. With the configuration seen in Figure 5.9a each X-band patch antenna element has an undesired radiation pattern similar to an isolated stacked patch from Appendix F on a ground plane of 60 by 60 mm. Appendix G shows that a grounded copper guide at the edge of the board can help solve this problem. Copper guides are only added at the corners of the board to ensure that the guides do not effecting the radiation from the S-band antenna elements.

Figure 5.9b shows the combined antenna radiation pattern of the X-band antenna elements. The realized RHCP gain is simulated to be 12.8 dB at 8.25 GHz. In the S-band the two linear modes of the cross-shaped patch is combined to give RHCP radiation with a pattern virtually unchanged from the isolated case in Figure 5.2.

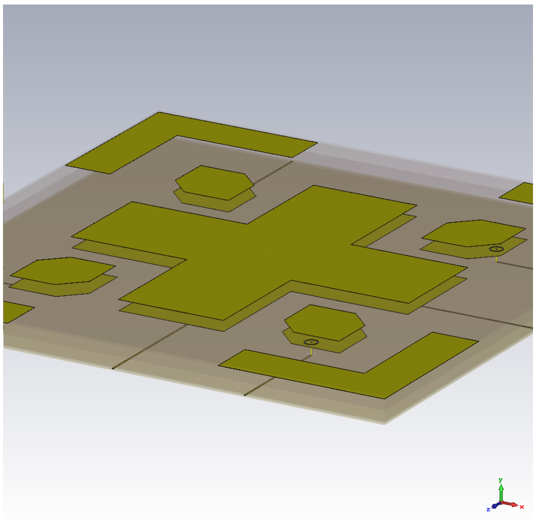

(a) Model of the combined antenna structure with the antenna elements and the stripline feed highlighted.

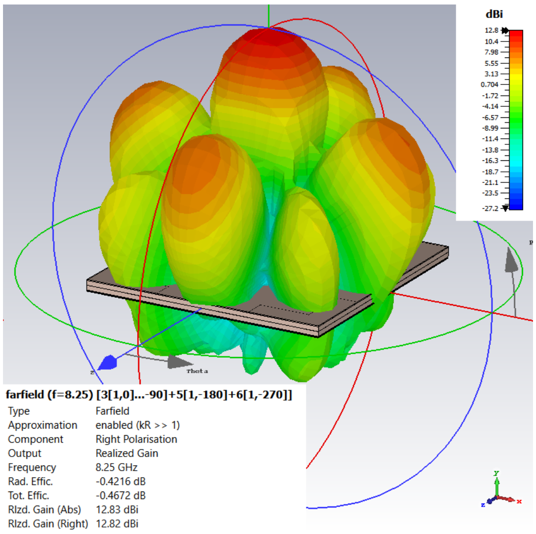

(b) The simulated radiation pattern of the X-band part of the combined antenna design.

Figure 5.9: Model and simulated X-band radiation pattern of the antenna with individual stripline feeds.

Figure 5.10 shows the realized RHCP gain of the four X-band antenna ports and of the combination of the ports. The individual antennas have realized RHCP gains between 6.6 to 7.15 dB. When the antenna ports are combined a realized RHCP gain of ≥ 12.75 dB is achieved in the full 8 to 8.5 GHz frequency band.

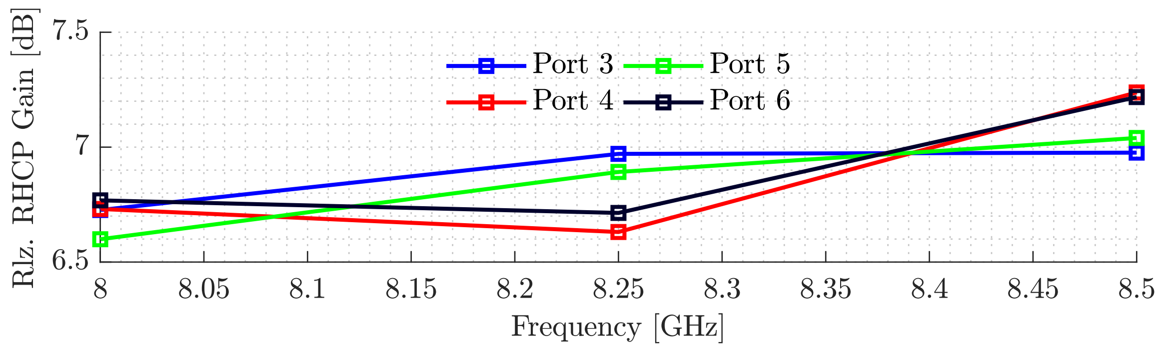

(a) Individual broadside realized RHCP gain. Ports three to six are the X-band antenna element ports.

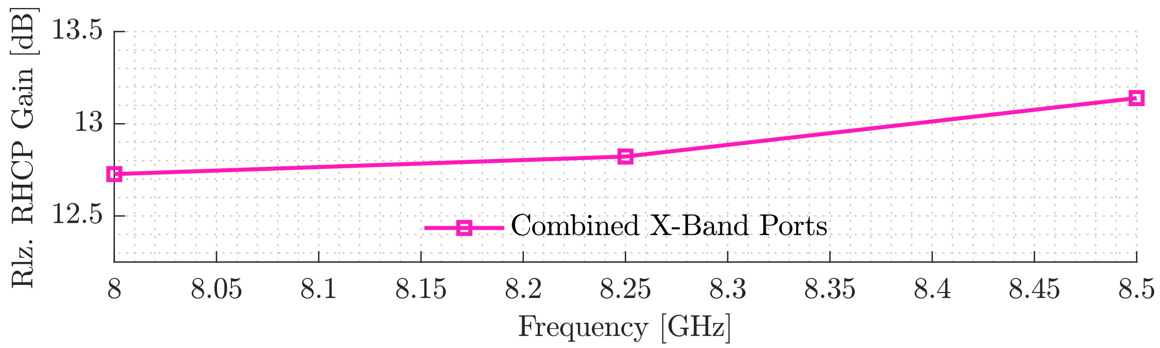

(b) Combined broadside realized RHCP gain.

Figure 5.10: Simulated broadside realized RHCP gain of the X-band antenna elements in the combined structure.

Figures 5.11 and 5.12 show the cross-coupling of the combined antenna structure. Figure 5.11 shows that the antennas couple less than −35 dB in the 1.97 to 2.03 GHz frequency range. Figure 5.12 shows how the antenna coupling is below −21 dB in the 8.0 to 8.5 GHz frequency range.

The cross-coupling requirement is, that the antennas should couple less than −25 dB. Thus the cross-coupling requirement is expected to be satisfied as the feeding network adds additional losses.

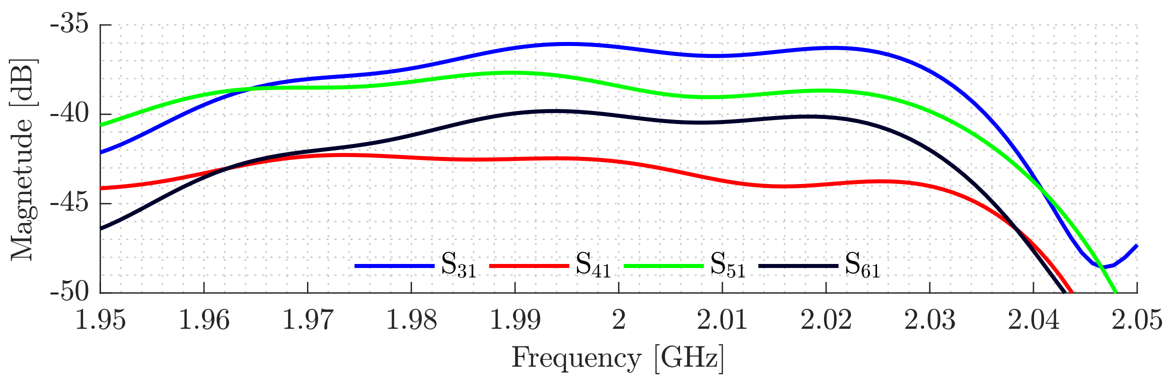

Figure 5.11: Simulated cross-coupling of the combined antenna structure at S-band.

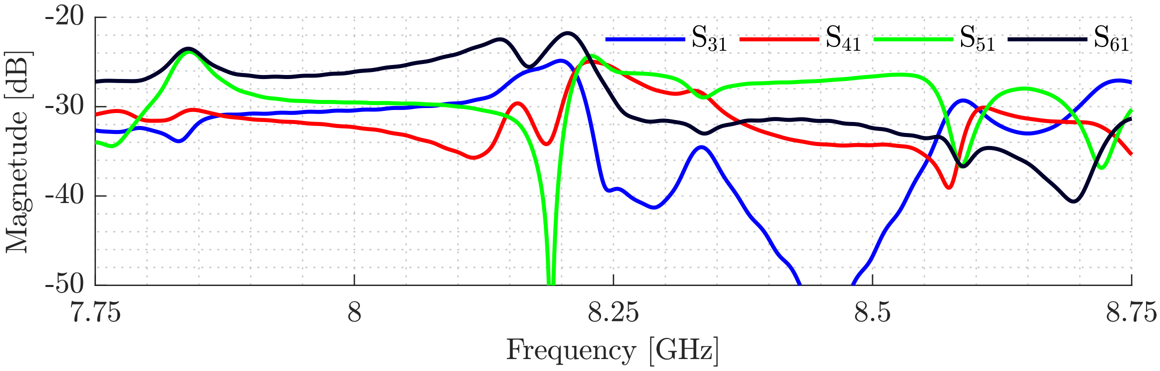

Figure 5.12: Simulated cross-coupling of the combined antenna structure at X-band.

The simulation results presented in this section show that the X-band part of the antenna satisfies the set X-band requirements. The X-band antenna is shown to have a $\geq 0.75\,\mathrm{dB}$ gain margin to cover the loss of the feeding network. The S-band part of the design does not satisfy the gain requirement at the edges of the frequency band and has no significant margin to compensate for the losses of the feeding network. However, the S-band antenna is deemed sufficient for the time being and the feeding network is designed.

5.4 FEED NETWORK DESIGN

In this section the feeding network is designed. The purpose of the feeding network is to divide the input power to the antenna elements with the correct phase delay. To do the power division T-junction power dividers with quarter wave transformers, described in Section 2.11, are used.

The X-band input port is split into four output ports, one for each antenna element, thus three power dividers are needed. For the S-band a single power divider is used.

A model of the feeding network is seen in Figure 5.13. In this model, the antenna elements and their feeding probes are replaced by waveguide ports. This allows simulations of the feeding network alone.

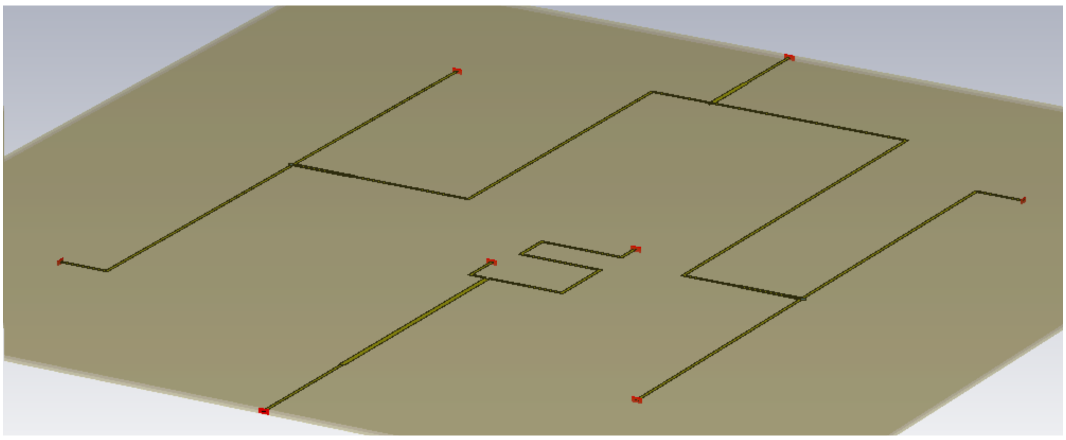

Figure 5.13: CST model of the feeding network. Antennas and their feeding pins are replaced by waveguide ports.

The S-band power divider has a $35\,\Omega$ quarter-wave transformer with a stripline width of 0.475 mm and a length of 25 mm. The X-band power dividers have $35\,\Omega$ quarter-wave transformers with a stripline width of 0.475 mm and a length of 5.85 mm.

As illustrated in Figure 5.13 the required 90° phase shift for the S-band antennas is made by adding more stripline length between the power divider and one of the antenna ports. The extra line length is added to the rightmost port to achieve RHCP radiation.

Figure 5.13 also shows that the phase delays for the X-band patches are achieved by simply having the feed network asymmetrical. The two leftmost antennas have shorter striplines since the first power divider placed left from the center. Likewise, the bottom left and the top right antennas have longer stripline lengths compared to the top left and the bottom right, respectively, because the second power dividers are placed offset from the center-axis.

The port to antenna stripline length for the four X-band ports is between 80 to 100 mm. The loss in a 100 mm stripline at 8.5 GHz is found in Appendix D to be -0.47 dB. The loss of the X-band power divider is 0.13 dB. Thus the total expected minimum loss of the X-band feed network is $2 \cdot 0.13\,\text{dB} + 0.47\,\text{dB} = 0.73\,\text{dB}$.

Figure 5.14 shows the simulated magnitude of the S-parameters for the X-band part of the antenna feeding network. A loss of as much as 0.93 dB at 8.14 GHz is observed. The variation in loss is likely caused by the difference in the feeding stripline length. The simulated loss is higher than the expected minimum. With a loss between 0.31 to 0.95 dB at 8.25 GHz, the feeding loss is within the margin of acceptable loss. Thus no further iterations are required.

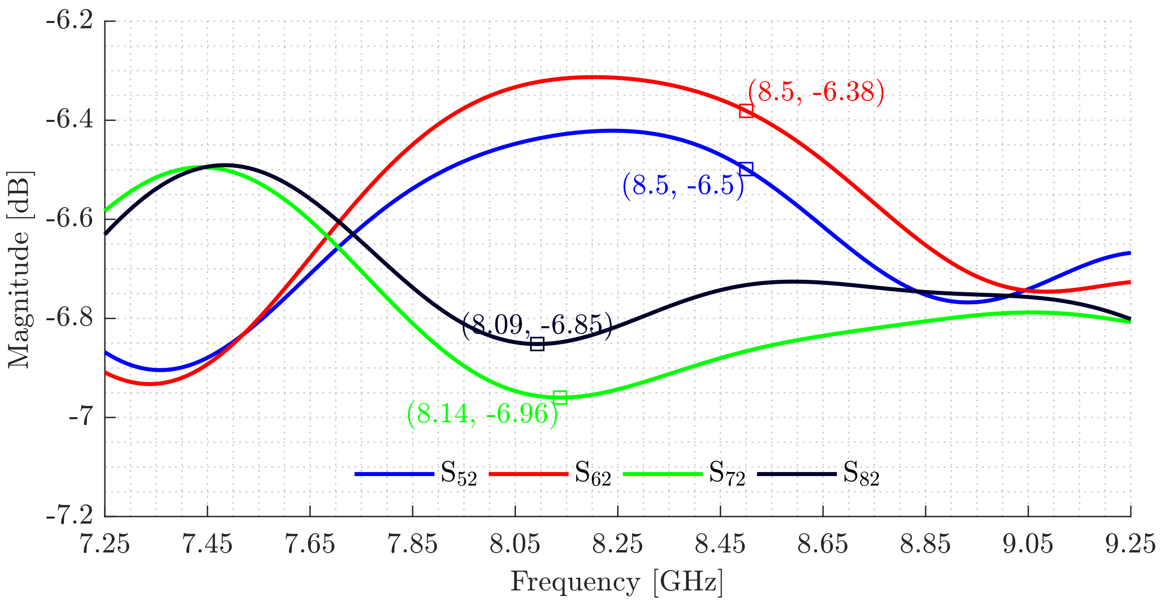

Figure 5.14: Simulated S-parameter magnitude for the X-band feeding network.

Figure 5.15 shows the simulated magnitude of the S-parameters for the S-band part of the antenna feeding network. The S-band feeding network causes a loss of approximately 0.1 dB at 2 GHz.

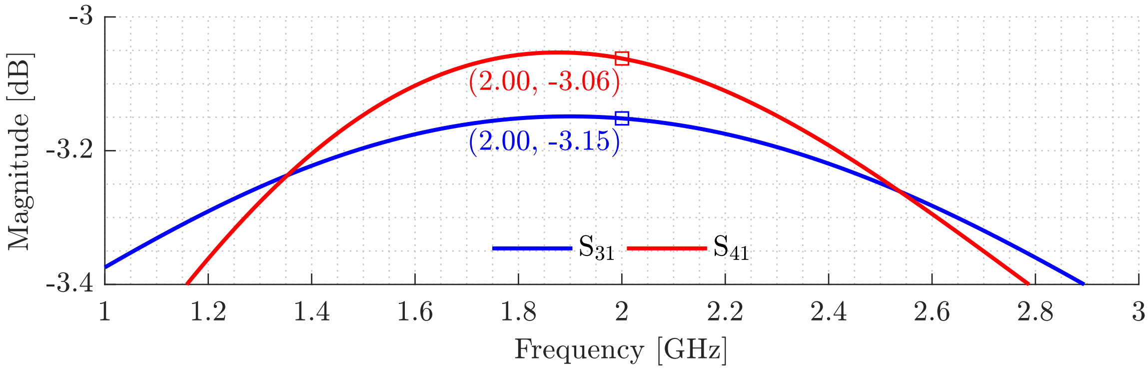

Figure 5.15: Simulated S-parameter magnitude for the S-band feeding network.

Figure 5.16 shows the simulated phase of the S-parameters for the X-band part of the antenna feeding network. Figure 5.17 shows the simulated phase of the S-parameters for the S-band part of the antenna feeding network. It is seen from the figures that the phase difference between the ports are approximately equal to the required 90°.

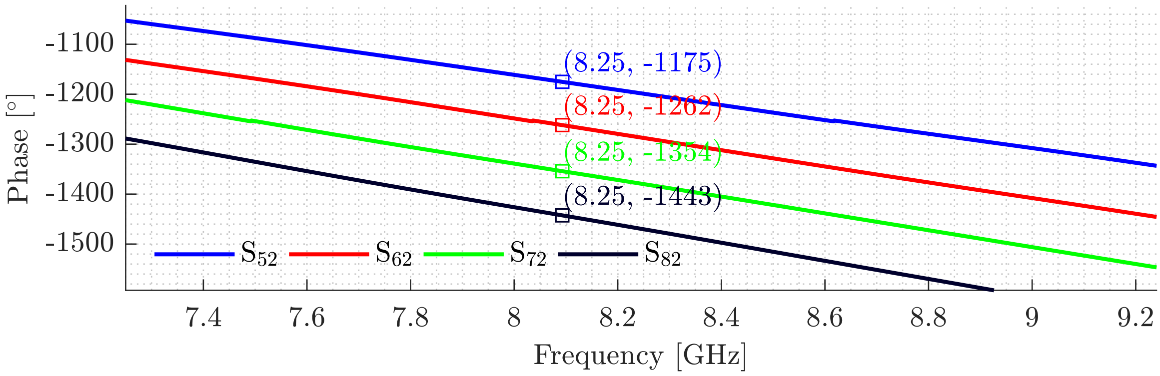

Figure 5.16: Simulated S-parameter phase for the X-band feeding network.

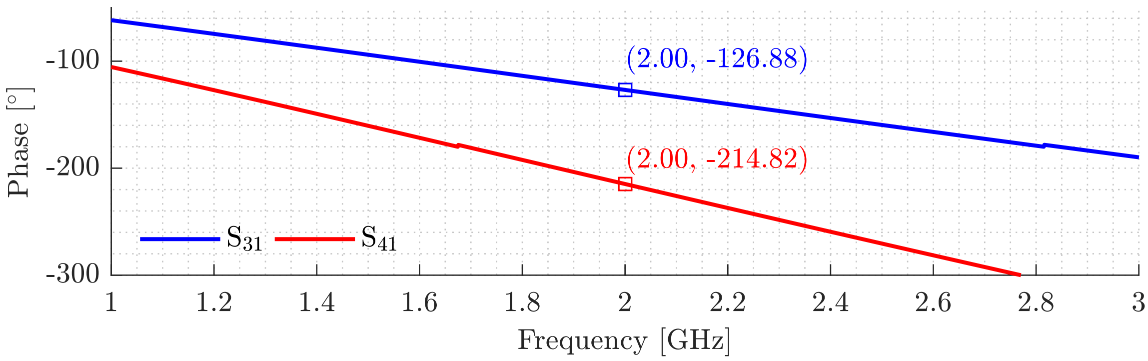

Figure 5.17: Simulated S-parameter phase for the S-band feeding network.

With the feeding network designed the next section presents the resulting antenna design and its simulated performance.

5.5 ASSEMBLED ANTENNA

Figure 5.18 shows two pictures of the final antenna design. Figure 5.18a shows a model with the antenna elements and guides highlighted. Figure 5.18b shows the model with the feeding network highlighted.

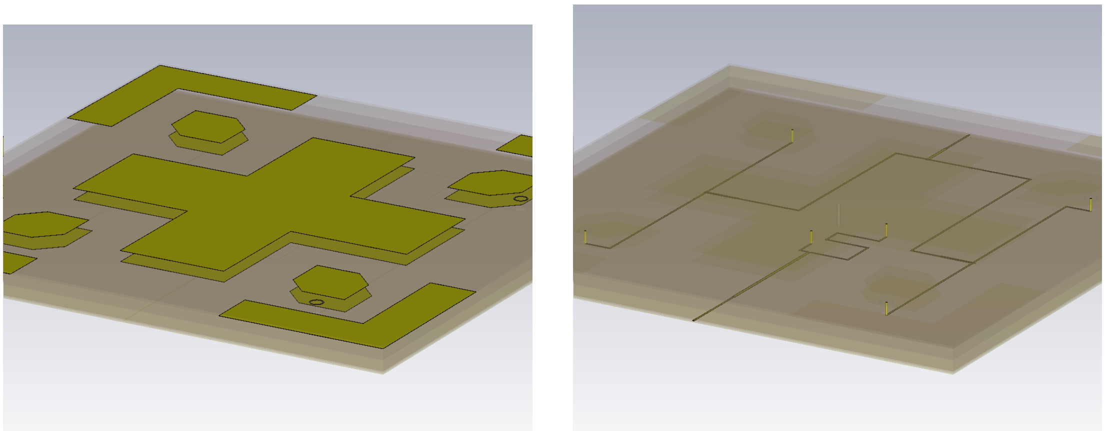

(a) The final antenna model with the antenna elements and guides highlighted.

(b) the final antenna with the feeding network highlighted.

Figure 5.18: Models of the final antenna structure.

Figure 5.19a shows the radiation pattern of the S-band antenna part of the final antenna, at 2 GHz. The realized RHCP gain is simulated to be 6.5 dB.

Figure 5.19b shows the radiation pattern of the X-band port of the final antenna design. The realized RHCP gain is observed to be 12.1 dB at 8.25 GHz. Thus the antenna has lost 0.7 dB in the feeding network compared to the simulation results shown in Figure 5.9b. This loss is in line with the loss found in the simulation shown in Figure 5.14.

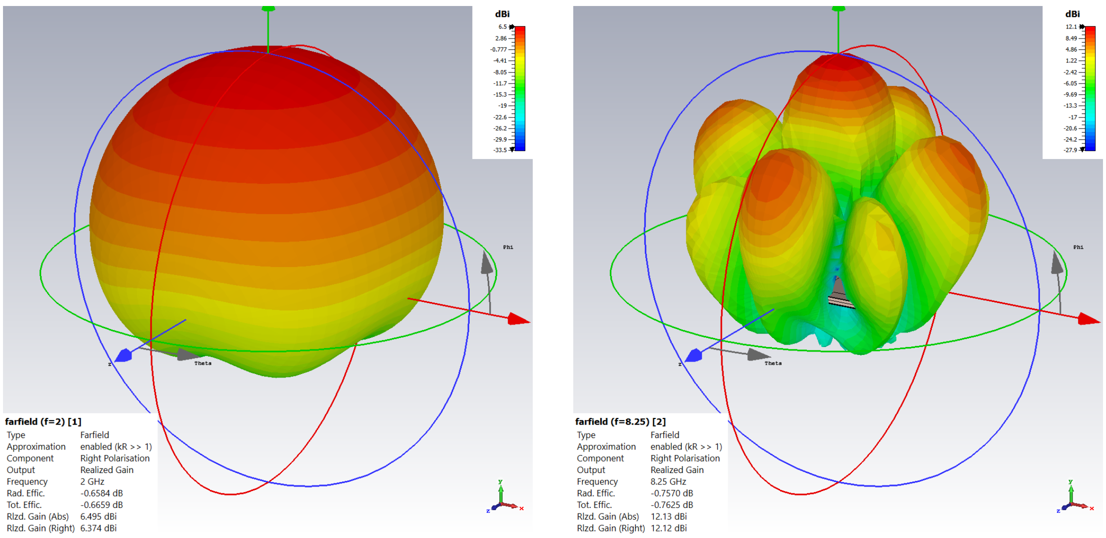

(a) Radiation pattern of port one at 2 GHz.

(b) Radiation pattern of port two at 8.25 GHz.

Figure 5.19: Simulated radiation patterns of the assembled antenna.

Figure 5.20 shows the $\phi = 90°$ and $\theta = 90°$ slices of the X-band radiation pattern seen in Figure 5.19b. The HPBW of the antenna is 20.0°. The side-lobe level is ≥ 4.09 dB at 43° from the center.

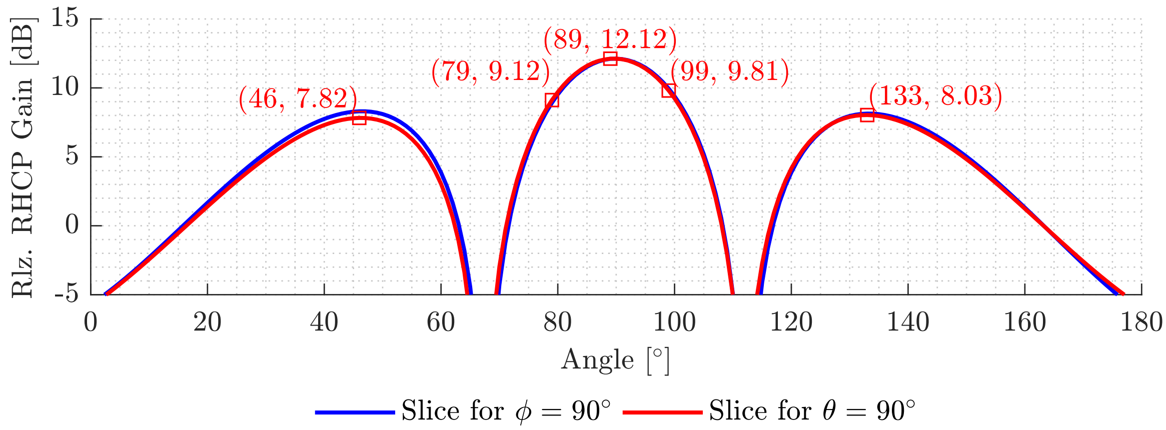

Figure 5.20: Radiation pattern slice of the X-band part of the antenna.

Figure 5.21 shows the $\phi = 90°$ and $\theta = 90°$ slices of the S-band radiation pattern seen in Figure 5.19a, The HPBW of the antenna is 42°.

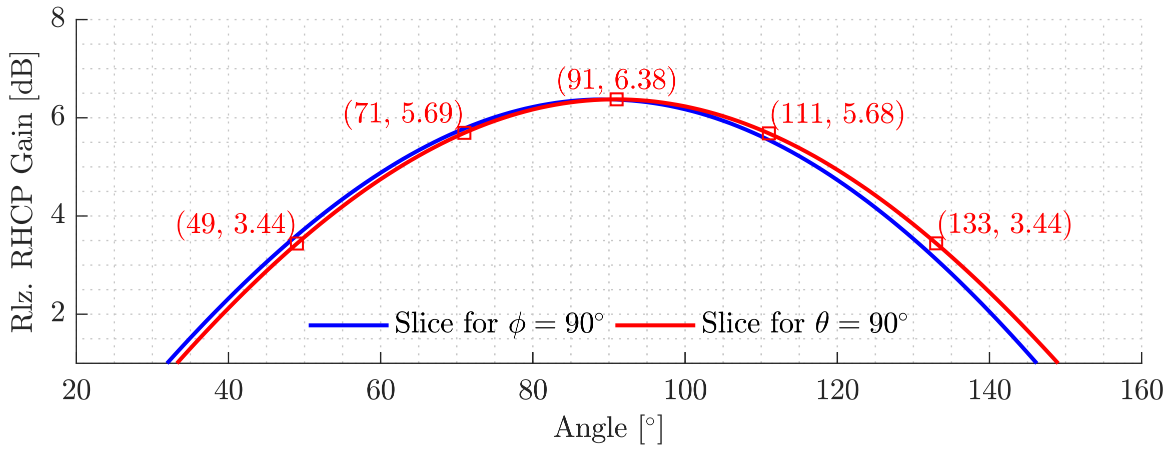

Figure 5.21: Radiation pattern slice of the S-band part of the antenna.

Figure 5.22 shows the realized RHCP gain of the S-band part of the antenna. The realized RHCP gain of the S-band part of the antenna is not above the requirement of 6 dB in the full frequency range from 1.97 to 2.03 GHz. The 6 dB requirement is only satisfied in the 1.975 to 2.015 GHz frequency range.

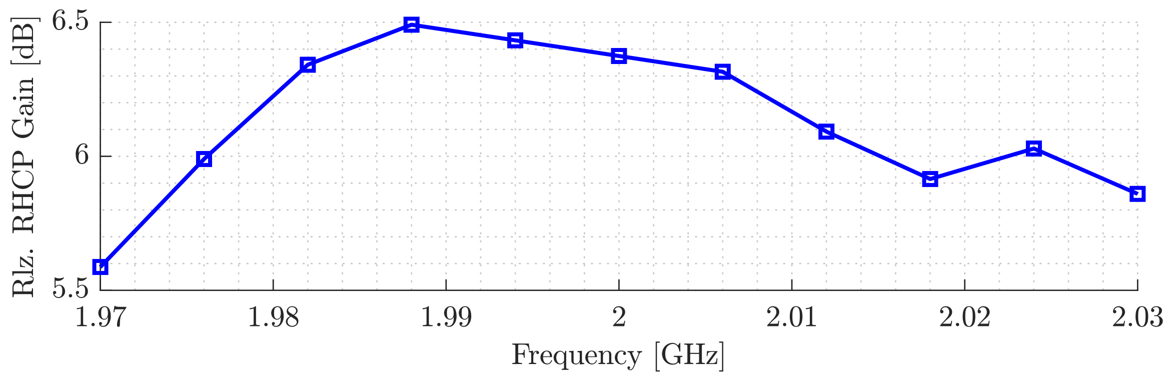

Figure 5.22: Simulated broadside realized RHCP gain of the S-band part of the antenna.

Figure 5.23 shows the S-parameters of the S-band antenna port. The antenna fulfils the impedance bandwidth requirement and has $> 10\,\mathrm{dB}$ return loss from 1.96 to 2.04 GHz. Additionally, the cross-coupling from the X-band antenna port is $\leq -27.5\,\mathrm{dB}$ at the operating frequency.

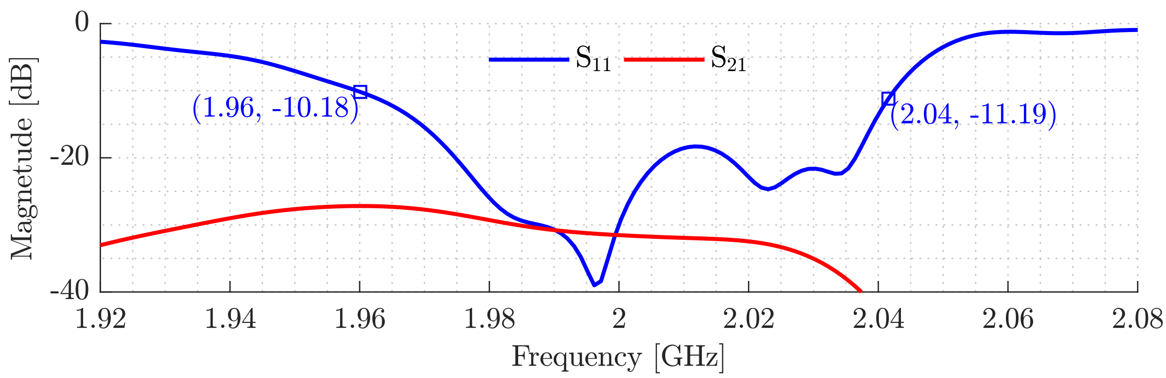

Figure 5.23: Simulated S-parameters for the S-band part of the antenna.

Figure 5.24 shows the simulated axial ratio of the S-band antenna port. The axial ratio of the antenna is $< -8\,\mathrm{dB}$ in the desired frequency band.

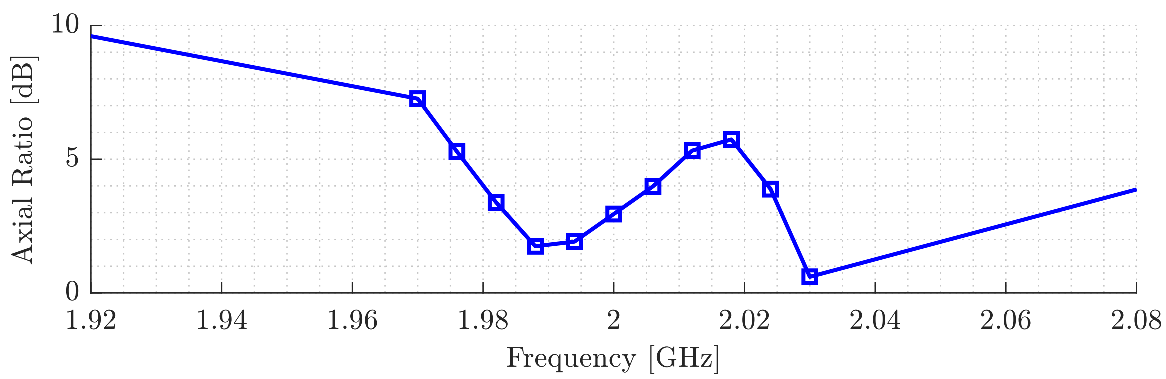

Figure 5.24: Axial ratio of port one (S-band).

Figure 5.25 shows the realized RHCP gain of the X-band part of the antenna. The antenna satisfies the 12 dB realized RHCP gain requirement in the full frequency range from 8.0 to 8.5 GHz.

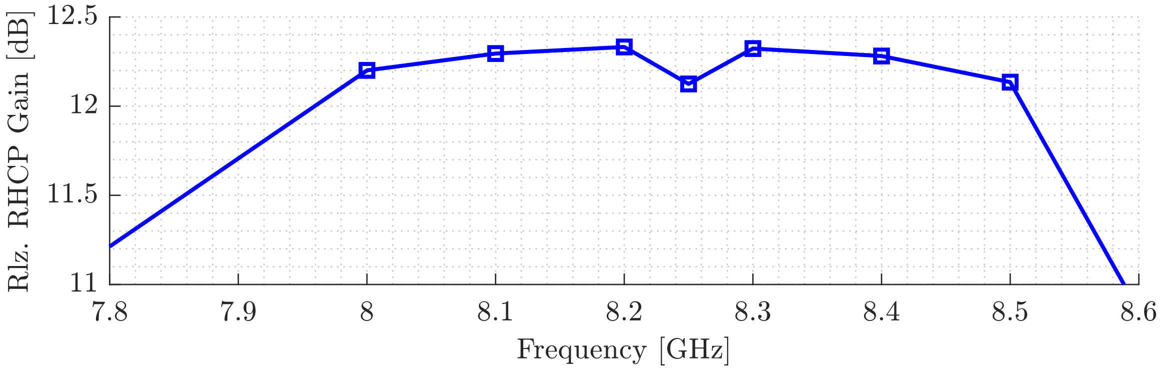

Figure 5.25: Simulated broadside realized RHCP gain of the X-band part of the antenna.

Figure 5.26 shows the S-parameters of the X-band antenna port. The simulation shows that the S_{22}-parameter of the antenna is well below the requirement of -10 dB. Additionally, the cross-coupling from the S-band antenna is observed to be below -33.5 dB.

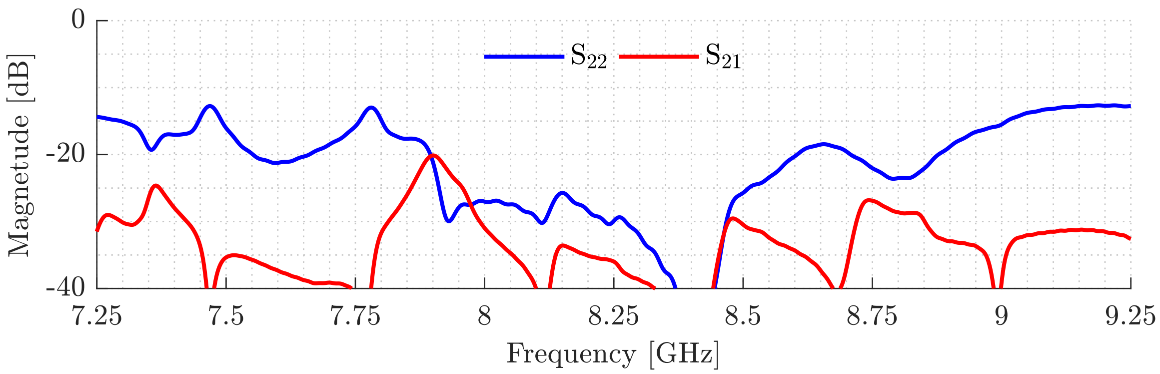

Figure 5.26: Simulated S-parameters for the X-band part of the antenna.

Figure 5.27 shows the simulated axial ratio of the X-band antenna port. The axial ratio is below 1.1 dB in the 8 to 8.5 GHz range.

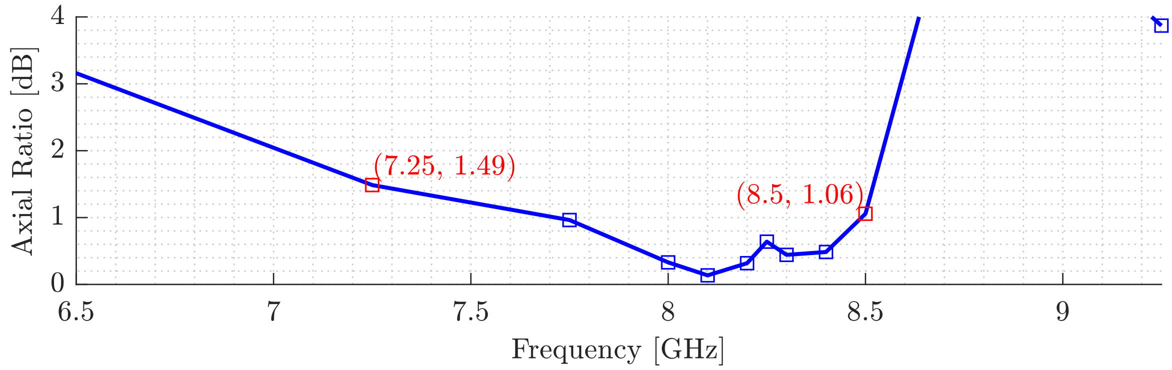

Figure 5.27: Simulated broadside axial ratio of port two (X-band).

Table 5.3 shows a comparison of the requirements specified in Table 4.1 and the simulated antenna performance. Most of the performance requirements are satisfied by the proposed antenna design. The still unsatisfied S-band gain bandwidth requirement will be discussed again after the manufacturing limitation have been investigated.

Table 5.3: Antenna requirement compared to the simulated performance of the Cross antenna design.

Performance metric	*Requirement*		*Simulated*	
Band	S-Band	X-Band	S-Band	X-Band
Bandwidth	1.97 to 2.03 GHz	8 to 8.5 GHz	1.97 to 2.03 GHz	8 to 8.5 GHz
Realized RHCP gain	$\geq$ 6 dB	$\geq$ 12 dB	$\geq$ 5.5 dB	$\geq$ 12.1 dB
HPBW	$\pm$ 20°	$\pm$ 10°	40°	20°
Cross-coupling	≤ -25 dB		≤ -27 dB	≤ -25 dB
Port reflection	≤ -10 dB		≤ -15 dB	≤ -25 dB
Impedance bandwidth	60 MHz	0.5 GHz	80 MHz	$\geq$ 2.5 GHz
Gain Bandwidth	60 MHz	0.50 GHz	39 MHz	0.55 GHz
Port input impedance	50 Ω		Yes	
Antenna dimensions	100 by 100 mm		83 by 83 mm	
Antenna height	$\leq$ 7 mm		$\leq$ 4 mm	
All metals $\geq$ 100 mm must be grounded			Yes	

With the performance of the Cross antenna design presented the Cross antenna design is concluded. The next chapter presents an alternative antenna design topology, the SepAp antenna design.

6 SOLUTION 2: SEPARATE APERTURE (SEPAP)

In Section 4.1 two different antenna solution proposals are presented. Chapter 5 presents the first design and its simulated performance. This chapter presents the second design and its simulated performance. This design is referred to as the separate aperture antenna structure or SepAp for short.

Figure 6.1 shows the proposed antenna structure and its feeding. As presented in Section 4.1 the antenna structure has four X-band antenna elements in the middle of the board and four S-band elements along the edge of the board.

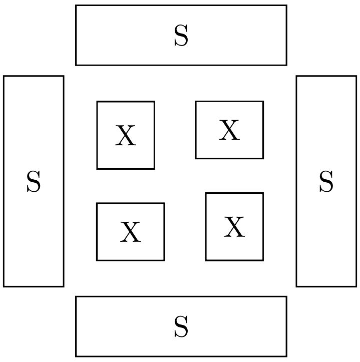

(a) Separate aperture structure. Four X-band antenna elements in the center and four S-band antenna elements along the edge of the board.

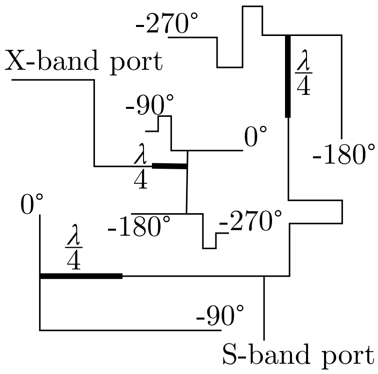

(b) Feed network layout. Impedance matching is done with a single quarter-wave transformer in the X-band feeding network and two in the S-band feeding network.

Figure 6.1: Drafts of antenna layout and feeding.

Figure 6.2 shows a cross-section of the assembled antenna. On top there is a thin layer of substrate, h_1, to serve as a shield and increase the effective permittivity of the S-band antenna elements. Below is a thicker layer of substrate h_2 supporting the S-band antenna elements. The lower antenna substrate h_3 supports the X-band antenna elements.

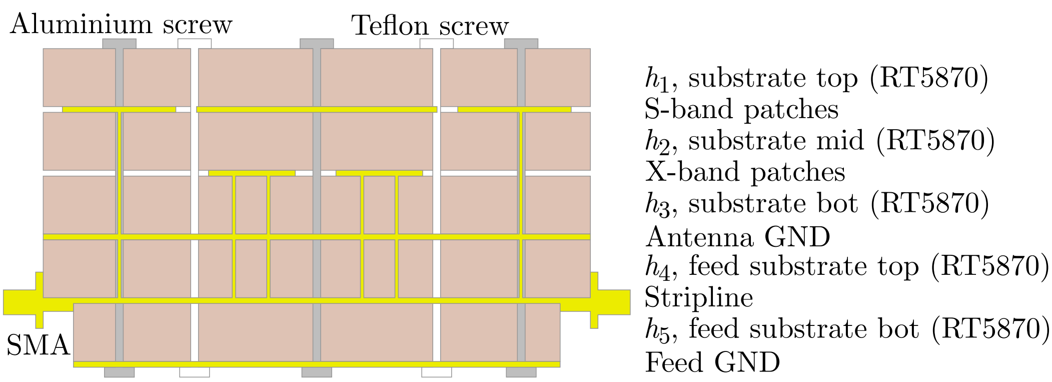

Figure 6.2: Illustration of the chosen antenna stack-up. Yellow is copper and brown is substrate. Vertical yellow lines are VIAs. Gray screws are made of aluminium and white screws are made of Teflon. Figure not to scale.

With this stack-up the separation between the S-band antenna elements and the ground plane can be increased to achieve the desired bandwidth, without making the separation between the X-band antenna elements and the ground plane too high. It is also possible to place additional S-band patches on the X-band patch layer and vice versa to alter the response by introducing additional coupled resonators.

As stated in Chapter 7, due to the choice of Rogers RT5870 laminate as substrate, where no matching pre-preg is available, the patch is designed for manual assembly with screws to hold the structure together and soldered wires as VIAs. Chapter 7 also covers the choice of feeding the antenna through SubMiniature version A (SMA) connectors and the interface between the antenna and the connector. Figure 6.3 shows a top and bottom view of the assembled antenna. In the top and bottom layer, there are visible holes to allow for soldering VIA wires between the feeding network and the radiating elements. There are similar holes in the middle antenna substrate h_2 to allow soldering between the feeding network and the X-band antenna elements.

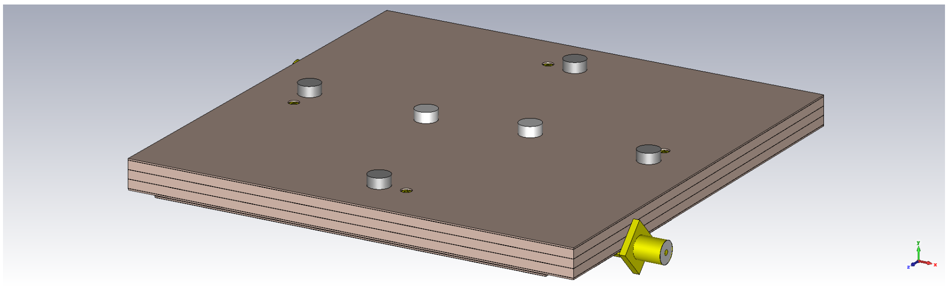

(a) Picture of the top of a 3D model of the SepAp antenna made in CST.

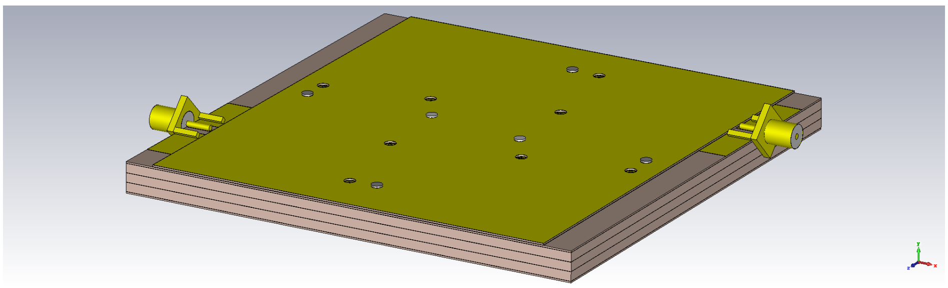

(b) Picture of the bottom of a 3D model of the SepAp antenna made in CST.

Figure 6.3: Pictures of CST model of assembled antenna. Yellow is copper, white is teflon, gray is aluminium, and brown is Rogers RT5870. There are visible holes in the top and bottom of the antenna to allow soldering of VIA wires.

6.1 S-BAND ANTENNA ELEMENTS

The initial challenge of the S-band design is to fulfil the bandwidth requirement. The bandwidth can be increased by for example:

- Switching to a substrate with lower relative permittivity.
- Increasing substrate height.
- Cutting slots in the antenna elements to introduce additional resonances.
- Stacking antenna elements to introduce additional resonances.
- Designing feeding as a coupled resonator bandpass filter.

As Section 2.7.3 and Appendix B show that increasing the substrate height up to a point provides an easy way to improve impedance bandwidth and realized gain, a tall substrate is chosen. The requirements list a maximum height of 7 mm, so the substrate heights are set to $h_2 = 3.150$ mm and $h_3 = 1.575$ mm. Initial dimensions are calculated using Section 2.7 and fitted through simulations. Dimensions are shown in Table 6.1 and variable explanation is shown in Figure 6.4.

Table 6.1: Dimensions of the substrates and S-band antenna elements.

Name	*Variable*	*Fitted value*	*Calculated value*
Patch length	L_S	48.45 mm	46.41 mm
Patch width	W_S	12 mm	-
Probe offset	p_0	5 mm	2.29 to 3.99 mm
Probe diameter	D_{probe}	0.8 mm	-
Ground cutout diameter	D_{GND}	2.86 mm	2.86 mm
Edge distance	D_e	3.5 mm	-
S- to X-Patch separation	D_p	11 mm	-
Bottom substrate height	h_3	1.575 mm	-
Middle substrate height	h_2	3.150 mm	-
Top substrate height	h_1	0.254 mm	-
Board size	-	82 mm	-

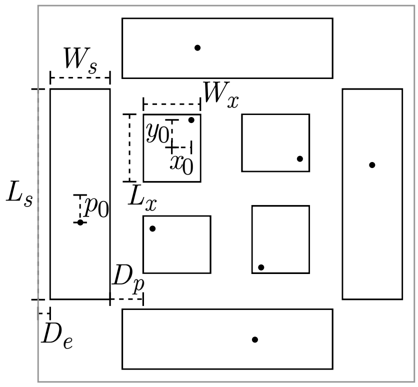

Figure 6.4: Figure showing variable names and their corresponding dimensions. The gray box is the board outline. Black dots are feeding probes.

Figures 6.5 and 6.6 show the CST model used for antenna element simulations.

Figure 6.7 shows the simulated impedance bandwidth and broadside realized linear gain with total substrate heights $h_t = h_2 + h_3 = 4.725$ mm and $h_t = 3.150$ mm. The substrate height $h_2 = 3.150$ mm is chosen since it shows sufficient performance. The gain margin is 1.5 dB at the edges of the band. The impedance bandwidth is nearly fulfilled, with the return loss falling slightly below the minimum 10 dB at the higher end of the band. The feeding network is however expected to introduce losses to the system, which should move the collective return loss above the 10 dB threshold. The performance is therefore deemed sufficient.

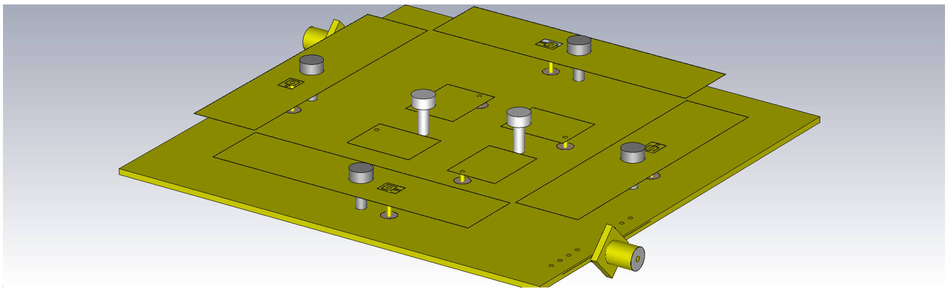

Figure 6.5: Picture of the top of a 3D model of the antenna made in CST used for antenna element simulations. The visible cutouts in the S-band antenna elements are detailed in Section 6.3 and simulated to not affect the performance at S-band. Substrates are hidden and the feeding probes are terminated in coaxial waveguide ports on the bottom of the model.

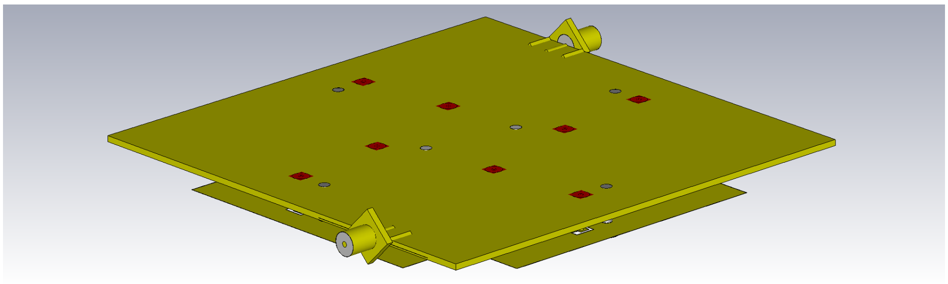

Figure 6.6: Picture of the bottom of a 3D model of the antenna made in CST used for antenna element simulations. Substrates are hidden and the feeding probes are terminated in coaxial waveguide ports, illustrated as red squares.

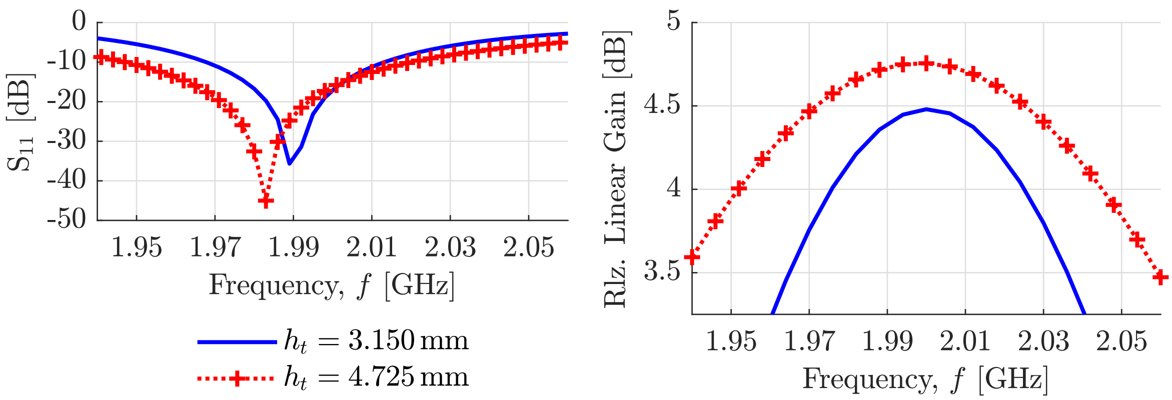

Figure 6.7: Simulated broadside realized linear gain and S_{11}-parameter for a single S-band antenna element with a total substrate height of $h_t = h_2 + h_3 = 4.725$ mm and $h_t = 3.150$ mm.

With the design of the S-band antenna elements finished, the X-band elements are now dimensioned.

6.2 X-BAND ANTENNA ELEMENTS

To achieve a RHCP gain of 12 dB, each X-band antenna element must have a realized RHCP gain of ≥ 6 dB. Circular polarization can be achieved by several different methods, some of which detailed in Section 2.9. Appendix A investigates the performance of the different designs and finds that they have very similar performance. The corner feed design is chosen due to its simplicity and absence of diagonal edges, easing time-domain simulations.

The model shown in Figures 6.5 and 6.6 is again used for simulations. The X-band antenna elements are fitted through parameter sweeping, so to reduce the scope of the sweeping, two parameters are defined by Equations (6.1) and (6.2)[1].

$$\text{Size} = \frac{L_x + W_x}{2} \qquad [\text{m}] \quad (6.1)$$

$$\text{Ratio} = \frac{L_x}{W_x} \qquad [\text{m}] \quad (6.2)$$

Where:

L_x	=	X-band patch length	[m]
W_x	=	X-band patch width	[m]

The parameter "Size" is then the electrical length of a patch antenna tuned to the center frequency between the frequencies of the two orthogonally excited modes. Altering "Size" should tune the X-band patch to a different frequency.

The parameter "Ratio" sets the frequency ratio between the two orthogonally excited modes. "Ratio" is used to alter the axial ratio. A higher "Ratio" is expected to provide a wider axial ratio bandwidth at the cost of impedance matching.

A parameter sweep where the parameters "Size", "Ratio", and feeding probe position is changed has been conducted to tune the X-band antenna elements. The subset of simulation runs that provides the highest broadside realized RHCP gain is shown in Figure 6.8 (next page).

Figure 6.8 shows that the broadside realized RHCP gain is highest at around 8.45 GHz for all the shown simulation runs. Contrary to the expected behaviour, increasing the parameter "Size" to 10.15 mm does not move the maximum realized broadside gain to a lower frequency. The parameters corresponding to the simulation run with the highest realized broadside gain are chosen, even though this run provides the worst axial ratio of the shown results.

When the X-band antenna elements are combined sequentially rotated, any uneven polarization is ideally equalized and the combined gain is equal the single element gain plus 6 dB. If the feeding network does not excite antennas equally, the axial ratio will suffer dependent on the single element axial ratio.

A probe fed square 8.25 GHz patch antenna on 1.575 mm RT5870 substrate can be simulated to have a bandwidth $BW \approx 0.5\,\text{GHz} \implies FBW \approx \frac{0.5}{8.25} \approx 0.06$. Such an X-band patch, therefore, has a Q-factor of $Q_p = \frac{1}{FBW\sqrt{2}} = 11.667$. For the nearly square patch design, the literature gives approximate formulas for the frequencies of the two orthogonal modes as Equations (6.3) and (6.4) [8, p. 831].

[1] Ideally the parameter Size should be given through a more complex expression as the relative strength of the two modes, and by extension the center frequency of the circularly polarized patch, depends on the proportional frequency deviation and the Q-factors of the two modes. However as $L_x \approx W_x$, the center frequency is approximately equal the average.

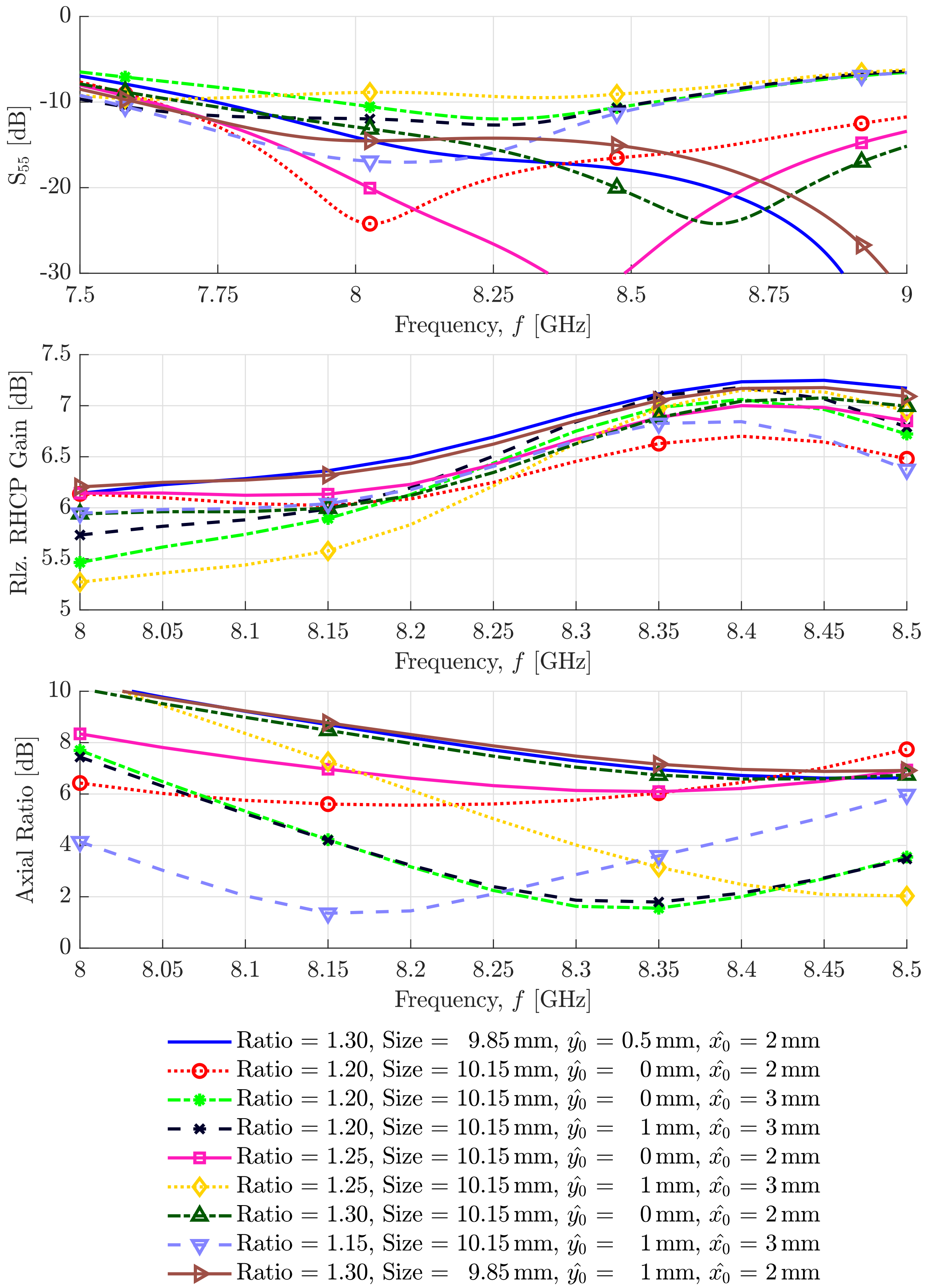

Figure 6.8: Simulated reflection coefficient, broadside realized RHCP gain, and broadside axial ratio for single X-band antenna element for different parameters. "Ratio" is the patch length to patch width ratio, Ratio $= \frac{L}{W}$. "Size" alters the center frequency, Size $= \frac{L+W}{2}$. $\hat{x_0}$ and $\hat{y_0}$ are feed point offsets from the patch edge, along the width and length of the patch respectively ($y_0 = \frac{L}{2} - \hat{y_0} - 0.3$ mm where the 0.3 mm is subtracted to account for the diameter of feeding probe and production tolerances).

$$f_1 = \frac{f_X}{\sqrt{1+Q_p^{-1}}} = 7.92\,\text{GHz} \tag{6.3}$$

$$f_2 = f_X\sqrt{1+Q_p^{-1}} = 8.60\,\text{GHz} \tag{6.4}$$

Where:

f_X	=	X-band center frequency	[Hz]
f_1	=	lower resonance frequency	[Hz]
f_2	=	higher resonance frequency	[Hz]
Q_p	=	quality factor of the patch	[Hz]

The corresponding resonant lengths are calculated recursively based on Section 2.7, using the resonant length of the other orthogonal mode as the width of the patch until convergence.

Table 6.2 shows the calculated and final values after fitting.

Table 6.2: Dimensions of the X-band antenna elements.

Name	*Variable*	*Fitted value*	*Calculated value*
Patch length	L_X	11.13 mm	11.60 mm
Patch width	W_X	8.57 mm	10.52 mm
Probe offset L	y_0	4.76 mm	-
Probe offset W	x_0	1.98 mm	-

6.3 S-BAND AND X-BAND ISOLATION

With the chosen antenna layout and the dimensioned S- and X-band antenna elements, there is some cross-coupling between the S- and X-band antenna elements in the X-band 8 to 8.5 GHz frequency range, as shown in Figure 6.10 by the dashed lines. Between the simulated S-band antenna element and the closest X-band antenna element, the isolation is approximately in the range of −28 to −24 dB. The isolation can be improved by cutting a small pad in the S-band antenna elements around the feeding point, inspired by [24, 25]. This pad also serves as a soldering pad during assembly. An illustration of the S-band antenna element with filtering pad cutout is shown in Figure 6.9 and fitted values are given in Table 6.3.

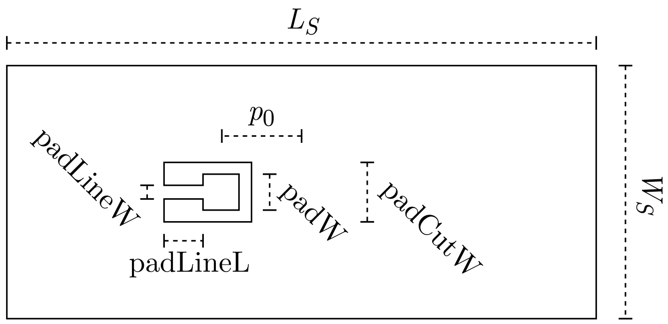

Figure 6.9: Drawing of S-band patch with filtering pad cutout as seen from above. The filtering pad consists of a square pad with a narrow line connecting the pad to the rest of the patch.

Table 6.3: Dimensions of the S-band patches with filtering pad cutout, as illustrated in Figure 6.9

Name	*Variable*	*Fitted value*
Patch length	L_S	48.45 mm
Patch width	W_S	12 mm
Probe offset	p_0	5 mm
Pad width	padW	1.8 mm
Pad cut width	padCutW	2.8 mm
Pad line length	padLineL	1.3 mm
Pad line width	padLineW	0.4 mm

Simulations show that the impedance and radiation performance at the S-band 1.97 to 2.03 GHz frequency range is unaltered, so results are only shown for the X-band 8 to 8.5 GHz frequency range. Simulated S-parameters between S-band antenna element (port one) and X-band antenna elements (port five to eight) are shown in Figure 6.10.

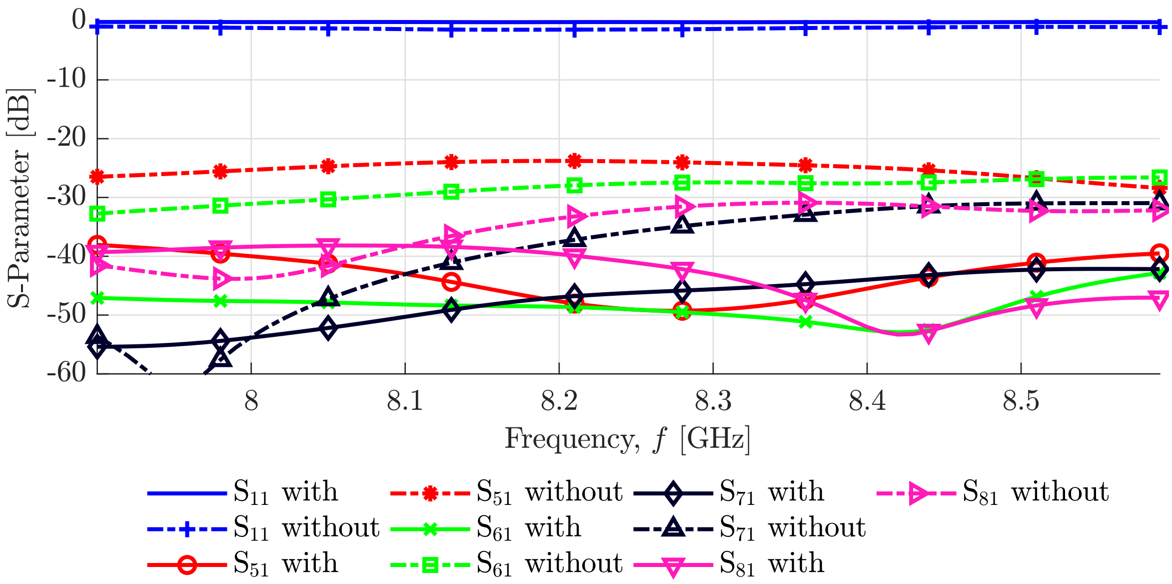

Figure 6.10: Simulated S-parameters with and without S-band patch cutout. Port one is assigned to an S-band antenna element. Port five to eight are assigned to the four X-band antenna elements

Assuming the S- and X-band feeding networks are both comprised of three ideal power splitters (input to antenna S-parameter is -6 dB) and that the phase shift is linear with frequency (constant time shift), the S- to X-band port is given by Equation (6.5).

$$\mathrm{S_{XS}} = \frac{1}{4}\left(\sum_{\mathrm{n=1}}^{4} \mathrm{e}^{-i\frac{\pi\cdot(n-1)}{2}\cdot\frac{f}{f_S}}\left(\sum_{\mathrm{m=5}}^{8} \mathrm{S_{mn}}\mathrm{e}^{-i\frac{\pi\cdot(m-4)}{2}\cdot\frac{f}{f_X}}\right)\right) \quad [1] \quad (6.5)$$

Where:

f_S	=	S-band center frequency	[Hz]
f_X	=	X-band center frequency	[Hz]
f	=	frequency	[Hz]

Figure 6.11 shows the S- and X-band isolation with idealized feeding networks. The filtering pad cutout improves the isolation by more than 10 dB in the X-band 8 to 8.5 GHz frequency range, bringing the isolation below −50 dB in the full band. Figure 6.11 also shows that the performance is unaltered in the S-band.

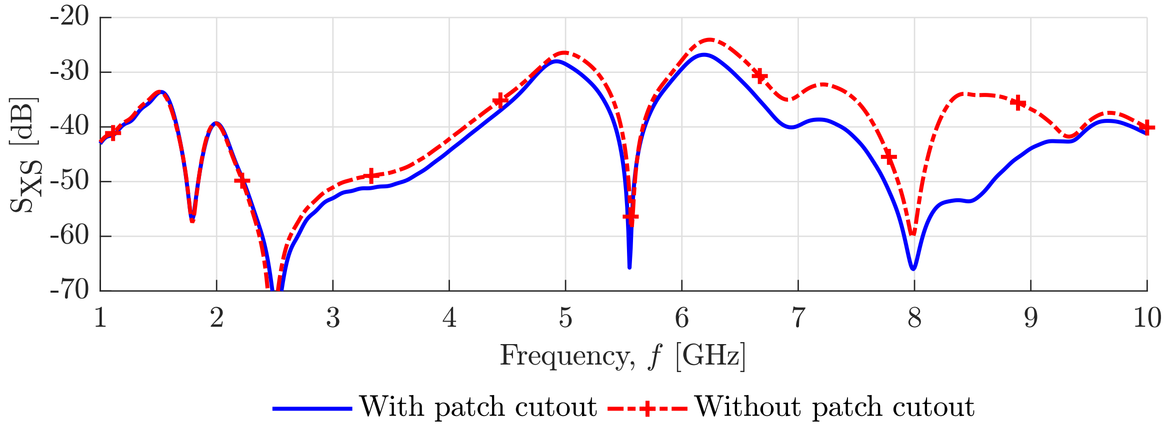

Figure 6.11: Approximated isolation based on antenna element simulation. A more than 10 dB improvement is seen in the 8 to 9 GHz range. Port one and two are respectively the S-band and X-band ports of an idealised final antenna assembly.

With simulations showing sufficient impedance, gain, and isolation the feeding network is designed and simulated.

6.4 FEEDING NETWORK

The S- and X-band feeding networks consist of three T-junction power dividers each, splitting the two inputs into eight outputs. Figures 6.12 and 6.13 show transmission-line models of two different feeding network design possibilities.

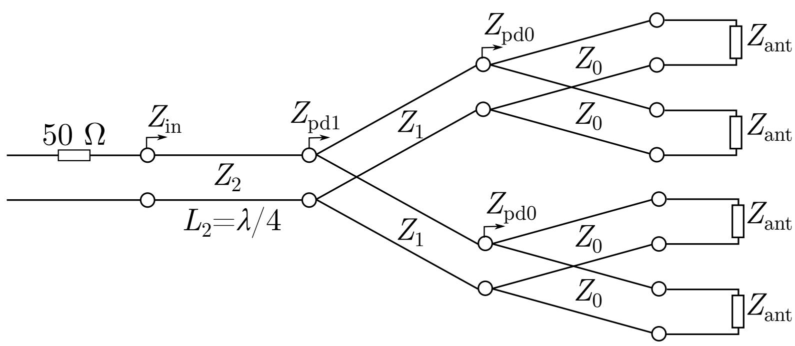

Figure 6.12: Transmission line model of feeding network design 1. To match impedances, design 1 has a single quarter-wave transformer at the input.

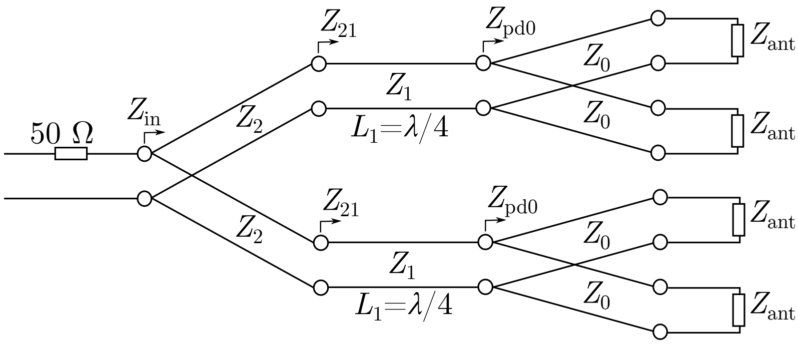

Figure 6.13: Transmission line model of feeding network design 2. To match impedances, design 2 has two quarter-wave transformers in the middle of the feeding network.

The following two paragraphs calculates the impedances. Afterwards a 3D-model of the feeding network is created and simulated.

Design 1 It is assumed that $Z_0 = Z_{\text{ant}} = 50\,\Omega$. Z_{pd0} is therefore given by Equation (6.6).

$$Z_{\text{pd0}} = Z_0 \parallel Z_0 = 25\,\Omega \tag{6.6}$$

Where:

Z_{pd0}	=	input impedance of power divider 0	[Ω]
Z_0	=	characteristic impedance of stripline 0	[Ω]

The impedances are matched: $Z_1 = Z_{\text{pd0}} = 25\,\Omega$. The input impedance of the power divider 1 is then given by Equation (6.7).

$$Z_{\text{pd1}} = Z_1 \parallel Z_1 = 12.5\,\Omega \tag{6.7}$$

Where:

Z_{pd1}	=	input impedance of first power divider	[Ω]
Z_1	=	characteristic impedance of stripline 1	[Ω]

To match the impedance Z_{pd1} to the source resistance $R_s = 50\,\Omega$, a quarter-wave transformer with impedance Z_2 is used. The impedance of the quarter-wave transformer is calculated by using Equation (2.73) as Equation (6.8).

$$Z_2 = \sqrt{R_s \cdot Z_{\text{pd1}}} = 25\,\Omega \tag{6.8}$$

Design 2 As in design 1, it is assumed that $Z_0 = Z_{\text{ant}} = 50\,\Omega$. To match source and antenna impedances, impedances Z_0 and Z_2 are given by Equations (6.9) and (6.10).

$$Z_0 = Z_{\text{in}} = 50\,\Omega \tag{6.9}$$
$$Z_{\text{in}} = Z_2 \parallel Z_2 \implies Z_2 = Z_{\text{in}} \cdot 2 = 100\,\Omega \tag{6.10}$$

Where:

Z_2	=	characteristic impedance stripline 2	[Ω]

The impedance of the quarter-wave transformer Z_1 is chosen to match impedances Z_2 and Z_{pd0} by the same method as in design 1, as shown in Equation (6.11).

$$Z_1 = \sqrt{Z_2 \cdot \left(\frac{Z_0}{2}\right)} = 50\,\Omega \tag{6.11}$$

Where:

Z_1	=	characteristic impedance of the quarter-wave transformer	[Ω]

3D-modelling and simulation The feeding network substrate heights h_4 and h_5 are set to the second lowest standard thickness of 0.254 mm. With these heights the total height of the antenna is $H_{\mathrm{tot}} = 3 \cdot 0.254\,\mathrm{mm} + 3 \cdot 1.575\,\mathrm{mm} = 5.487\,\mathrm{mm}$ excluding trace thickness, leaving approximately $H_{\mathrm{mount}} = 7\,\mathrm{mm} - (5.487\,\mathrm{mm} + 0.21\,\mathrm{mm}) \approx 1.3\,\mathrm{mm}$ for the mounting system assuming a trace thickness of 35 µm.

Table 6.4 lists stripline dimensions used in the feeding network designs. Line widths are calculated using Equation (2.49).

Table 6.4: Dimensions of the X-band antenna elements. The *Init. sim.* column contains the dimensions used for the non-isolated simulation of the model in Figure 6.14c, these values has not been fitted. The column *Fit* contains the fitted values for the isolated feed model in Figure 6.14b.

Name	*Variable*	*Init. sim.*	*Fit*	*Calculated*
Line width 25 Ω	-	1.00 mm	1.00 mm	1.03 mm
Line width 50 Ω	-	0.35 mm	0.35 mm	0.40 mm
Line width 100 Ω	-	-	-	0.10 mm
S-band quarter wavelength	-	25.55 mm	25.55 mm	24.55 mm
X-band quarter wavelength	-	6.43 mm	5.86 mm	5.95 mm
Feed substrate top	h_4	0.254 mm	0.254 mm	-
Feed substrate bot	h_5	0.254 mm	0.254 mm	-

Due to production tolerances, the minimum clearance and line width is 0.1 mm. The narrowest line of design 2 is 0.1 mm whereas the narrowest line of design 1 is 0.4 mm. Minor deviations in production will provide a smaller relative error for design 1, making it more robust to production tolerances. Design 1 is chosen due to its bigger line width. Figure 6.14 shows the 3D model used to simulate the feeding network with and without isolating VIAs.

The parameters are fitted to optimize the broadside RHCP array gain given by Equation (6.12) for the S-band and Equation (6.12) for the X-band.

$$\mathrm{AG}_{\mathrm{RHCP,S}} = 20 \cdot \log_{10} \left| \sum_{\mathrm{n=3}}^{6} \left(\mathrm{S}_{\mathrm{n1}} \cdot \mathrm{e}^{i\frac{(n-3)\pi}{2}} \right) \right| \quad [\mathrm{dB}] \tag{6.12}$$

$$\mathrm{AG}_{\mathrm{RHCP,X}} = 20 \cdot \log_{10} \left| \sum_{\mathrm{n=7}}^{10} \left(\mathrm{S}_{\mathrm{n2}} \cdot \mathrm{e}^{i\frac{(n-7)\pi}{2}} \right) \right| \quad [\mathrm{dB}] \tag{6.13}$$

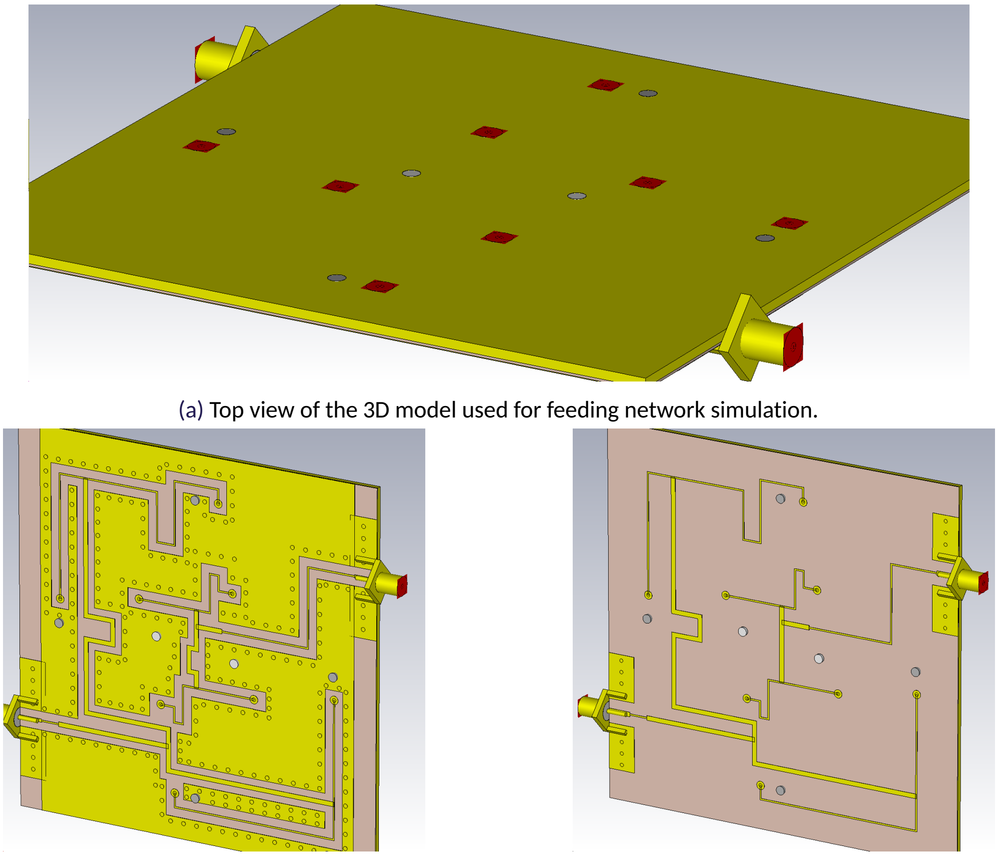

(a) Top view of the 3D model used for feeding network simulation.

(b) Bottom view of the 3D model used for feeding network simulations with isolating VIAs

(c) Bottom view of the 3D model used for feeding network simulations without isolating VIAs

Figure 6.14: Pictures of 3D CST model of feeding network. Ports one and two are the S-band and X-band SMA waveguide ports. Ports three to six are S-band antenna element ports, ports seven to ten are X-band antenna element ports. The antenna feeding probes are terminated in coaxial waveguide ports illustrated as red squares in Figure 6.14a. Bottom copper layer Feed GND and substrate h_5 are hidden to show feeding network in Figures 6.14b and 6.14c

Figure 6.15 shows the simulated reflection coefficient and cross-coupling between the S- and X-band SMA ports. The simulation shows that the cross-coupling in the feeding network is significantly reduced by the isolating VIAs, and the reflection coefficient has fewer dips and an overall smoother frequency response. The isolated design is chosen for its lower cross-coupling.

Figures 6.16 and 6.17 show the performance of the fitted feeding network in the S- and X-band respectively.

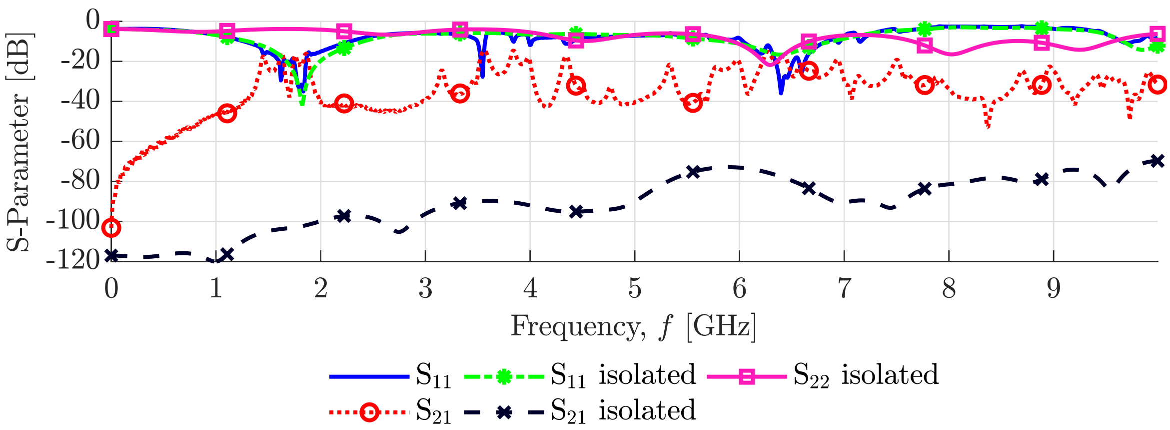

Figure 6.15: Simulated S-parameters with and without shielding around stripline. Port one is assigned the S-band port and port two is assigned the X-band input port. Non-isolated S_{22} has not been simulated to due to the design being discarded because of the high cross-coupling visible from the initial simulation.

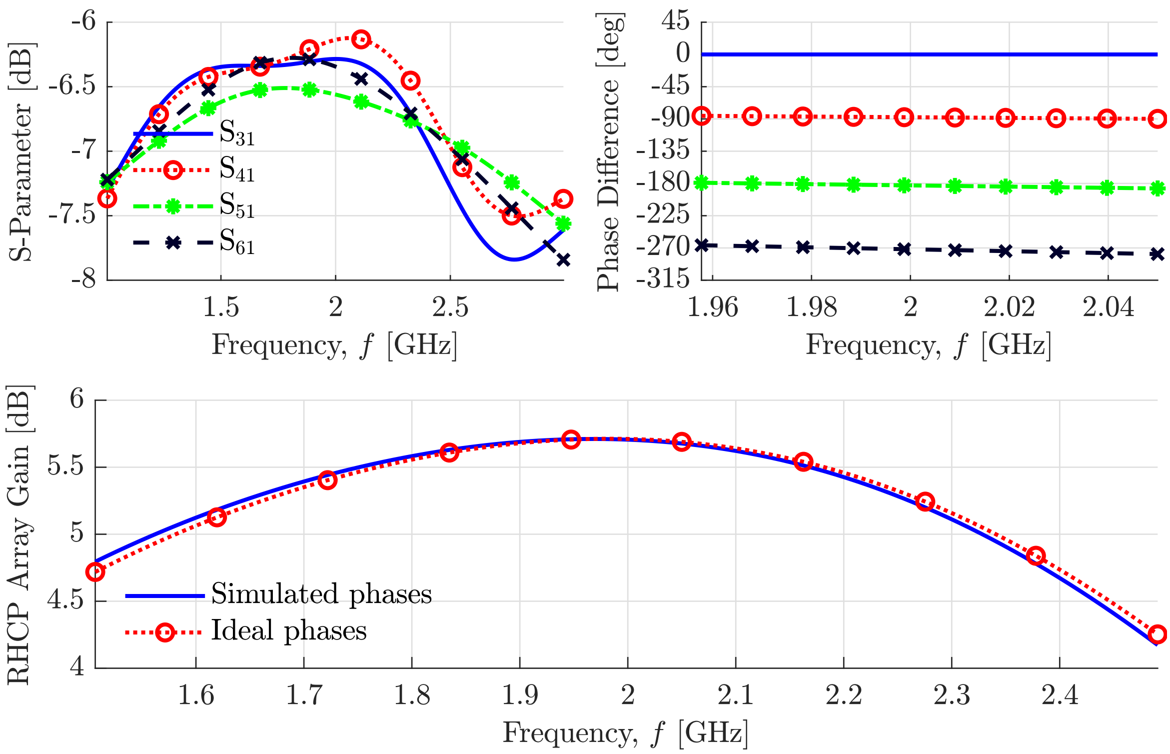

Figure 6.16: Simulated S-parameters for the S-band feeding network and resultant broadside RHCP array gain. Port one is the S-band port. Ports three to six are coaxial ports modelling termination in the four S-band antenna elements.

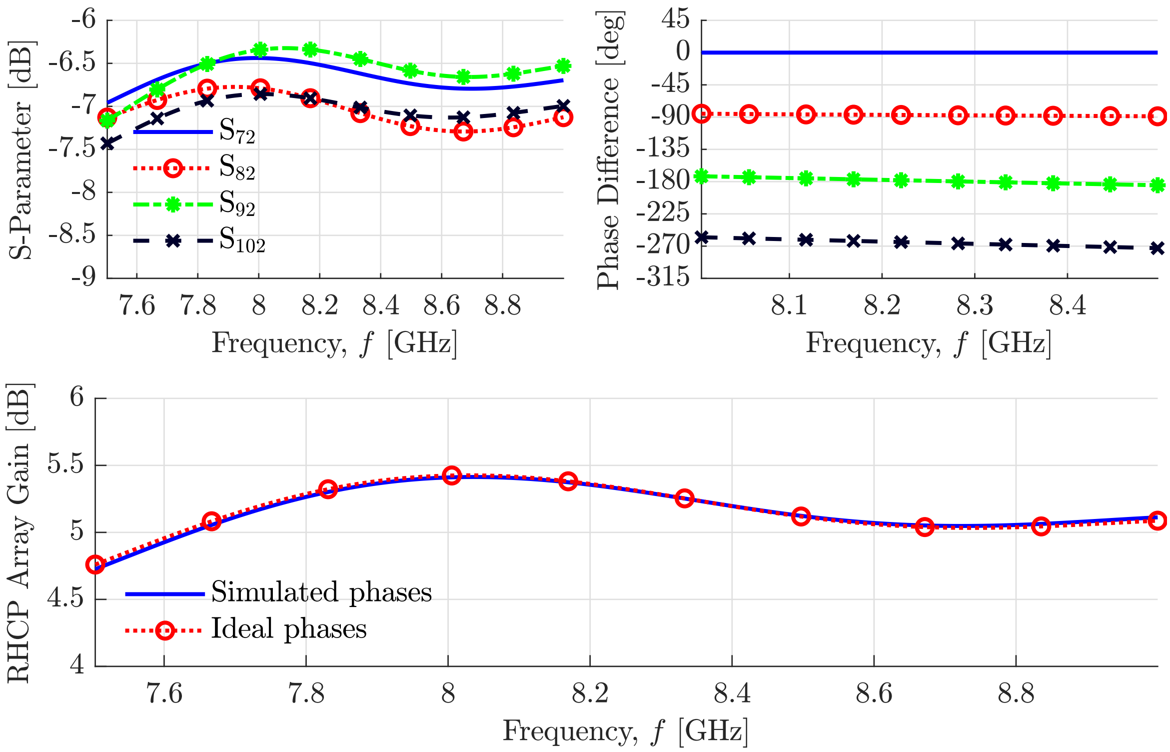

Figure 6.17: Simulated S-parameters for the X-band feeding network and resultant broadside RHCP array gain. Port two is the X-band port. Ports seven to ten are coaxial ports modelling termination in the four X-band antenna elements.

6.5 ASSEMBLED ANTENNA

The feeding network and antenna elements are assembled into a single model and simulated. Figure 6.18 shows the simulated S-parameters and Figure 6.19 shows the broadside realized RHCP gain and broadside axial ratio in the S- and X-band. Figure 6.20 shows the radiation pattern at the two bands' center frequencies.

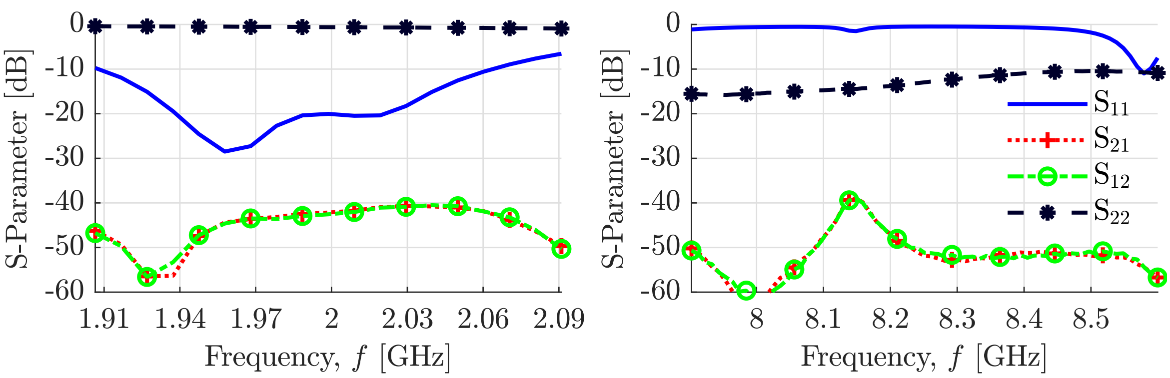

Figure 6.18: Simulated S-parameters of the assembled antenna. Port one is the S-band port. Port two is the X-band port.

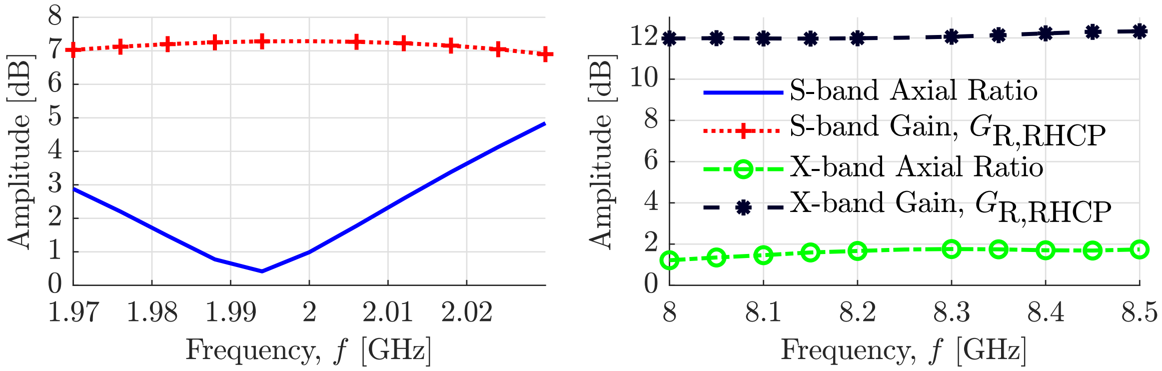

Figure 6.19: Simulated broadside realized RHCP gain and broadside axial ratio of the assembled antenna.

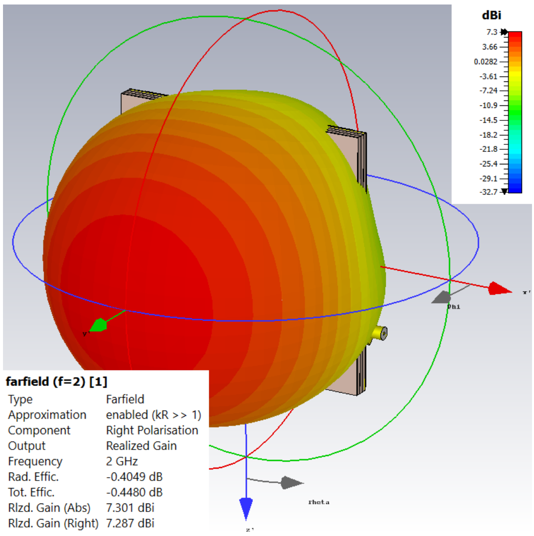

(a) Simulated S-band center frequency realized RHCP gain pattern.

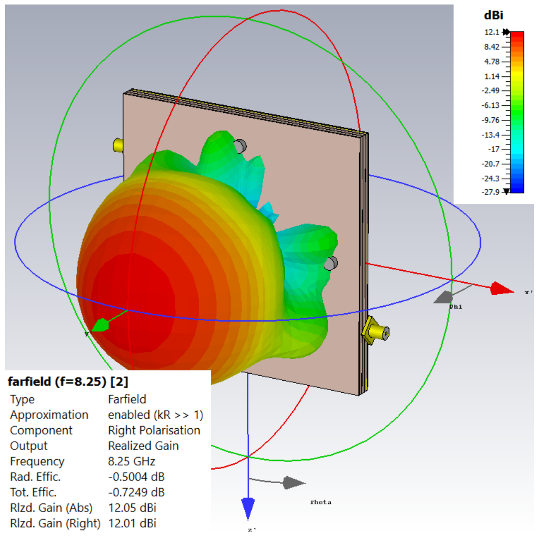

(b) Simulated X-band center frequency realized RHCP gain pattern.

Figure 6.20: Simulated radiation patterns.

The simulations show sufficient realized RHCP gain in both bands, but the axial ratio goes above the specified maximum 3 dB limit within the S-band. Figure 6.21 shows simulated RHCP realized gain pattern slices at the center frequencies and the worst case in-band frequency slice. The worst case is chosen as the slice where the realized RHCP gain falls 3 dB below the required broadside gain, at the lowest angle relative to the broadside direction to either side. This is done to find a beamwidth that guarantees a gain above the requirement for all in-band frequencies simultaneously, since the radiation pattern does not have the same shape for all frequencies.

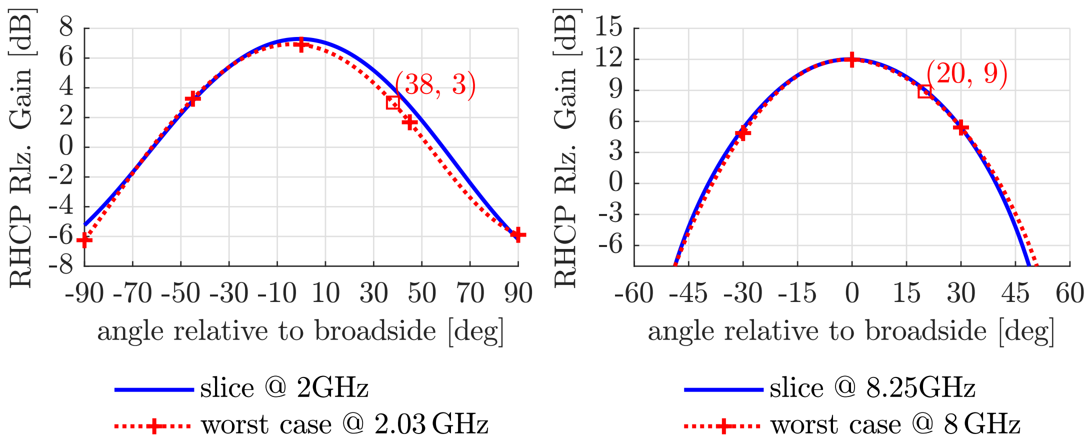

Figure 6.21: Simulated center frequency realized RHCP gain pattern slice and worst case in-band slice.

The X-band fulfils all the requirements within the specified band. The axial ratio is flat across the band due to the sequential rotation of the antenna elements and the fact that all elements are individually circularly polarized. Table 6.5 shows an overview of the requirements and simulated performance.

Table 6.5: Final simulated performance of the separate aperture dual-band antenna compared to the specified requirements.

Performance metric	*Requirement*		*Simulated*	
Band	S-Band	X-Band	S-Band	X-Band
Bandwidth	1.97 to 2.03 GHz	8 to 8.5 GHz	1.97 to 2.03 GHz	8 to 8.5 GHz
Realized RHCP gain	$\geq$ 6 dB	$\geq$ 12 dB	$\geq$ 6.9 dB	$\geq$ 11.96 dB
HPBW	$\pm$ 20°	$\pm$ 10°	$\pm$ 38°	$\pm$ 20°
Cross-coupling	≤ -25 dB		≤ -41 dB	≤ -39 dB
Port reflection	≤ -10 dB		≤ -18 dB	≤ -10.5 dB
Impedance bandwidth	60 MHz	0.5 GHz	150 MHz	-
Port input impedance	50 Ω		Yes	
Antenna dimensions	100 by 100 mm		82 by 82 mm	
Antenna height	$\leq$ 7 mm		5.732 mm	
All metals $\geq$ 100 mm must be grounded			Yes	

With the design of the SepAp antenna finalized and its simulated performance presented, the antenna design chapters are concluded. Chapter 7 presents prototypes of the two designed antennas. The measured performance of the prototypes is presented in Chapter 8.

7 ANTENNA PROTOTYPE FABRICATION AND ASSEMBLY

Chapters 5 and 6 proposes two antenna designs, referred to as Cross and SepAp respectively. The designs have to be slightly adapted to adhere to limitations set by the manufacturer. This chapter describes adaptations made to adhere to fabrication limitations and present the two fabricated antenna prototypes.

Simulation and measurement results for the two fabricated prototype antennas are presented in Chapter 8.

Both designs are based on the Rogers RT5870 material which was found to be unavailable during the thesis. Therefore the antenna prototypes are fabricated using Rogers RT5880. The two materials are available in the same dimensions. Rogers RT5880, however, has a relative permittivity of $\epsilon_r = 2.2$ and a slightly lower loss tangent. This has an effect on the antenna performance, however, it is expected to be minimal since the material constants are similar. The SepAp design is slightly re-fitted to the new substrate, the Cross design is not.

Both antenna designs have multiple substrate and copper layers. Due to fabrication limitations with the chosen material, the prototype antennas are split into multiple single layer Print Circuit Boards (PCBs). To connect the PCBs, VIAs terminated in copper pads are used for the first design. The second design utilizes soldered wires. M2 screws and bolts are used to fasten the layers tightly together, this will keep the antenna structure aligned and solid. The primary reason for choosing this approach as opposed to a standard multi-layer print is that the chosen RT5880 material only comes as core material, and no matching pre-preg is available.

For standard multi-layered prints, a symmetric stack-up is preferred to avoid e.g. flexing of layers during assembly. By assembling the antenna from single layer PCBs this limitation can be avoided, as all layers are fabricated individually. The individually fabricated multi-layer design allows for more flexible VIA positioning and dimensioning between copper layers. Figure 6.2 shows the stack-up of the second design "SepAp" with VIAs between copper layer two and copper layer four (counting from the top). With the proposed design such a VIA can easily be realized.

The chosen manufacturer only has two substrate heights available. Thus the design is adapted to substrate of heights 0.254 and 1.575 mm. Additionally, all plated via holes must have a diameter of at least 0.35 mm for manufacturability.

7.1 STRIPLINE TO MICROSTRIP TRANSITION

Both designs have feed networks made from stripline. Ideally, a through hole connector is attached directly to the end of the feeding stripline. For prototyping, it is more convenient to attach a surface mounted connector to a microstrip. Therefore a transition from stripline to microstrip is used. This section investigates a simple microstrip to stripline transition.

The difference between striplines and microstrips is the absence of a substrate and ground layer in the case of microstrips. Due to the absence of a substrate and ground layer, all the of the field is not contained within the substrate. This means that the effective relative permittivity of the microstrip is lower, and it therefore has to be wider to achieve the same impedance.

The transition is done by simply stepping up the line width when going from stripline to microstrip, as seen in Figure 7.1a. However simulations show that grounded VIAs around the stripline are required. Figure 7.1b shows a model of a stripline encapsulated in grounded VIAs.

Figure 7.2 shows the simulated S_{21}-parameters of the models shown in Figures 7.1a and 7.1b together with the simulated S_{21}-parameter of an equal length stripline. The simulations show that the transition without the grounding VIA encapsulation results in a "noisy" S_{21}-parameter. The grounding VIAs provides a smoother and higher S_{21}-parameter across the frequency ranges of interest. The simulation shows that the transition introduces a loss of 0.10 dB at 2 GHz and 0.04 dB at 8.25 GHz.

It is suspected that without the grounding VIAs the microstrip to stripline transition causes the microstrip to excite more modes than the desired TEM mode of the stripline. The VIAs are added to ensure only the desired mode is exited. Figure 7.1b shows the model of the transition with grounding VIAs along the lines.

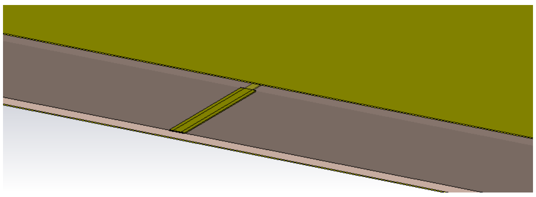

(a) CST model of the microstrip to stripline transition.

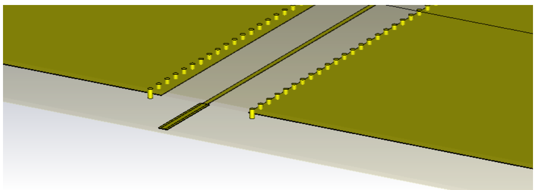

(b) CST model of the microstrip to stripline transition, with the lines and the VIAs highlighted.

Figure 7.1: Models of the microstrip to stripline transformation.

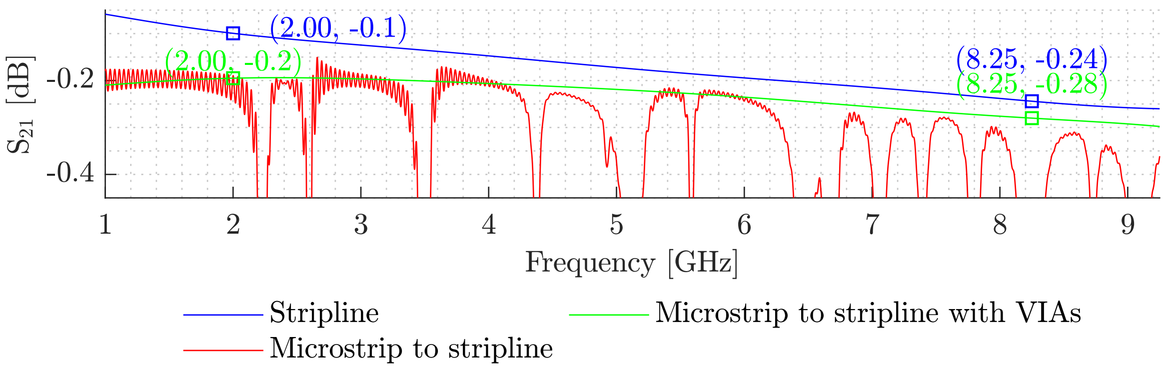

Figure 7.2: Simulated S_{21}-parameters of the two models seen in Figures 7.1a and 7.1b, together with a similar length stripline as reference.

7.2 FEEDING PROBE REALIZATION

As specified previously, the antenna prototypes are assembled from multiple single-layer PCBs. This means multi-layer VIAs has to be connected manually between the single-layer PCBs during assembly. Two different approaches are used to realize the feeding probes of the two antenna designs.

The SepAp antenna is fabricated with drill holes at the feeding points. A wire is manually cut, inserted, and soldered onto the PCB. A feeding pad is added to the end of the striplines to ease soldering. The drilled holes have a diameter of 0.9 mm and the wires have a diameter of 0.8 mm. A CST model of this feeding probe realization is shown in Figure 7.3.

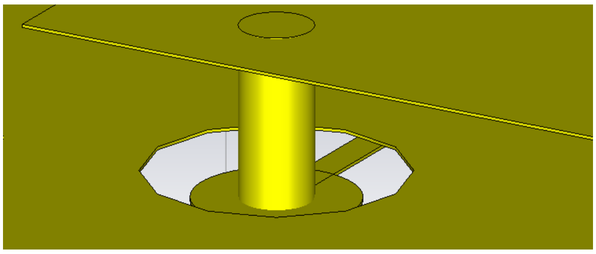

Figure 7.3: CST model of the feeding probe realization of the SepAp antenna design. The feeding proble is realized by a soldered metal wire between the feeding line and the antenna element.

For the Cross design, the multi-layer feeding probes are realized using plated VIAs terminated in copper pads. During assembly the layers are aligned and screwed together, relying on force to press the copper pad terminated plated VIAs together and create a connection. The VIAs have a diameter of 0.35 mm and the pads have a diameter of 0.6 mm.

Figures 7.4a and 7.4b shows two CST models of the Cross feeding probe realization. Both figures show substrate layers three and four of the antenna (counting from the top), see Figure 7.6 for an illustration of the stack-up. Figure 7.4a shows how the two layers are fabricated individually and Figure 7.4b shows how the two layers are pressed together to realize the feeding probe.

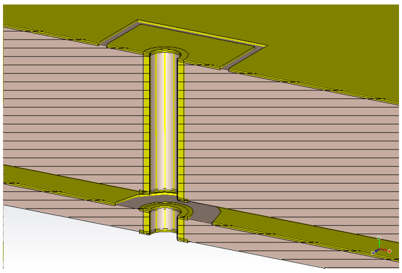

(a) Cross-sectional view of the antenna feeding probe for antenna layers three and four of the cross antenna prototype. The layers are separated by an air gap.

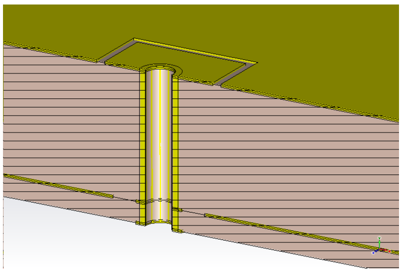

(b) The same as Figure 7.4a, however for this figure the antenna layers have been pressed together to illustrate how the antenna feeding probe is realized during assembly.

Figure 7.4: Two CST models showing how the antenna feeding probe is realized for the cross prototype antenna design.

Sections 7.3 and 7.4 presents the fabricated single-layer PCBs and the assembled antennas. Tests are conducted and presented in Chapter 8

7.3 SHARED APERTURE PROTOTYPE (CROSS)

This section presents the assembled cross antenna prototype and the minor modifications made to meet fabrication limitations.

Figure 7.5 shows CST models of the antenna after the modifications. A metal screw is added to the center of the antenna, and four Teflon screws are added to the corners of the antenna. The feeding network is enclosed in ground using grounded VIAs between the upper and lower ground layers. The size of the bottom substrate layer is reduced to accommodate the stripline to microstrip transformation and SMA connector.

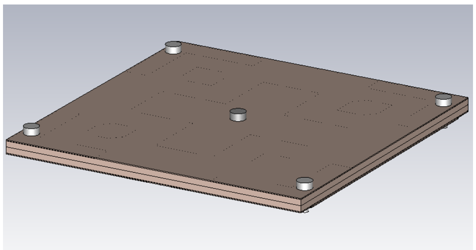

(a) Illustration of the antenna assembled antenna.

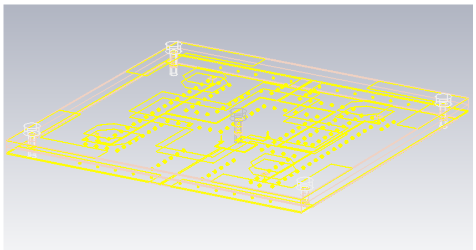

(b) Wireframe illustration of the antenna assembled antenna.

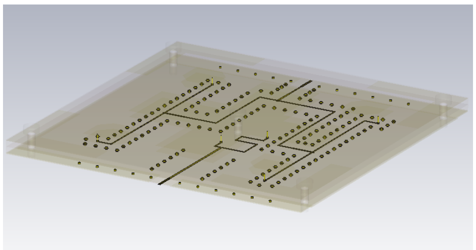

(c) Illustration of the cross antenna with the feeding network highlighted.

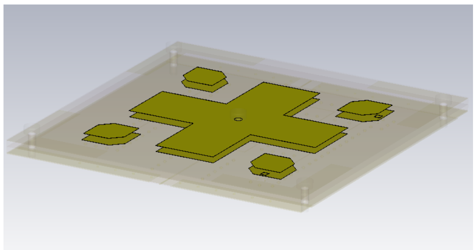

(d) Illustration of the cross antenna with the patch antenna elements highlighted.

Figure 7.5: Four illustrations of the cross antenna design.

Figure 7.6 shows the stack-up and Table 7.1 shows the dimensions of the Cross antenna prototype.

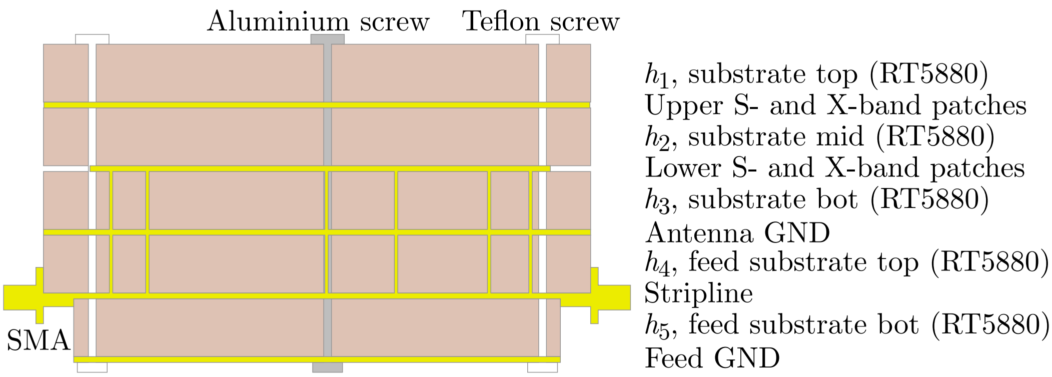

Figure 7.6: Cross-sectional view of cross antenna design.

Table 7.1: Table summarising the dimensions of the antenna prototype.

Parameter	*S-band*	*X-band*
Substrate Type	RT5880	
Substrate Height (Feeding)	0.254 mm	
Substrate Height (Under Patch)	1.575 mm	
Substrate Height (Under Patch)	1.575 mm	
Substrate Height (Over Patch)	0.254 mm	
Feed Line Height	0.035 mm	
Board size	82 mm	
Ground side shield length	25 mm	
Ground side shield width	6.0 mm	
Feed line Width 50 Ω	0.32 mm	
Feed line Width 35 Ω	0.49 mm	
Quarter wave transformer length	25.0 mm	5.8 mm
Untrimmed Patch Length Top	52.1 mm	9.86 mm
Untrimmed Patch Width Top	16.0 mm	9.86 mm
Patch Corner Trim Top	-	4.07 mm
Untrimmed Patch Length Bottom	51.8 mm	10.49 mm
Untrimmed Patch Width Bottom	16.0 mm	10.49 mm
Patch Corner Trim Bottom	-	4.05 mm
Feeding point (Distance from center)	8.20 mm	3.80 mm
Feed Pin diameter	0.35 mm	0.35 mm
Ground Cut out Radius	0.60 mm	0.60 mm
Solder Pad radius	0.30 mm	0.30 mm
Feeding cut inner diameter	-	1.4 mm
Feeding cut outer diameter	-	1.6 mm
Antenna separation	-	45 mm

Figure 7.7 shows pictures of the assembled cross antenna prototype and relevant individual layers.

Figures 7.7a and 7.7b show the antenna placed on a single wooden plate. Before X-band measurement, an additional layer of wood is added on the bottom of the antenna. This is done to stabilize and support the connector as the antenna prototype is found to be very fragile due to the flexibility of the substrate. With the extra wooden plate, the connector is less likely to put a damaging strain on the bottom PCB layer.

The wooden plate does not have the same radiation properties as air and might affect the impedance of the microstrip line. However, the additional connector support was required doing testing to ensure the prototype would not break.

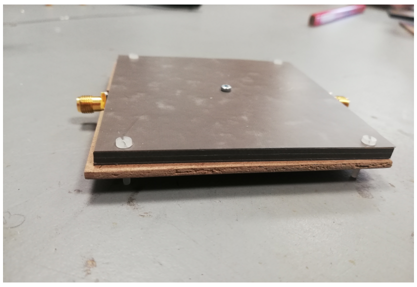

(a) Top view of the assembled cross antenna prototype.

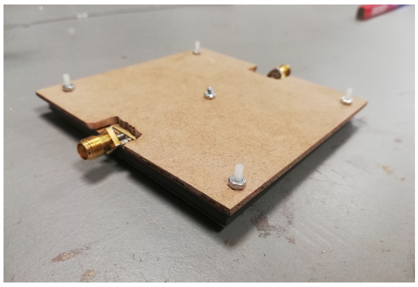

(b) Bottom view of the assembled cross antenna prototype.

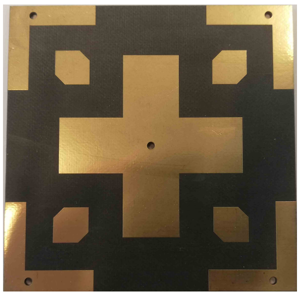

(c) Top view of substrate layer two containing the upper cross patch, X-band patches, and corner shields.

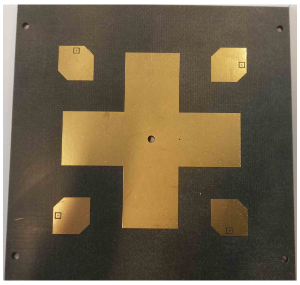

(d) Top view of substrate layer three containing the lower cross patch and x-Band patches with rectangular slots around the feeding point.

(e) Bottom view of substrate layer three containing feeding VIAs.

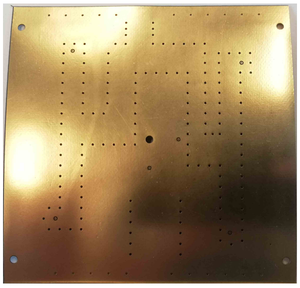

(f) Top view of substrate layer four containing the antenna ground layer, grounding VIAs for the feeding network, and feeding VIAs for the antennas.

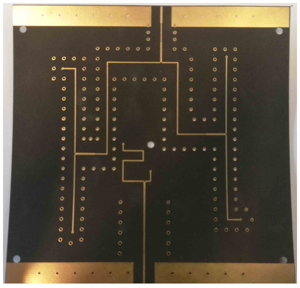

(g) Bottom view of substrate layer four containing the stripline feeding network.

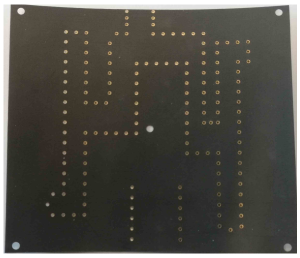

(h) Top view of substrate layer five containing grounding VIAs for the feeding network.

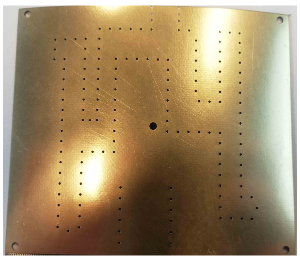

(i) Bottom view of substrate layer five containing a ground layer. Grounding VIAs for the feeding network are visible.

(j) Zoomed picture of bottom of layer three where two feeding VIAs are more visible.

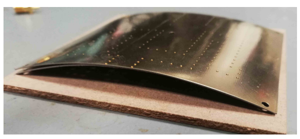

(k) Bottom of substrate layer four seen from the side, showing the curvature of the print due to the flexibility of the substrate.

Figure 7.7: Pictures of the assembled cross antenna prototype and individual layers two to five. Layer one is substrate on top of antenna and layer five contains the ground layer below the stripline feeding network.

7.4 SEPARATE APERTURE PROTOTYPE (SEPAP)

This section presents the assembled SepAp antenna prototype and the minor modifications made to meet fabrication limitations.

The SepAp antenna design is already designed with single-layer assembly in mind but has to be re-dimensioned for the change in substrate. Table 7.2 shows the dimensions of the designed and fabricated antenna. Since the maximum standard height of Rogers RT5880 is 1.575 mm, the substrate height $h_2 = 3.150$ mm is realized by two layers of height 1.575 mm.

Table 7.2: Dimensions and material of designed and fabricated antenna. Dimensions of delay bends in the feeding networks are not listed, but are fitted to desired phase shifts. Stripline widths are left unchanged.

Name	*Designed*	*Fabricated*
substrate material	Rogers RT5870	Rogers RT5880
substrate size	82 mm	82 mm
substrate height h_2	3.150 mm	3.150 mm
substrate height h_3	1.575 mm	1.575 mm
substrate height h_1, h_4, and h_5	0.254 mm	0.254 mm
padW	1.8 mm	1.8 mm
padCutW	2.8 mm	2.8 mm
padLineL	1.3 mm	1.3 mm
padLineW	0.4 mm	0.4 mm
sPatchL	48.45 mm	49.75 mm
sPatchW	12 mm	12 mm
sFeedOffset	5 mm	5.5 mm
sQuaterWaveLength	25.55 mm	26.27 mm
xPatchL	11.13 mm	11.07 mm
xPatchW	8.57 mm	8.52 mm
xFeedOffsetL	4.27 mm	4.24 mm
xFeedOffsetW	1.98 mm	2.21 mm
xQuaterWaveLength	6.03 mm	6.54 mm
probeD	0.8 mm	0.8 mm
probeGroundCutoutD	2.86 mm	2.86 mm

Figure 7.8 shows pictures of the assembled SepAp antenna prototype and relevant individual layers.

During measurement preparations, the bottom substrate layer broke near the X-band port, due to the torque applied when connecting cables between the X-band SMA connector and the measurement equipment. The antenna has been repaired by applying extra soldering tin to connect the disconnected ground layer, and a thin wire is soldered along the stripline. Measurements show that the S-parameters are nearly identical after the repair.

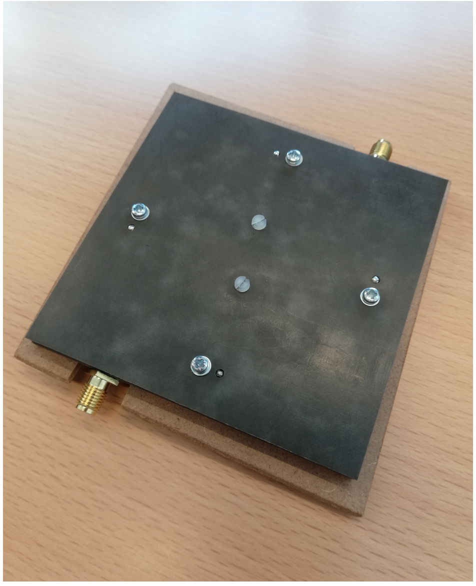

(a) Top view of assembled SepAp antenna prototype.

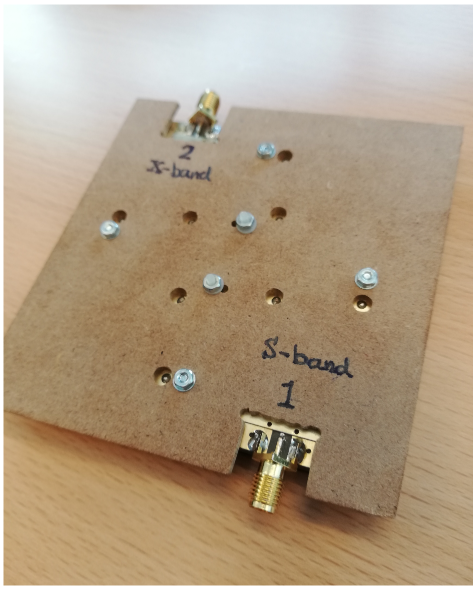

(b) Bottom view of assembled SepAp antenna prototype.

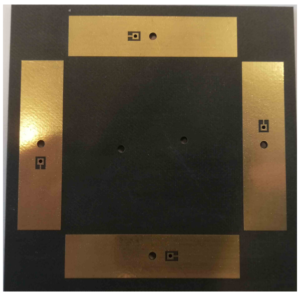

(c) Top view of substrate layer two containing the S-band patches.

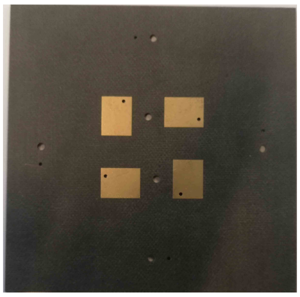

(d) Top view of substrate layer four containing the X-band patches.

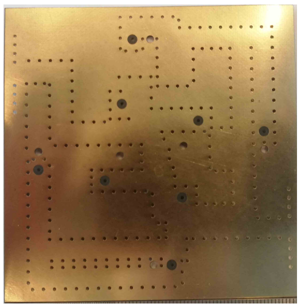

(e) Top view of substrate layer five containing the antenna ground layer and grounding VIAs for the feeding network.

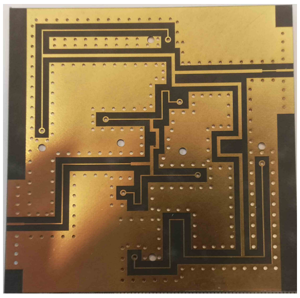

(f) Bottom view of substrate layer five containing the stripline feeding network and grounding VIAs..

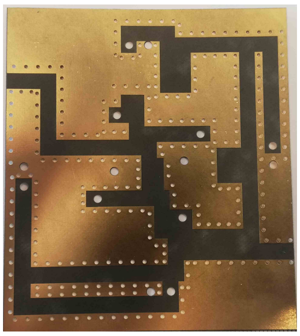

(g) Top view of substrate layer six containing grounding VIAs for the feeding network.

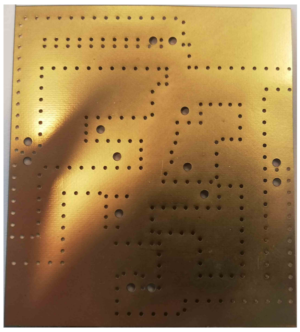

(h) Bottom view of substrate layer six containing the bottom ground layer for the stripline.

Figure 7.8: Pictures of the assembled SepAp antenna prototype and individual layers two and four through six. Layer one is substrate on top of antenna, layer three is pure substrate, and layer six contains the ground layer below the stripline feeding network.

8 ANTENNA TEST AND MEASUREMENT

Chapter 7 presents two prototype antennas. The prototypes are tested to verify whether they satisfy the requirements set forward in Chapter 4. This chapter presents the measurement procedure, data processing, and measurement results.

8.1 TEST PROCEDURE

The measurement campaign is split into three parts:

1. S-Parameter measurement using network analyser.
2. S-band radiation measurement using SATIMO measurement chamber.
3. X-band radiation measurement in an anechoic chamber.

The SATIMO measurement chamber is able to measure the full spherical radiation pattern in a matter of minutes and is therefore preferred for the radiation measurements. The SATIMO measurement chamber has a maximum frequency of 6 GHz and is therefore only be used for the S-band radiation measurement.

8.1.1 S-PARAMETER MEASUREMENT

For the S-parameter measurement, a Keysight Technologies N5227A-US56070644 network analyser is used. Figure 8.1 shows a picture of the measurement and calibration setup.

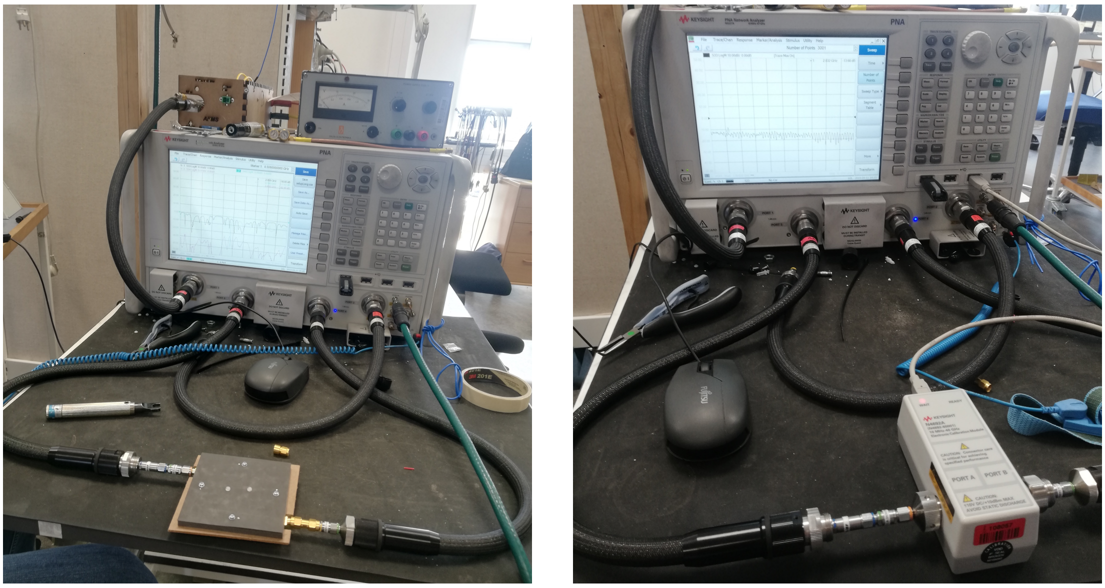

(a) Picture of S-parameter measurement. The antenna prototype is connected to the network analyser and S-parameters can be read on the display.

(b) Picture of network analyser calibration using Keysight N4692A calibration module. The calibration module is connected to the network analyser.

Figure 8.1: Pictures of S-parameter measurement and calibration.

The measurement procedure is as follows:

1. Set frequency range to 1 to 10 GHz.
2. Calibrate using calibration kit or module suitable for the frequency range. For this measurement, a Keysight N4692A calibration module is used.
3. Connect S-band antenna port to network analyser port 1.
4. Connect X-band antenna port to network analyser port 2.
5. Save measured S-parameters.

8.1.2 S-BAND RADIATION MEASUREMENT

The S-band radiation is measured in a SATIMO measurement chamber as shown in Figure 8.2.

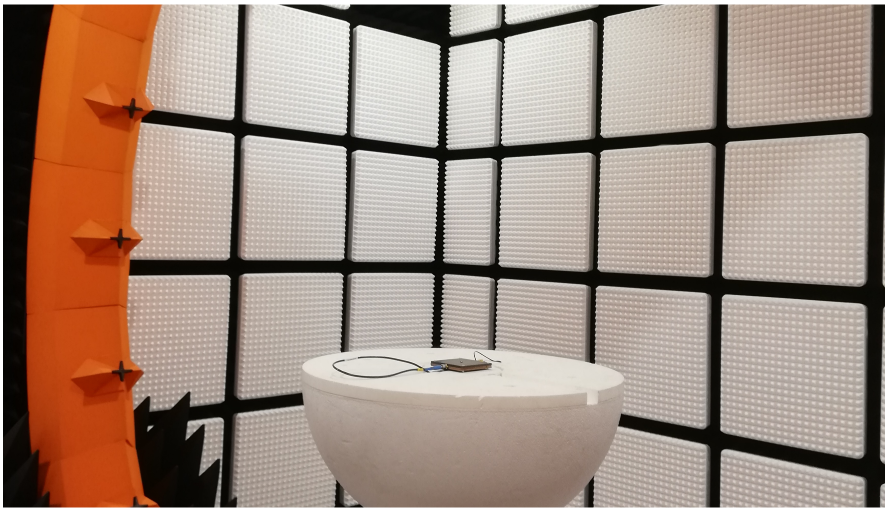

Figure 8.2: Picture of antenna prototype in SATIMO measurement chamber. The antenna is positioned on a pedestal in the center of the chamber. The orange blocks to the left contain measurement antennas and form a circle, not shown on the picture, which encloses the antenna prototype. The pedestal is rotated and tilted during measurement to measure the whole sphere around the antenna prototype.

The measurement procedure is as follows:

1. Set frequency range to 1.9 to 2.3 GHz.
2. Connect calibration antenna on the measurement pedestal and run calibration program.
3. Disconnect calibration antenna and connect S-band antenna port on the measurement pedestal and connect X-band antenna port to a 50 Ω termination.
4. Run measurement and save results.

The SATIMO measurement chamber software system is able to automatically calibrate using a supported reference antenna and process the data to output the desired farfield gains and axial ratio. No manual data processing or calibration is done since the resulting output file already contains all the desired processed data.

8.1.3 X-BAND RADIATION MEASUREMENT

The X-band radiation characteristic is measured in an anechoic chamber as shown in Figure 8.3.

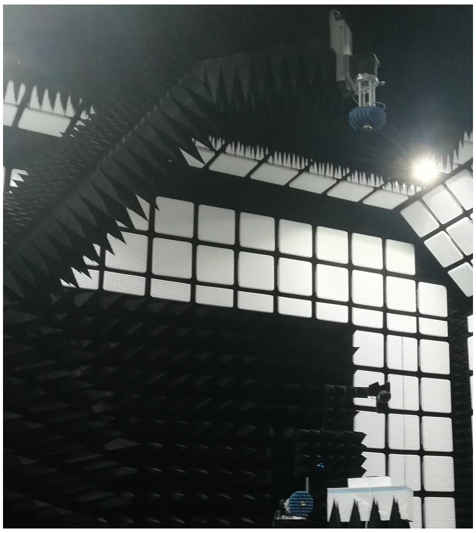

(a) Picture of X-band radiation measurement showing antenna prototype placed on rotating pedestal (bottom right) and measurement antennas on mechanical arm (middle top). The mechanical arm is in the $\theta = 0°$ position.

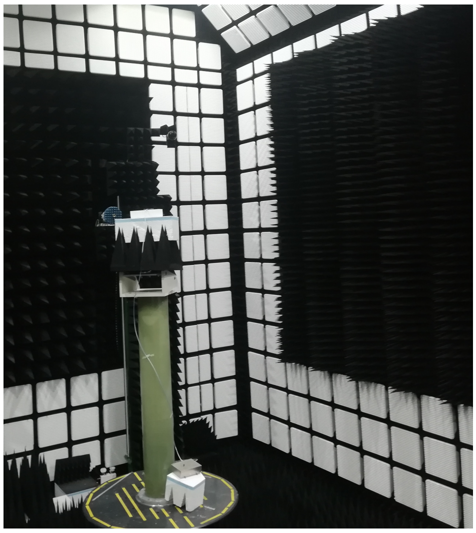

(b) Picture of X-band radiation measurement showing antenna prototype placed on rotating pedestal (middle left).

Figure 8.3: Pictures of the anechoic chamber X-band measurement.

During measurement, the antenna prototype is placed on a rotating pedestal centred in the chamber. The upper sphere is measured by moving a mechanical arm with a reference antenna in the range $\theta_{\text{range}} = 0$ to $90°$ while the center pedestal is rotated in the range $\phi_{\text{range}} = 0$ to $360°$. With the antenna pointing upwards, the broadside direction is $\theta = 0°$.

The measurement procedure is as follows:

1. Set frequency range to 8 to 9.3 GHz.
2. Connect reference antenna on the measurement pedestal. An A-Info LB-SJ-60180 dual-polarized horn antenna is used for this measurement. The reference antenna is a two-port design, so only the horizontal port is connected to the measurement pedestal.
3. Run a calibration measurement with $\theta = 0°$ and $\phi \in 0$ to $360°$ to measure broadside gain. ϕ is rotated so data processing can account for any misalignments.
4. Disconnect calibration antenna and connect X-band antenna port on the measurement pedestal and connect S-band antenna port to a $50\,\Omega$ termination.
5. Run measurement with $\theta_{\text{range}} = 0$ to $90°$ and $\phi_{\text{range}} = 0$ to $360°$ to measure the upper sphere.
6. Save measurement data.

The measurement data contains measured S-parameters between the antenna under test and the two (one horizontal and one vertical) linear measurement antennas in linear scale. The data has to be processed to extract the desired data.

8.2 DATA PROCESSING

This section covers how the X-band antenna radiation measurements are calibrated and processed into gains and axial ratios.

8.2.1 CALIBRATION

The measured data has to be calibrated to the propagation losses, measurement antenna gains, and phase shifts. This is done by multiplying the measured data by a frequency dependent factor unique to the measurement setup.

The measurement data is given in the form of S-parameters $\mathrm{S}_{RT} = \frac{V_R^-}{V_T^+}$. The time-averaged powers delivered to the reference antenna and received by the measurement antenna is given by Equation (8.1) [7].

$$P_T = \frac{|V_T^+|^2}{2R_T} \quad , \quad P_R = \frac{|V_R^-|^2}{2R_R}. \qquad \text{[W]} \quad (8.1)$$

Where:

V_T^+	=	ingoing wave at test antenna port (transmitter)	[V]
V_R^-	=	outgoing wave at measurement antenna port (receiver)	[V]
R_T	=	resistance of test antenna port	[Ω]
R_R	=	resistance of measurement antenna port	[Ω]

The power delivered to the measurement antenna can also be expressed in terms of transmitter gain and receiver effective aperture as in Equation (8.2) [8].

$$P_R = G_T \frac{P_T A_R}{4\pi r^2} \implies |\mathrm{S}_{RT}|^2 = G_T \frac{R_R A_R}{R_T 4\pi r^2} = \frac{G_T}{K_R} \implies \sqrt{G_T} = \mathrm{S}_{RT} \cdot C_R \qquad (8.2)$$

Where:

r	=	distance between antennas	[m]
A_R	=	polarization dependent effective receiver aperture	$\left[\mathrm{m}^2\right]$
G_T	=	test antenna gain	[1]
K_R	=	$\frac{R_T 4\pi r^2}{R_R A_R}$ = power gain calibration factor	[1]
C_R	=	$\sqrt{K_R} \cdot \mathrm{e}^{-j\angle S_{RT}}$ = field gain calibration factor	[1]

As seen from Equation (8.2), calibration has to be applied to the measured data, before the test antenna gain can be extracted. To calibrate, the measured data is multiplied by a calibration factor C_R dependent on the orientation and frequency. To calibrate both measurement antennas, a calibration factor is therefore needed for both the θ and ϕ components: C_θ and C_ϕ.

To determine the two calibration factors, a measurement is done using a reference antenna with a known gain characteristic. The measurement gives two S-parameters, one for each field-component, $\mathrm{S}_{\theta T}$ and $\mathrm{S}_{\phi T}$. The calibration factor is then calculated as $C_x = \frac{\sqrt{G_x}}{\mathrm{S}_{xT}}$, where G_x is the reference antenna gain in the x component, and x is either θ and ϕ.

As reference antenna an A-Info LB-SJ-60180 6 to 18 GHz dual polarized horn antenna is used [26]. Only the horizontal port of the antenna is used for these measurements.

As the reference antenna is linearly polarized, the gain in the orthogonal component is zero. Therefore calibration of both the θ and ϕ measurement antennas can not be done from a single data point. Instead the reference antenna is measured in the anechoic chamber for $\phi_{\text{range}} = 0$ to 360° and $\theta = 0$.

The calibration measurement of the A-Info horn antenna is seen in Figure 8.4. For calibration, the measured data at the rotational angle ϕ where the reference antenna is aligned with either the θ or ϕ direction is used. The reference antenna is aligned with the ϕ or θ component, when the measured data reaches a maximum.

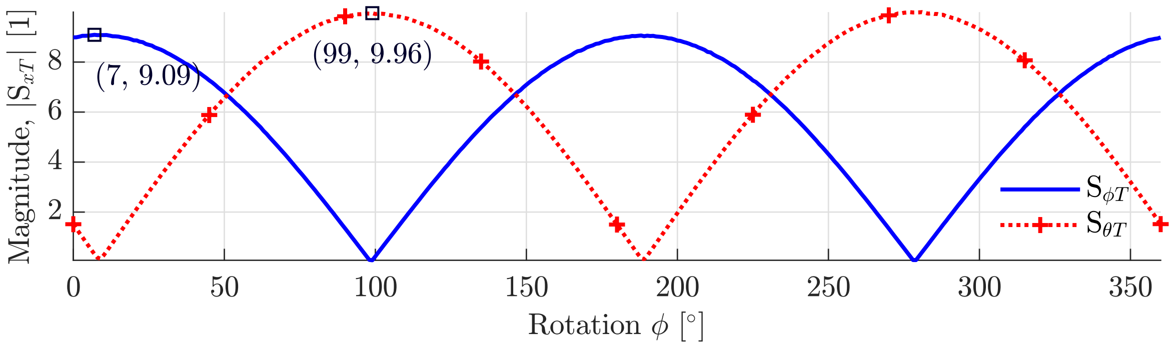

Figure 8.4: Calibration measurement results for frequency $f = 8$ GHz. The reference antenna is placed in the center of the anechoic chamber pointing in the $\theta = 0$ direction with allignment in the ϕ-axis. Reference antenna is measured for $\theta = 0$ and $\phi_{\text{range}} = 0$ to 360°.

Figure 8.4 shows how the data points used for calibration are extracted from the measurement, marked as black squares. The used data points are given by Equation (8.3).

$$\bar{S}_{xT} = \max_{\phi} (S_{xT}) \quad [1] \quad (8.3)$$

Where:

S_{xT}	=	measured data	[1]
$\bar{S}_{xT}$	=	data point used for calibration	[1]
x	=	θ or ϕ	[1]

With the the two maximums $\bar{S}_{\theta T}$ and $\bar{S}_{\phi T}$ found, the calibration factors are calculated using the horizontal gains from the reference antenna datasheet by Equation (8.4). This process is repeated for all frequencies of interest.

$$C_x = \frac{\sqrt{G_H}}{\bar{S}_{xT}} \quad [1] \quad (8.4)$$

Where:

G_H	=	horizontal gain from reference antenna datasheet	[1]

The calibration is applied to a measurement to calculate a phased field gain by Equation (8.5).

$$E_x = S_{xT} \cdot C_x \quad [1] \quad (8.5)$$

Where:

S_{xT}	=	measured data	[1]

E_x	=	phased field gain	[1]
x	=	θ or ϕ	[1]

The phased field gains are used to calculate antenna gains and axial ratio in the following section.

8.2.2 GAIN AND AXIAL RATIO

Given horizontal and vertical field gains E_ϕ and E_θ, the absolute gain and RHCP gain is given by Equations (8.6) and (8.7).

$$G_A = |E_\phi|^2 + |E_\theta|^2 \quad [1] \tag{8.6}$$

$$G_{\mathrm{RC}} = \frac{1}{2}|E_\phi + E_\theta \cdot \mathrm{e}^{-j\frac{\pi}{2}}|^2 \quad [1] \tag{8.7}$$

Where:

G_A	=	Absolute Gain	[dB]
G_{RC}	=	RHCP gain	[dB]
E_x	=	phased field gain for x polarization	[1]

The axial ratio is given by Equation (2.19) as shown in Equation (8.8).

$$AR = \sqrt{\frac{A_\phi^2 + A_\theta^2 + \sqrt{A_\phi^4 + A_\theta^4 + 2A_\phi^2 A_\theta^2 \cos\left(2\left(\varphi_\theta - \varphi_\phi\right)\right)}}{A_\phi^2 + A_\theta^2 - \sqrt{A_\phi^4 + A_\theta^4 + 2A_\phi^2 A_\theta^2 \cos\left(2\left(\varphi_\theta - \varphi_\phi\right)\right)}}} \quad [1] \tag{8.8}$$

Where:

A_x	=	$\lvert E_x \rvert$	[1]
φ_x	=	$\angle E_x$	[rad]

Measurement champaign results are presented in the next section.

8.3 RESULTS

This section will include a series of plots, showing various antenna performance metrics. All the plots contain simulated curves together with the measured curves after calibration.

First, the simulated and measured performance of the cross and SepAp prototype antennas is presented. In section Section 8.4 the performance of the two prototypes is compared to the requirements specified in Chapter 4.

S-band S-parameters
Figures 8.5 and 8.6 show the simulated and measured S-band S-parameters of the prototypes. The S-parameters has shifted upwards in frequency in the measurement compared to the simulations. Overall the S-band S-parameters looks similar. It is noted that the cross-coupling of the Cross prototype is measured to be around 10 dB lower than simulated.

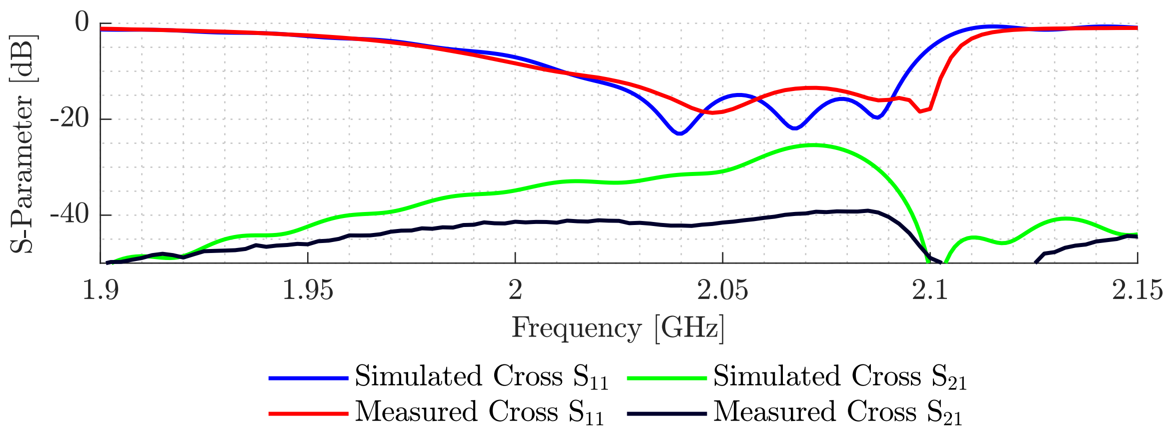

Figure 8.5: Simulated and measured S-Band S-parameters of the Cross antenna prototype.

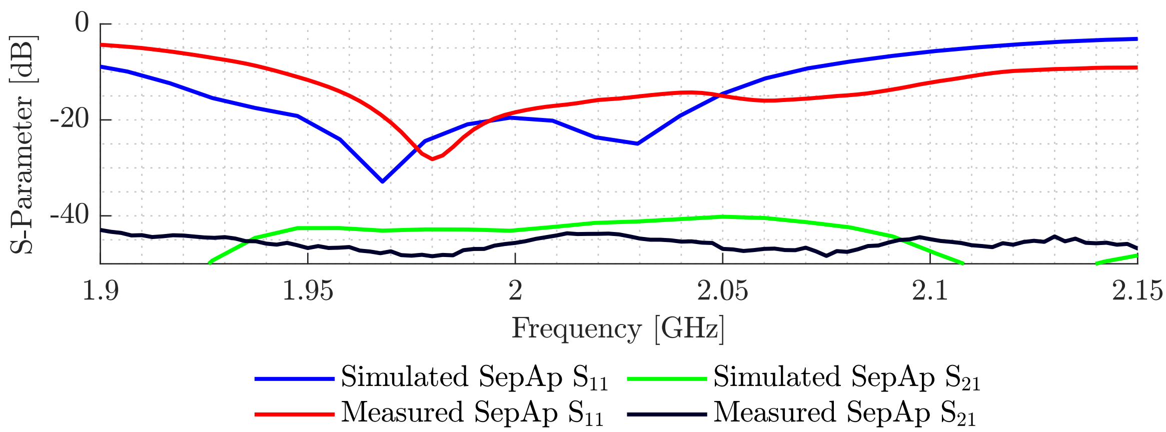

Figure 8.6: Simulated and measured S-Band S-parameters of the SepAp antenna prototype.

X-band S-parameters

Figures 8.7 and 8.8 show the simulated and measured X-band S-parameters of the prototypes.

Figure 8.7 shows that the measured S_{22} of the Cross prototype is significantly higher than simulated. A minimum S_{22} of -6.94 dB is observed at 8.41 GHz.

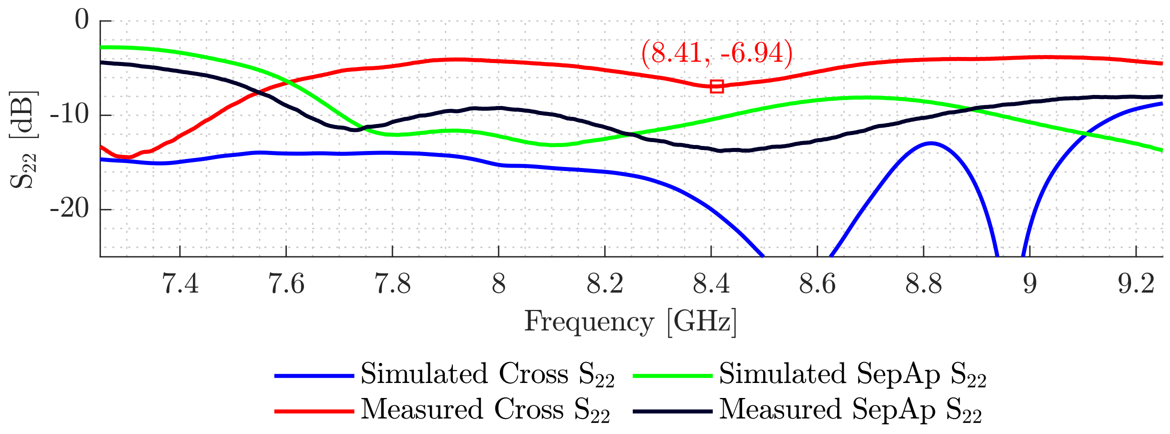

Figure 8.7: Simulated and measured X-Band S_{22} of the antenna prototypes.

Figure 8.8 shows that the Cross prototype has significantly higher than simulated cross-coupling. The maximum in-band cross-coupling is measured to be -25 dB at 8.5 GHz. Both of the measured S-parameters of the Cross prototype indicate a loss of realized RHCP gain compared to simulations.

The SepAp prototype shows measured results which are similar to the simulated, with an $S_{22} \leq -9.25$ dB and an S_{21} below -33 dB in the measured band.

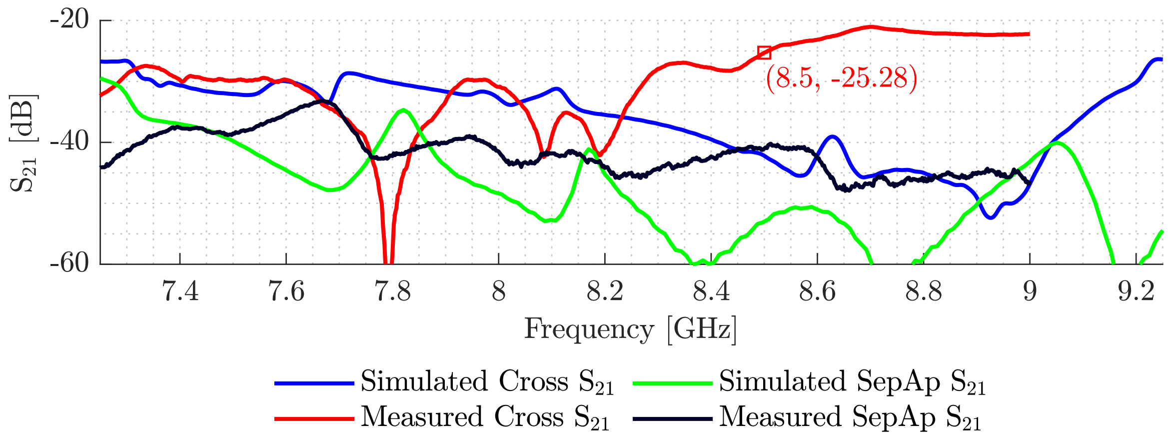

Figure 8.8: Simulated and measured X-Band S_{21} of the antenna prototypes.

S-band RHCP gain

Figure 8.9 shows the measured and simulated S-band realized RHCP gain of the prototypes in the broadside direction. The measured results show frequency offsets. The SepAp prototype shows a frequency offset of 60 MHz. The Cross prototype shows a frequency offset of 20 to 30 MHz. Both these frequency shifts are larger than expected from the S-parameters.

The SepAp prototype shows no significant difference when accounting for the frequency shift between the simulated and the measured gain characteristics. The Cross prototype shows narrower gain characteristics resulting in a low gain in the higher part of the band.

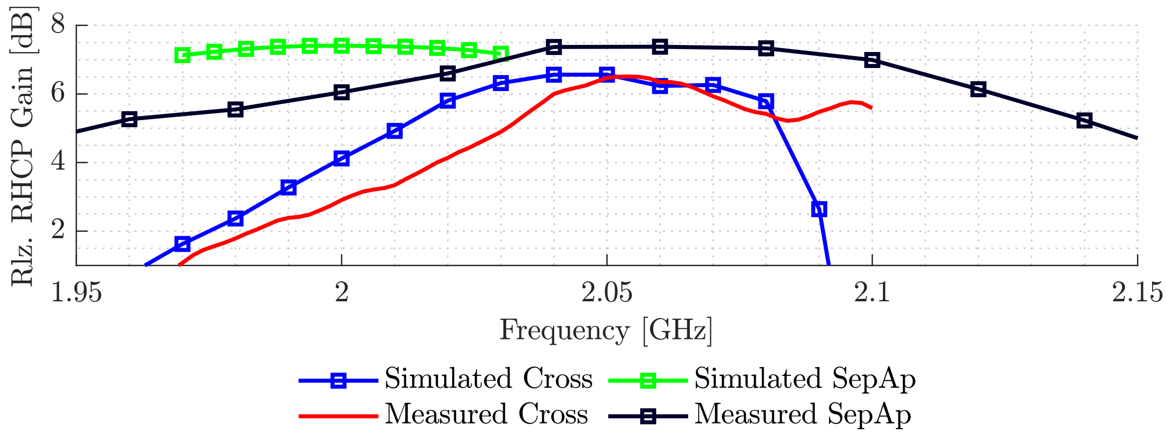

Figure 8.9: Simulated and measured S-band broadside realized RHCP gain of the prototypes, in the broadside direction.

X-band gain

Figure 8.10 shows the measured and simulated X-band realized RHCP gain of the prototypes.

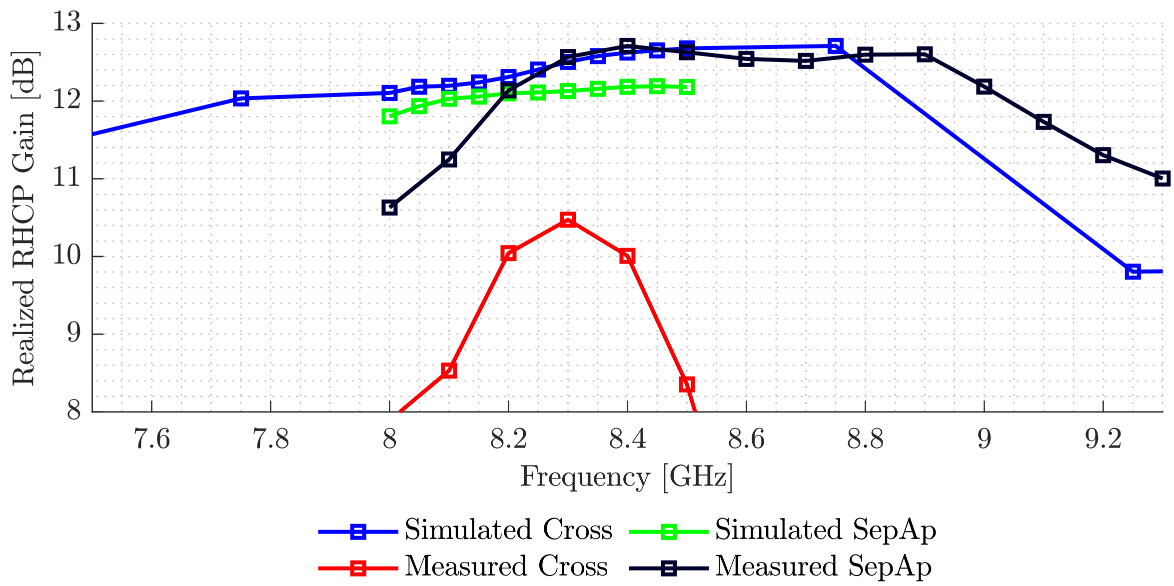

Figure 8.10: Simulated and measured X-band broadside realized RHCP gain of the prototype antennas, in the broadside direction.

As expected from the S-parameters the Cross prototype has a lower measured realized RHCP gain compared to simulations. The Cross prototype shows an overall gain loss of ≤ 2 dB.

The SepAp prototype shows differences between the simulation and measurement as well. The realized RHCP gain at 8.0 GHz is measured to be 1.2 dB lower than simulated, and the measured gain at 8.4 GHz is measured to be approximately 0.5 dB higher. This might indicate that a frequency shift of 0.2 GHz, which results in the higher gain.

Axial ratio

Figures 8.11 and 8.12 show the simulated and measured axial ratio of the prototype antennas in the S-band and X-band respectively.

The X-band axial ratio shows some differences between simulation and measurement. However, the ratio is well below 3 dB in a wide frequency range indicating good polarization.

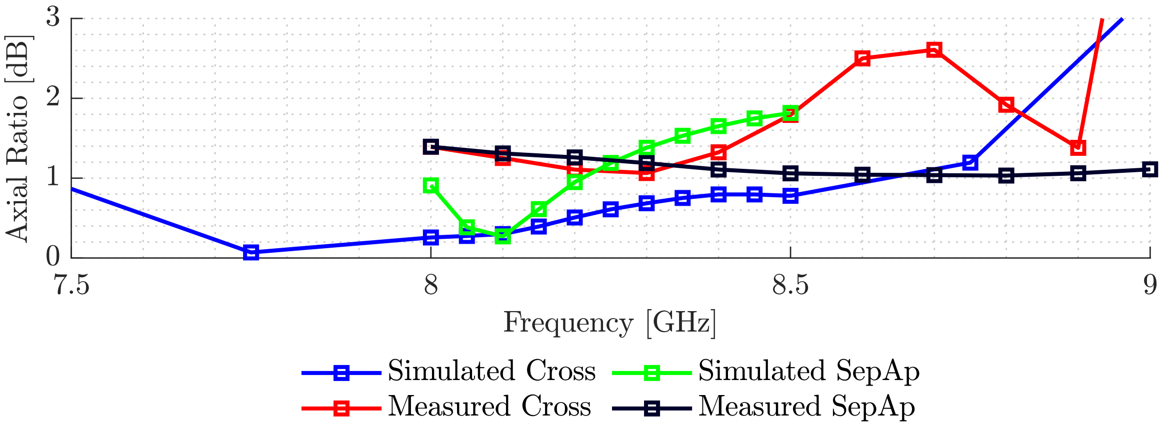

Figure 8.11: Simulated and measured X-band broadside axial ratio of the prototype antennas.

In the S-band the axial ratio also shows some differences between the simulation and measurements. The measured performance of the SepAp prototype is significantly better that the simulation predicts. The Cross prototype shows similar performance although with a frequency offset.

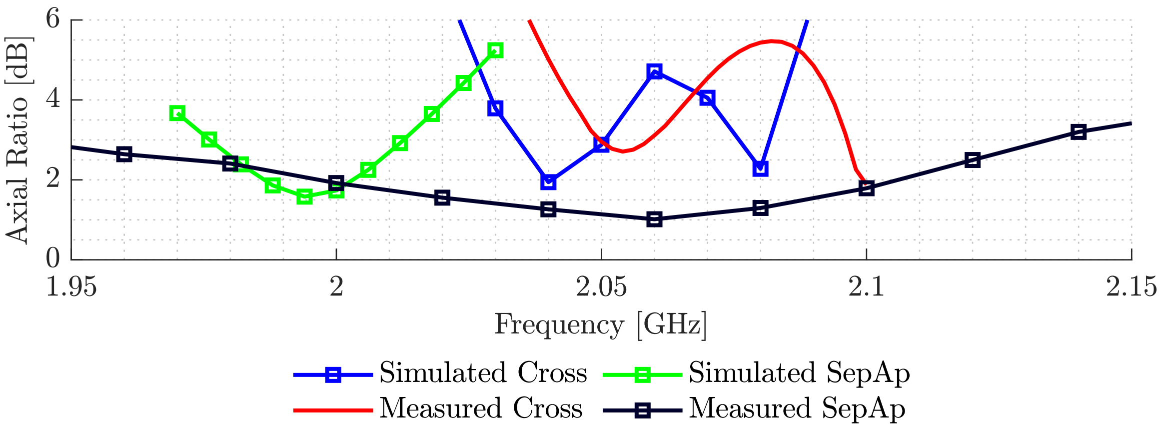

Figure 8.12: Simulated and measured S-band broadside axial ratio of the prototype antennas.

Radiation pattern - Seperate aperture (SepAp)
Figure 8.13 shows the measured realized RHCP gain patterns of the SepAp prototype. The patterns are similar to simulations and show one strong main-lobe and no significant side-lobes.

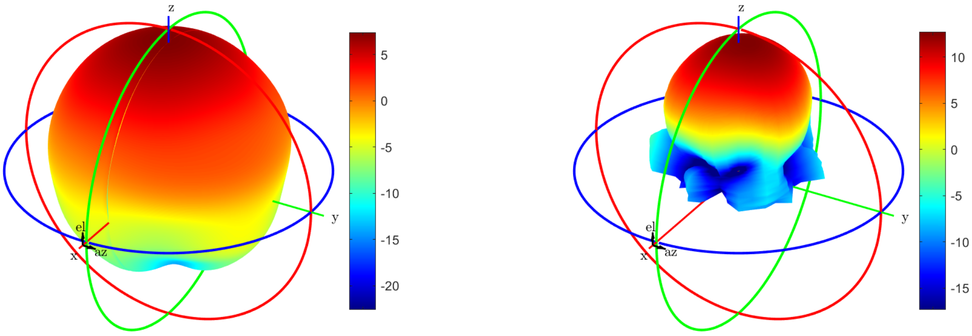

(a) Measured S-Band realized RHCP gain pattern pattern of the SepAp antenna at 2.04 GHz.

(b) Measured X-Band realized RHCP gain pattern pattern of the SepAp antenna at 8.3 GHz.

Figure 8.13: Measured radiation pattern of the SepAp antenna prototype.

Radiation pattern - Shared aperture (Cross)
Figure 8.14 shows the measured realized RHCP gain patterns of the Cross prototype. The S-band pattern has one strong main-lobe, and the X-band patten has a strong broadside main-lobe and side-lobes as expected due to the X-band antenna element separation.

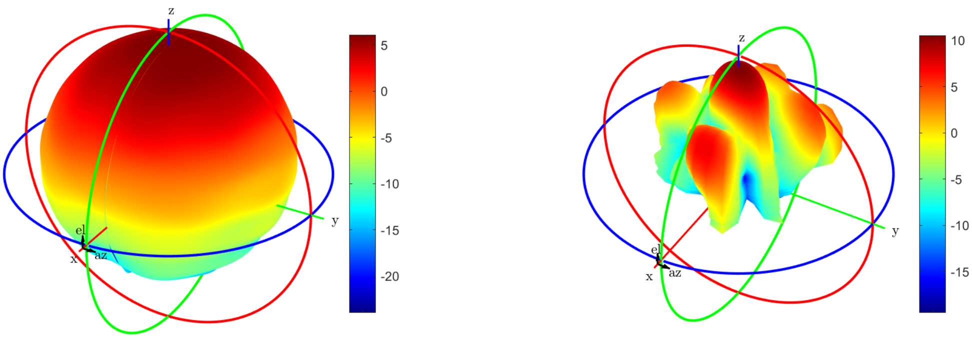

(a) Measured S-Band realized RHCP gain pattern of the Cross 1 antenna at 2.04 GHz.

(b) Measured X-band realized RHCP gain pattern pattern of the Cross 2 antenna at 8.3 GHz.

Figure 8.14: Measured radiation pattern of the Cross antenna prototype.

Figure 8.15 shows a rectangular view of the measured Cross prototype radiation pattern at 8.3 GHz (A different representation of the data in Figure 8.14b). The realized RHCP gain in the side-lobes is ≤ 7 dB and the main-lobe has a gain of 10.5 dB.

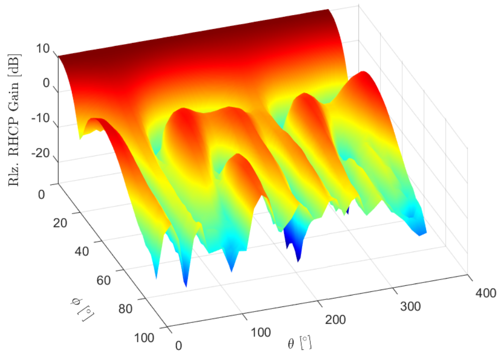

(a) Rectangular view of the Cross realized RHCP gain pattern measured at 8.3 GHz.

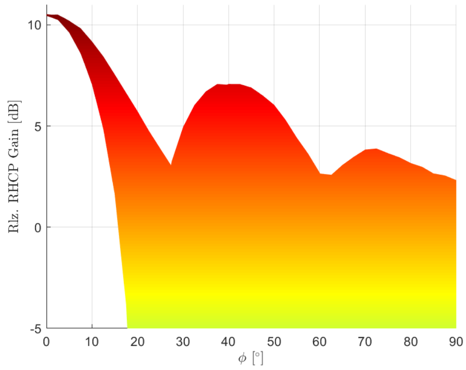

(b) Figure 8.15a viewed from the side.

Figure 8.15: Measured radiation pattern of the Cross antenna prototype.

Radiation pattern slices - Shared aperture (Cross)

Figure 8.16 shows the simulated X-band $\phi = 90°$ and $\theta = 90°$ slices and measured X-band $\phi = 0°$ and $\phi = 90°$ slices for the Cross antenna prototype at 8.3 GHz. The difference in angles is due to the fact that the antenna is measured facing the Z-axis and simulated facing the Y-axis of the three-dimensional coordinate system (see Section 2.1).

The realized RHCP gain in the broadside direction is the expected 10.5 dB, as observed in Figure 8.10. With the measured minimum side-lobe level of 3.43 dB, the relative main-lobe to side-lobe ratio between the simulation and the measurement remains approximately the same: $(12.41 - 8.07) - (10.51 - 7.08) = 0.91$ dB.

Additionally Figure 8.16 shows that the Cross prototype has a measured X-band HPBW of 20° and 24°, which is in agreement with the simulation.

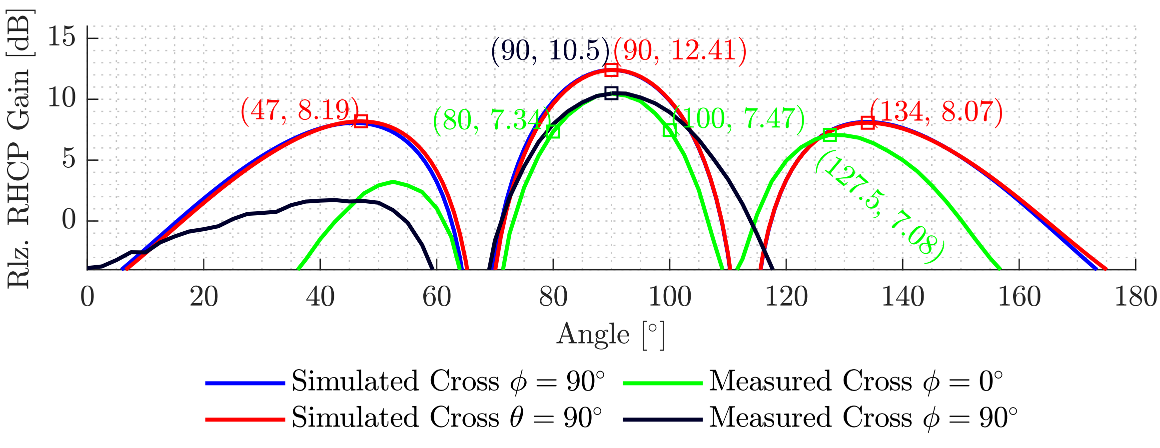

Figure 8.16: X-band radiation pattern slice of the Cross antenna prototype at 8.3 GHz.

Figure 8.17 shows the S-band $\phi = 90°$ and $\theta = 90°$ slices of the simulated antenna and the measured slice equivalent. Both slides are for a frequency of 2.05 GHz. The simulated and measured S-band antenna radiation patterns are similar.

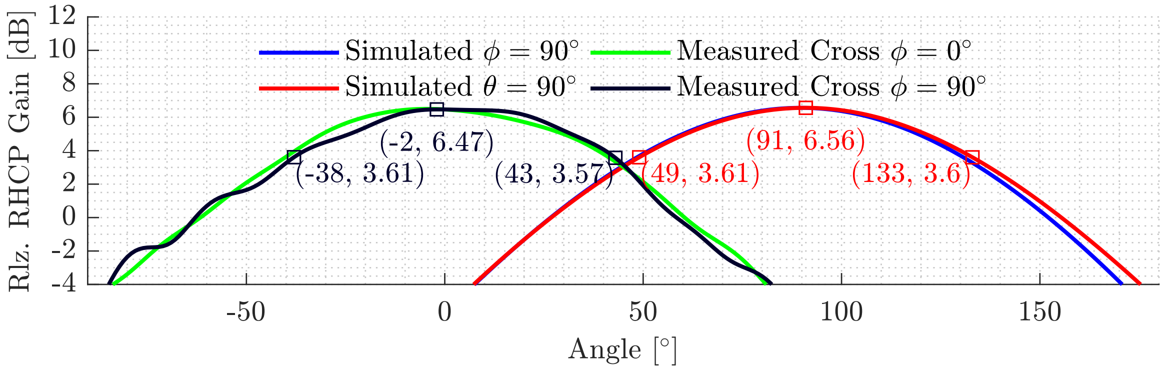

Figure 8.17: S-band radiation pattern slice of the Cross antenna prototype at 2.05 GHz.

Radiation pattern slices - Separate aperture (SepAp)

Figures 8.18 and 8.19 show the measured $\phi = 0°$ and $\phi = 90°$ slices for the SepAp prototype in the X- and S-band respectively. As seen from the figures the HPBW is approximately the same for both simulation and measurement, in both bands.

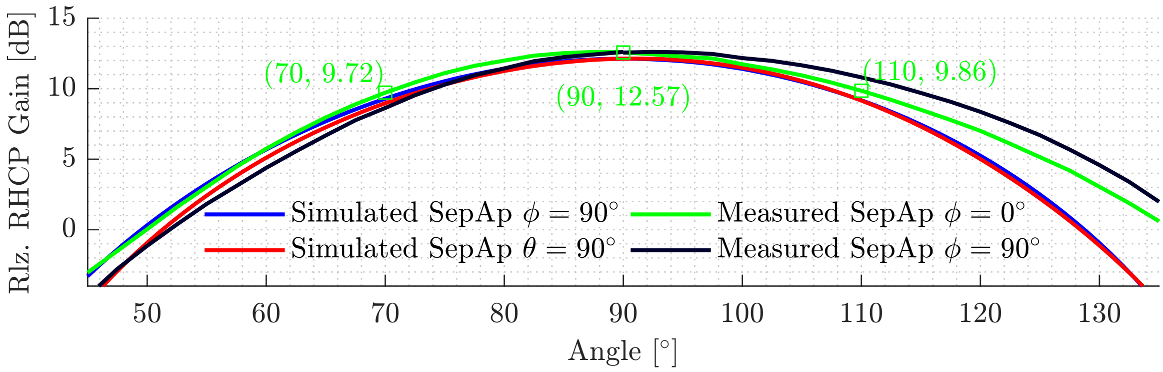

Figure 8.18: X-band radiation pattern slice of the SepAp antenna prototype at 8.3 GHz.

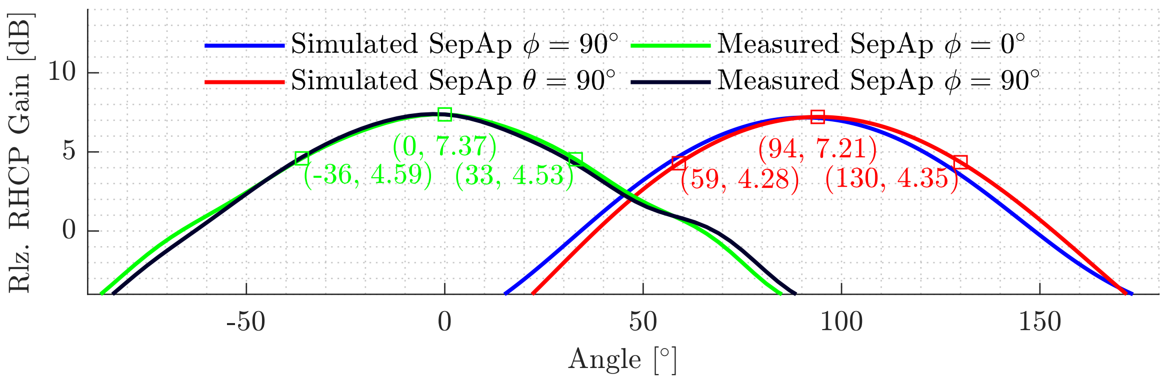

Figure 8.19: S-band radiation pattern slice of theSepAp antenna prototype at 2.04 GHz.

8.4 DISCUSSION OF TEST RESULTS

With the performance of the two antenna prototypes presented. this section relates the results to the requirements.

It is found that the antenna designs both show deviations between simulation and measurement. Common for both designs is the fact that the X-band antenna part has the larger deviations which can be attributed to the higher frequency.

Tables 8.1 and 8.2 show a comparison of the measured and simulated performance for both antennas. (On the next page)

The Cross antenna prototype (Table 8.1) does not satisfy the requirements. The SepAp antenna prototype (Table 8.2) satisfies the set requirements with the exception of a frequency offset of 0.2 GHz in the X-band and 60 MHz in the S-band.

The inferior performance of the Cross antenna prototype could be caused by different effects. In Chapter 10 different theories explaining the significant performance differences between the simulation and measured results are presented. The problem is most likely caused by the patch antenna feeding probe choice presented in Section 7.2.

With the measured performance of the two antenna prototypes presented and evaluated relative to the requirements specified in Chapter 4, the prototype measurement champaign is concluded. The next chapter presents simulated results for the effect of mounting the antenna designs on a satellite structures.

Table 8.1: Cross prototype antenna performance compared to the antenna requirements.

Requirement	Band	Requirement	Simulated	Measured
-10 dB impedance	S-Band	1.97 to 2.03 GHz	2.01 to 2.95 GHz	2.01 to 2.13 GHz
bandwidth	X-Band	8.0 to 8.5 GHz	6.75 to 9.15 GHz	≥ -6.94 dB
Gain bandwidth	S-Band	1.97 to 2.03 GHz	2.03 to 2.08 GHz	2.04 to 2.07 GHz
≥ 6 dB and ≥ 12 dB	X-Band	8 to 8.5 GHz	7.75 to 8.75 GHz	≤ 10.5 dB
Min. gain (in 60 MHz	S-band	≥ 6 dB	5.75 dB	5.25 dB
and 0.5 GHz range)	X-band	≥ 12 dB	12.1 dB	7.9 dB
HPBW	S-Band	$\pm$ 20°	84°	81°
	X-Band	$\pm$ 10°	$\pm$ 11°	$\pm$ 10°
Cross coupling	S-Band	≤ -25 dB	≤ -25 dB	≤ -38 dB
	X-Band	≤ -25 dB	≤ -31 dB	≤ -25 dB
Port impedance	S-band	50 Ω	-	-
	X-band	50 Ω	-	-
Antenna dimensions	-	100 by 100 mm	82 by 82 mm	81 by 81.5 mm
Antenna height	-	≤ 7 mm	3.947 mm	4.00 mm

Table 8.2: SepAp prototype antenna performance compared to the antenna requirements.

Requirement	Band	Requirement	Simulated	Measured
-10 dB impedance	S-Band	1.97 to 2.03 GHz	1.91 to 2.07 GHz	1.94 to 2.12 GHz
bandwidth	X-Band	8.0 to 8.5 GHz	7.7 to 8.4 GHz	8.1 to 8.8 GHz
Gain bandwidth	S-Band	1.97 to 2.03 GHz	1.97 to 2.03 GHz	2.00 to 2.12 GHz
(≥ 6 dB and ≥ 12 dB)	X-Band	8 to 8.5 GHz	8.1 to 8.5 GHz	8.2 to 9.0 GHz
Min. gain (in 60 MHz	S-band	≥ 6 dB	7.1 dB	6 dB
and 0.5 GHz range)	X-band	≥ 12 dB	11.8 dB	12.1 dB
HPBW	S-Band	$\pm$ 20°	71°	69°
	X-Band	$\pm$ 10°	$\pm$ 20°	$\pm$ 20°
Cross coupling	S-Band	≤ -25 dB	≤ -40 dB	≤ -40 dB
	X-Band	≤ -25 dB	≤ -40 dB	≤ -40 dB
Port impedance	S-band	50 Ω	-	-
	X-band	50 Ω	-	-
Antenna dimensions	-	100 by 100 mm	82 by 82 mm	82 by 82 mm
Antenna height	-	≤ 7 mm	5.732 mm	5.65 mm

9 SATELLITE INSTALLATION

As mentioned in Chapter 4 the antenna should fit on a 1 U nano-satellite structure. To shield the antenna from the rest of the satellite and mount the antenna to the satellite structure with sufficient structural stability a mounting solution must be developed. The development of a proper mounting solution is outside the scope of this project, instead this chapter investigates the effect of adding a metal box around the antennas as a way of modelling mounting. This chapter is only based on simulations.

First, the metal box is added to a 3D model of the Cross antenna presented in Section 7.3. Secondly, the box is added to a 3D model of the SepAp antenna presented in Section 7.4.

9.1 CROSS ANTENNA

Figure 9.1a shows a CST model of the Cross antenna in a metal box. The metal box is directly touching the bottom ground layer of the antenna and the metal screws. The box has an inner height of 6 mm such that the side of the box extends $\approx$ 2 mm beyond the topmost layer of the antenna. Thus the metal side also extends beyond the screw head hight.

Figure 9.1b shows a model of the antenna mounted on the side of a 2 U nano-satellite box. Simulations are run without the 2 U nano-satellite box.

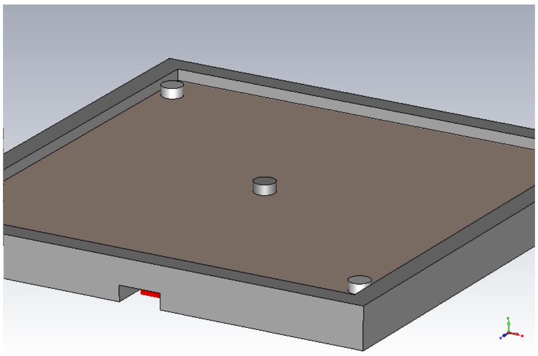

(a) CST Model of the Cross prototype antenna in a metal box.

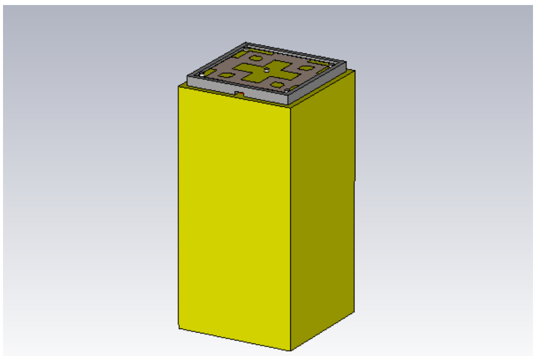

(b) CST Model of the Cross prototype antenna installed on a box the size of a 2 U satellite.

Figure 9.1: CST models of the antenna design in a metal box and on a satellite model.

Figures 9.2 and 9.3 show a comparison of the antenna performance with and without the box. The two plots show the realized RHCP gain in the S-band and X-band respectively.

In the S-band it is observed that adding the box has overall improved the gain characteristics antenna.

In the X-band, it is observed that adding the box causes the antenna to have a slightly higher realized RHCP gain at the lower frequency range at the cost of a lower cut-off frequency. The lowered cutoff frequency causes the frequencies $\geq$ 8.4 GHz to have lower realized RHCP gain. The antenna however still satisfies the gain requirement since the antenna achieves a realized RHCP gain of 12.2 dB at 8.50 GHz.

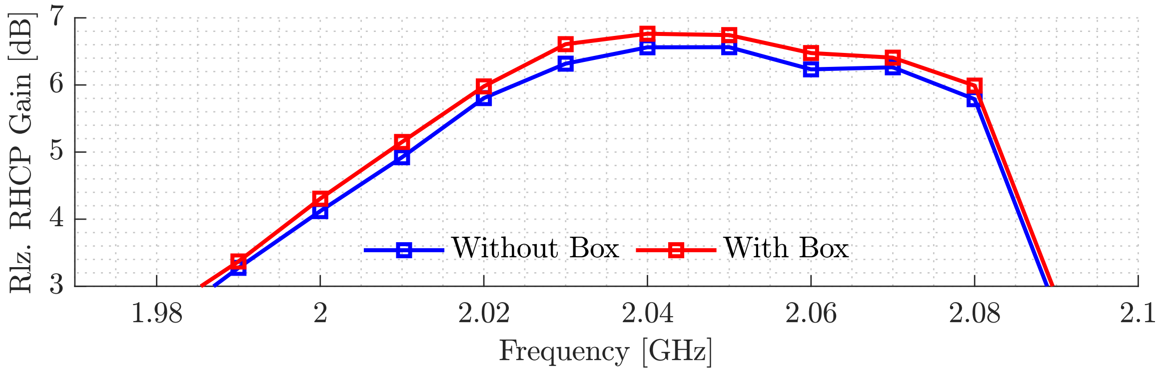

Figure 9.2: Simulated S-band broadside realized RHCP gain of the prototype antenna, with and without the ground box.

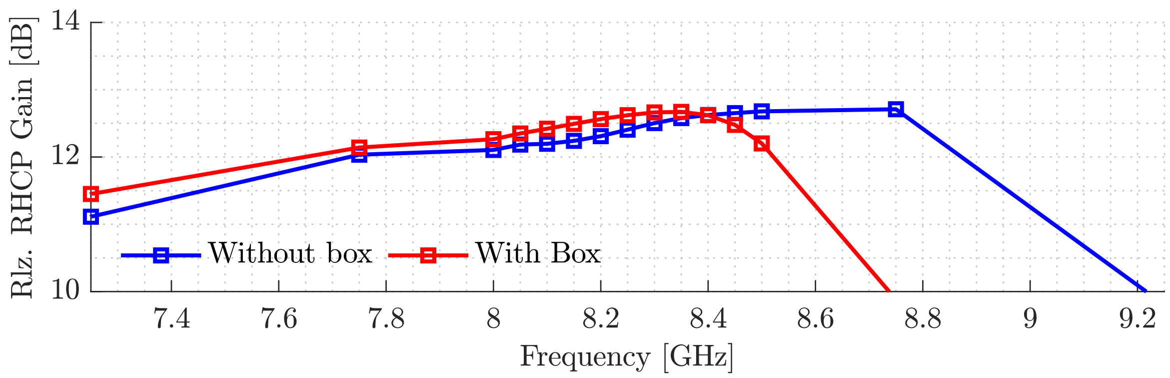

Figure 9.3: Simulated X-band broadside realized RHCP gain of the prototype antenna, with and without the ground box.

Figure 9.4 shows the $\phi = 90°$ slice of the X-band radiation pattern at 8.25 GHz, for the antenna with and without the box. The main-lobe is slightly increased by introducing the box.

Figure 9.5 shows the $\phi = 90°$ slice of the S-band radiation pattern at 2.0 GHz, for the antenna with and without the box. The box increases the antenna gain in the broadside direction by narrowing the beam width.

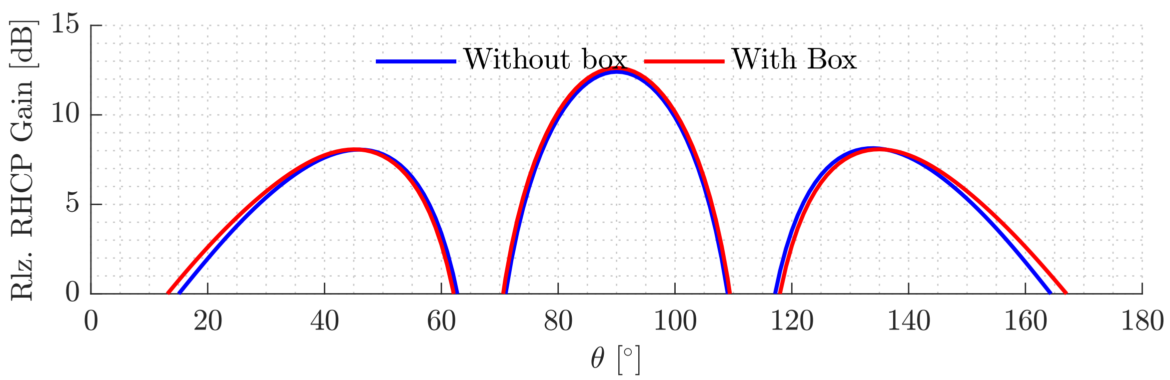

Figure 9.4: $\phi = 90°$ slice of the X-band realized RHCP gain pattern at 8.25 GHz.

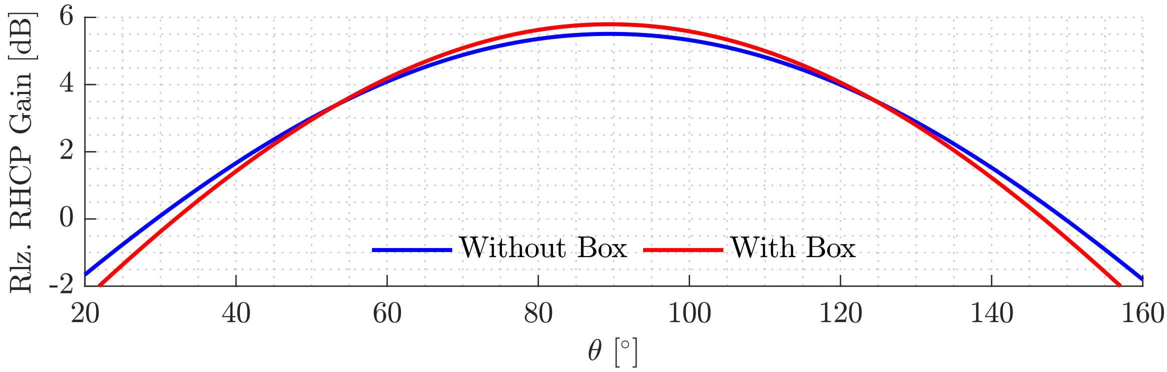

Figure 9.5: $\phi = 90°$ slice of the S-band realized RHCP gain pattern at 2.0 GHz.

9.2 SEPAP ANTENNA

Figure 9.6a shows a CST model of the SepAp prototype antenna in a metal box. The metal box is directly touching the bottom ground layer of the antenna and the metal screws. The box has an inner height of 7.8 mm. Thus the metal box of the SepAp prototype is slightly taller than the box of the Cross prototype, this is to compensate for the taller height of the SepAp prototype antenna. The box extends approximately 2 mm above the topmost layer of the antenna.

Figure 9.6b shows a model of the antenna mounted on the side of a 2 U nano-satellite box. Simulations are run without the 2 U nano-satellite box.

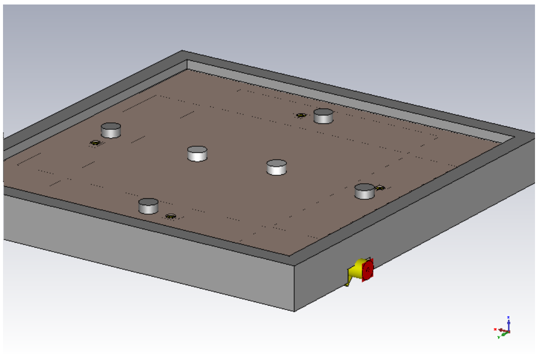

(a) CST Model of the SepAp prototype antenna in a metal box.

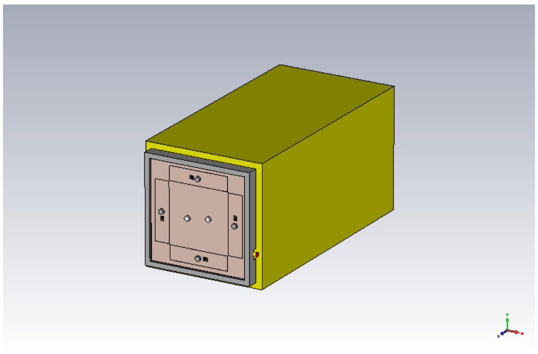

(b) CST Model of the SepAp prototype antenna installted on a box the size of a 2U satellite.

Figure 9.6: CST models of the antenna design in a metal box and on a satellite model.

Figure 9.7 shows the X-band realized RHCP gain of the SepAp antenna prototype with and without the box. The box has slightly lowered the overall gain performance of the antenna.

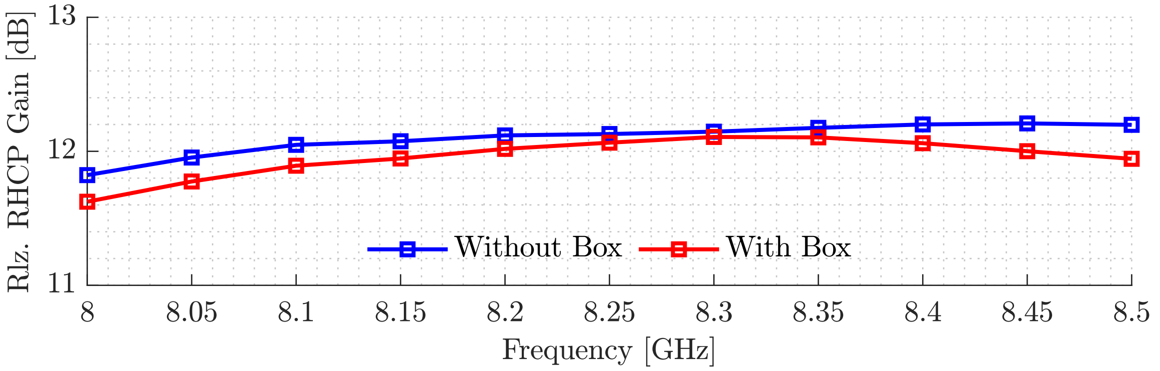

Figure 9.7: Simulated broadside realized RHCP gain of SepAp prototype antenna.

Figure 9.8 shows the S-band realized RHCP gain of the SepAp antenna prototype with and without the box. The box has greatly reduced the gain of the antenna, most significantly at the lower end of the frequency range.

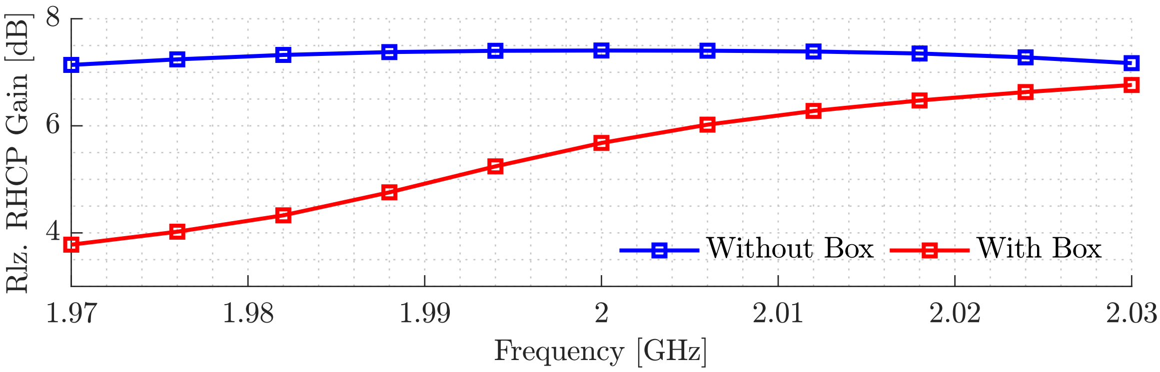

Figure 9.8: Simulated broadside realized RHCP gain of SepAp prototype antenna.

Figure 9.9 shows the S-band realized RHCP gain pattern slices of the SepAp antenna at 1.97 GHz. The maximum gain of the antenna with the box is lower and tilted.

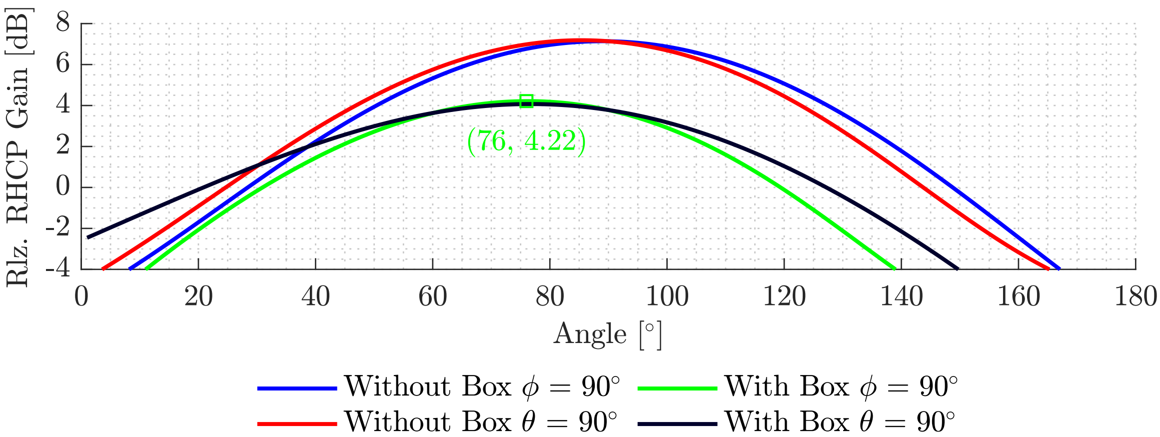

Figure 9.9: $\phi = 90°$ and $\theta = 90°$ slices of the realized RHCP gain pattern of the SepAp antenna at 1.97 GHz.

9.3 CONCLUSION

The grounded box around the antenna does have an effect on the performance on the antennas.

When the metal box is added to the Cross antenna it results in a lowered cutoff frequency of the X-band gain characteristics. For the SepAp antenna the ground box mostly impacts the S-band performance, causing a reduced S-band realized gain.

As expected the metal box effects the outer antenna elements the most, as they are physically closer to the box.

If the proposed antenna designs are to be integrated into a satellite structure, more detailed simulation which investigates the effect of adding metal around the antenna structure is necessary. It is expected that the antenna design must be altered to compensate for are the effect surrounding metals.

10 DISCUSSION

The purpose of this thesis is to propose tested dual S- and X-band nano-satellite antenna designs that comply with the requirements stated in Chapter 4. With antenna performance requirements and a limited available volume, the problem becomes finding a good compromise between volume dedicated to either S-band or X-band, or alternatively finding methods of sharing the volume without sacrificing isolation.

This chapter evaluates some of the choices made throughout this thesis, gives suggestions for further improvements or alternate technologies, and topics for future studies.

Initially, the measured performance of the two antenna prototypes is addressed, and suggestions as to why the Cross antenna prototype deviates from simulations and displays reduced gain and narrower gain bandwidth.

Measurement
Two designs referred to as Cross and SepAp are presented in Chapters 5 and 6 respectively. The prototypes are fabricated and assembled out of single-layer PCBs and tested through a measurement campaign covered in Chapter 8. The antenna measurement champaign shows some differences between the simulated and measured performance. The SepAp antenna prototype is found to satisfy the requirement, however with a 200 MHz frequency offset in the X-band and 60 MHz frequency offset in the S-band. The Cross design shows performance similar to simulations in the S-band, but inferior performance in the X-band and does therefore not satisfy the requirements.

Fabrication and assembly
The material Rogers RT5870 is chosen for both antenna designs. This decision was made based its low loss tangent, relative permittivity of $\epsilon_r = 2.33$, and a presumed availability. During the thesis it is found to be unavailable and the solution is to use the substrate Rogers RT5880 instead. This substrate should yield similar performance since the difference in dielectric constant is only 0.08.

There are two major disadvantages to choosing this substrate for these designs: The flexibility of the substrate and the fact that there is no matching pre-preg available at the time of writing.

Due to the lack of matching pre-preg, it is not possible to fabricate the designs as single multi-layer PCBs. It is instead chosen to realize the multi-layer designs by manually assembling single-layer PCBs together with screws. This choice introduces some imperfections. There is potential for misalignment through tolerances during drilling of screw holes individually for each layer. It also allows for potential air gaps between the layers. The risk of having air gaps is further increased by the flexible nature of the substrate material. Air gaps change the effective dielectric constant and can cause a loss in performance.

The slim substrate layers used in the feeding network are fragile due to the flexibility of the substrate. With SMA connectors soldered to the edge of the slim substrates, the strain put on the substrate when tightening SMA cables to the prototype can break the substrate. During measurements, one of the prototypes broke and had to be fixed by soldering wire along the broken stripline.

In an attempt to compensate for the flexible substrate material, a wooden plate is added below the ground layer of the prototypes. This wooden plate improves the stability of the antennas and doubles as a mounting fixture. With a second iteration of the Cross prototype, an additional wood plate is added on the bottom to give additional support to the connector. This additional wooden plate improves the structural integrity of the prototype greatly. The wooden plate is however measured to introduce an approximately 0.5 dB loss of realized RHCP gain in the S-band and the effect is unknown at the X-band.

Both of the proposed antenna designs uses multi-layer VIAs as feeding probes. Since the antenna prototypes are assembled by manually screwing single-layer PCBs together to realize the multi-layer designs such multi-layer VIAs are not possible to fabricate. Therefore two different methods are used to realize the feeding probes. Section 7.2 describes how the feeding probes are realized. For SepAp antenna design, the feeding probes are realized by having the manufacturer drill holes in the printed circuit board and then manually soldering metal wires to the board. For the Cross design, the feeding probes are realized by having single-layer VIAs terminated in copper pads. The copper pads of the different layers must be pressed tightly together to connect the feeding probe. The results in Section 8.3, shows that the SepAp antenna design with the manually soldered wires yields better results. This might indicate that the manually soldered feeding probes are a better design choice. It is expected that the solder pads are not pressed properly together in the prototype because of the flexible nature of the substrate material or misalignment. To prove this theory additional measurements could be conducted with a modified Cross prototype using an alternative feeding probe realization.

Both of the two antenna prototypes are designed to be 82 by 82 mm. The fabricated Cross prototype is however only 81.0 by 81.5 mm. By inspection with a calliper, it is concluded that the patches of the antennas are the correct size. Thus it is assumed that the PCBs was imprecisely cut from the panel during fabrication. This is the case for all the layers of the fabricated Cross prototypes. This is not expected to significantly affect the antenna performance.

S-band design

During the design phase, the primary challenge of the S-band design is to achieve a sufficient impedance bandwidth. This is in agreement with the theory showing that a width of at least 40 mm and substrate height 4.725 mm is necessary to provide the required bandwidth for a standard patch antenna (Section 2.7.3). Due to the limited substrate height and surface area, sufficient bandwidth cannot be achieved by simply increasing the width of the patch and alternate methods are therefore used.

The Cross design utilizes a stacked antenna structure where the tuning of the patches and coupling between them is vital to the performance. As a consequence of choosing the stacked structure, the available substrate height for each patch antenna layer in the stack is halved, reducing the bandwidth of each element. This, in turn, makes the tuning of each element less resistant to fabrication and component tolerances such as shifts in dielectric constants, due to their narrow bandwidth.

The SepAp design utilizes both a tall substrate which limits the available height for the mounting fixture design and feeding network, together with the fact that bandwidth increases as ground plane is removed, which is the case when the S-band patches are placed along the edge of the 1 U face. This makes the S-band performance vulnerable to adjacent metals, the design of the mounting fixture, and positioning on the nano satellite. The vulnerability to adjacent structures is discovered in Section 9.2 where the performance suffers as metal is placed along the edge of the antenna.

An evident method of increasing the bandwidth which was not considered during the thesis can be derived from Section 2.9 and Appendix A where circular polarization is achieved using a single feed into a structure supporting two orthogonal resonant modes at two frequencies, one above and one below the center frequency. A slight shift in resonant frequency between the two orthogonal mods creates a desired 90° relative phase between the two modes required for circular polarization. In Appendix A this approach shows significantly improved impedance bandwidth at the cost of axial ratio bandwidth. As both the Cross and SepAp designs use orthogonal patches tuned to the same frequency and fed 90° out of phase, the impedance bandwidth could be improved by detuning them slightly and reducing the phase shift in the feeding network. This would allow for a more symmetric feed network design. To slightly improve the axial ratio the linear S-band patches, they could be made elliptically polarized if the allocated area allows it, also improving the RHCP gain.

The bandwidth could also be improved by introducing additional resonances either in the feeding network or by cutting slots in the antenna elements, as covered in Chapter 3.

X-band design
The X-band design does not present the same challenges in regards to impedance bandwidth, as the substrate is electrically four times as tall. The main challenge is however to achieve sufficient RHCP gain, as the adjacent S-band elements and electrically larger ground size are observed to affect the radiation pattern of the X-band elements, decreasing the gain in the broadside direction. In the Cross design, copper guides on the corners of the antenna are used to provide a more symmetrical propagation environment and limit the effective ground plane size. The guides together with a stacked patch design are simulated to provide the required performance with a margin for losses elsewhere. In the SepAp design, the substrate height of the X-band elements is reduced and the distance to the S-band elements is swept to find an optimized point. The parameter sweep finds a set of values which provides just enough performance to fulfil the requirements.

In the SepAp design, the S-band patches have a width comparable to the theoretical resonant length of an X-band patch. An idea for a future improvement could therefore be to utilize the width of the S-band patches as X-band patches, and thereby increase the gain.

Future studies
To investigate the cause of the inferior performance of the Cross design, simulations incorporating the added wood plates and measurements with alternative feeding probe realizations should be made. Topics for further improvements to the designs could include integrating K-band end-firing antenna elements into the stack-up for inter satellite communications, metasurface-based designs allowing full reuse of the limited surface area as done in [27], or coupled-resonator feeding networks, as introduced in Chapter 3, to reduce the total height of the antenna.

11 CONCLUSION

The focus of this thesis is defined in the introduction (Chapter 1) as:

Design of dual-band S- and X-band antennas for nano-satellites

It is chosen to focus on designs for a 1 U nano-satellite face using microstrip patch antennas. The theory (Chapter 2) covers definitions for commonly used antenna terms and performance metrics. The later parts of the chapter focuses on microstrip patch antenna design.

Chapters 5 and 6 present two different antenna design proposals. The two antennas are designed from different structure topologies. One antenna called SepAp is designed using an array of four X-band patch antenna surrounded by four narrow width S-band patch antennas. The other antenna design is called Cross because it is designed with a cross-shaped S-band patch antenna surrounded by an array of four X-band patch antennas.

Prototypes antenna are made for both of the two designed antennas. For the two designs, the feeding probe is realized differently. For the SepAp prototype, wires are manually soldered to connect the feeding to the antenna elements. For the Cross prototype, PCB VIAs terminated in copper pads are used to realize the feeding probe, by pressing the copper pads together.

A measurement campaign is presented in Chapter 8. The simulated and measured results of both antenna prototypes are presented in Section 8.3. The measurement results show some variation compared to the simulated antenna performance. The Cross antenna prototype shows significantly worse performance comparing when measurement to simulation. The Cross antenna prototype does not satisfy the requirements. The SepAp antenna prototype however shows better measurement results and the antenna satisfies all the requirements except for a small frequency offset of 0.2 GHz for the X-band antenna.

The measurement of the SepAp antenna prototype shows a realized RHCP gain of ≥ 6.0 dB in the S-band frequency range 2.00 to 2.12 GHz and a realized RHCP gain of ≥ 12.0 dB in the X-band frequency range 8.2 to 9.05 GHz. The impedance bandwidth of the antenna is measured to satisfy the set requirements as well, since it is measured to exceed the desired frequency range. Furthermore the antenna shows to have a cross-coupling lower than -40 dB in the full frequency range of interest.

The inferior performance of the Cross antenna is discussed in Chapter 10. However, the problem is most likely caused by the patch antenna feeding probe choice presented in Section 7.2. To prove this theory additional measurements could be conducted with a modified antenna prototype using another feeding probe realization.

With the good measurement results for the SepAp antenna prototype, the thesis achieves its objective of designing a dual-band S- and X-band nano-satellite antenna which satisfies the set of requirements.

BIBLIOGRAPHY

[1] Alen, “A basic guide to nanosatellites,” Website. [Online]. Available: https://alen.space/basic-guide-nanosatellites/

[2] M. Birney, “Sky and space global secures commercial contracts for nano-satellite bandwidth,” Website. [Online]. Available: https://www.businessnews.com.au/article/Sky-and-Space-Global-secures-commercial-contracts-for-nano-satellite-bandwidth

[3] Earth Observation Portal, “Gomx-3 (gomspace express-3),” Website. [Online]. Available: https://directory.eoportal.org/web/eoportal/satellite-missions/g/gomx-3

[4] S. Gao, Y. Rahmat-Samii, R. E. Hodges, and X. Yang, “Advanced antennas for small satellites,” *Proceedings of the IEEE*, vol. 106, no. 3, pp. 391–403, March 2018.

[5] A. H. Lokman, P. J. Soh, S. N. Azemi, H. Lago, S. K. Podilchak, S. Chalermwisutkul, M. F. Jamlos, A. A. Al-Hadi, P. Akkaraekthalin, and S. Gao, “A Review of Antennas for Picosatellite Applications,” *International Journal of Antennas and Propagation*, vol. 2017, pp. 1–17, 2017. [Online]. Available: https://www.hindawi.com/journals/ijap/2017/4940656/

[6] “Ieee standard test procedures for antennas,” *ANSI/IEEE Std 149-1979*, pp. 0_1–, 1979.

[7] D. Pozar, *Microwave Engineering, 4th Edition.* Wiley, 2011.

[8] C. A. Balanis, *Antenna Theory: Analysis and Design*, 4th ed. Wiley, 2016.

[9] T. Milligan, *Modern Antenna Design*, ser. Wiley - IEEE. Wiley, 2005.

[10] J. R. James, P. S. Hall, and C. Wood, *MICROSTRIP ANTENNA THEORY AND DESIGN: Electromagnetic wave series 12*, ser. IEE Electromagnetic wave series. Peter Peregrinus Ltd, 1981.

[11] R. J. Mailloux, *Phased Array Antenna Handbook.* Artech house, 1993.

[12] C. Mao, S. Gao, Y. Wang, Q. Chu, and X. Yang, “Dual-band circularly polarized shared-aperture array for c-/ x-band satellite communications,” *IEEE Transactions on Antennas and Propagation*, vol. 65, no. 10, pp. 5171–5178, Oct 2017.

[13] X. Zhang and L. Zhu, “High-gain circularly polarized microstrip patch antenna with loading of shorting pins,” *IEEE Transactions on Antennas and Propagation*, vol. 64, no. 6, pp. 2172–2178, June 2016.

[14] C. X. Mao, S. Gao, Z. P. Wang, Y. Wang, F. Qin, B. Sanz-Izquierdo, and Q. X. Chu, “Integrated filtering-antenna with controllable frequency bandwidth,” in *2015 9th European Conference on Antennas and Propagation (EuCAP)*, April 2015, pp. 1–4.

[15] Y. Zhang, X. Y. Zhang, L. Ye, and Y. Pan, “Dual-band base station array using filtering antenna elements for mutual coupling suppression,” *IEEE Transactions on Antennas and Propagation*, vol. 64, no. 8, pp. 3423–3430, Aug 2016.

[16] A. Nascetti, E. Pittella, P. Teofilatto, and S. Pisa, “High-gain s-band patch antenna

system for earth-observation cubesat satellites," *IEEE Antennas and Wireless Propagation Letters*, vol. 14, pp. 434–437, 2015.

[17] P. Mathur and G. Kumar, "Dual-frequency microstrip antenna at s and x bands with higher-order mode suppression technique," *IET Microwaves, Antennas Propagation*, vol. 12, no. 4, pp. 583–587, 2018.

[18] C. Salvador, L. Borselli, A. Falciani, and S. Maci, "Dual frequency planar antenna at s and x bands," *Electronics Letters*, vol. 31, no. 20, pp. 1706–1707, Sep. 1995.

[19] A. I. Sandhu, E. Arnieri, G. Amendola, L. Boccia, E. Meniconi, and V. Ziegler, "Radiating elements for shared aperture tx/rx phased arrays at k/ka band," *IEEE Transactions on Antennas and Propagation*, vol. 64, no. 6, pp. 2270–2282, June 2016.

[20] Y. Yao, S. Liao, J. Wang, K. Xue, E. A. Balfour, and Y. Luo, "A new patch antenna designed for cubesat: Dual feed, ls dual-band stacked, and circularly polarized." *IEEE Antennas and Propagation Magazine*, vol. 58, no. 3, pp. 16–21, June 2016.

[21] GomSpace, "Nanocom ant2000," Website. [Online]. Available: https://gomspace.com/shop/subsystems/communication-(1)/nanocom-ant2000.aspx

[22] Endurosat, "X-band 4 element patch antenna array," Website. [Online]. Available: https://www.endurosat.com/products/cubesat-x-band-2x2-patch-array/

[23] Rogers corp., *RT/duroid® 5870 /5880 High Frequency Laminates*, 2018. [Online]. Available: https://www.rogerscorp.com/documents/606/acs/RT-duroid-5870-5880-Data-Sheet.pdf

[24] P. Mathur and G. Kumar, "Dual-frequency microstrip antenna at s and x bands with higher-order mode suppression technique," *IET Microwaves, Antennas Propagation*, vol. 12, no. 4, pp. 583–587, 2018.

[25] Y. Xu, S. Gong, and Y. Guan, "Coaxially fed microstrip antenna for harmonic suppression," *Electronics Letters*, vol. 48, no. 15, pp. 895–896, July 2012.

[26] Chengdu AINFO Inc., "A-info," Website. [Online]. Available: http://www.ainfoinc.com

[27] T. Li and Z. N. Chen, "Metasurface-based shared-aperture 5gS-/K-band antenna using characteristic mode analysis," *IEEE Transactions on Antennas and Propagation*, vol. 66, no. 12, pp. 6742–6750, Dec 2018.

A ACHIEVING CIRCULAR POLARISATION WITH AN X-BAND PATCH ANTENNA

In this appendix four different methods of achieving circular polarisation with a single patch antenna element is investigated. The four methods are:

- Dual feeding the antenna element
- Feeding the antenna at the corner
- Trimming two opposite corners of the antenna patch
- Cutting a rectangular sloth on the patch antenna element

The performance of the different methods is investigated by designing a circularly polarized X-band patch antenna using each of the four methods.

ANTENNA PARAMETERS

Table A.1 shows the dimensions of the four antennas. Figure A.1 and Figure A.2 show the CST models of the four designed antennas.

Table A.1: The dimentions of the four designed patch antennas.

Antenna Type	Corner Trim	Slotted Patch	Dual Feed	Corner feed
Substrate Height	1.524			
Feed Substrate Height	0.305			
Feed Line Height	0.035			
Substrate type	RO4003C			
Feed line Width	0.7			
Feed Line Length	20			
Board Size	95			
Patch Length	8.95	8.2	8.6	8.15
Patch Width	8.96	8.2	8.6	9.05
Feeding point (Length)	2.00	1.3	1.5	1.05
Feeding point (Width)	0.50	-	-	1.85
Feed Pin radius	0.35			
Ground Cut Radius	0.9			
Corner Trim	2.65	-	-	-
Patch cut Width	-	1.40	-	-
Patch cut Length	-	4.90	-	-
Patch cut rotation	-	50°	-	-

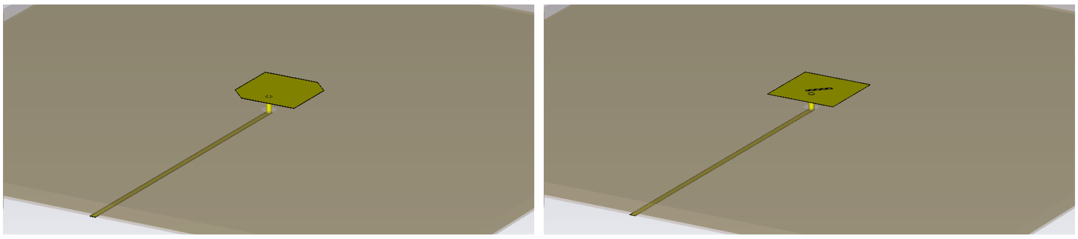

(a) Trimmed corner patch antenna. (b) Slotted patch antenna.

Figure A.1: Two different methods of achiving circular polarizateion.

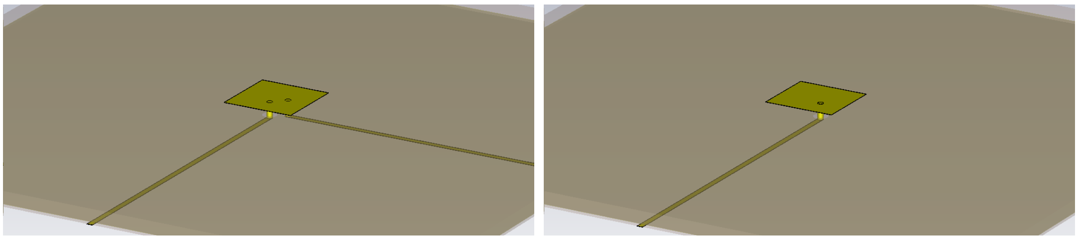

(a) Dual feed patch antenna. (b) Corner feed patch antenna.

Figure A.2: Two different methods of achiving circular polarizateion.

SIMULATION RESULTS

Figures A.3 and A.4 show the simulated radiation patterns of the four antennas. The four methods result in similarly shaped radiation patterns and all methods yields total efficiencies of around 90 %.

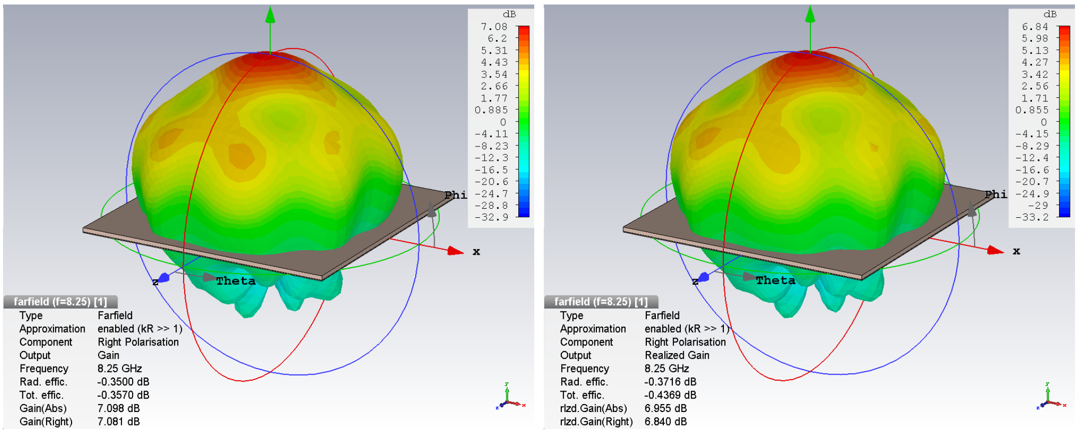

(a) Simulated radiation pattern fot the corner trimmed patch antenna. (b) Simulated radiation pattern fot the slotted patch antenna.

Figure A.3: Simulated radiation patterns.

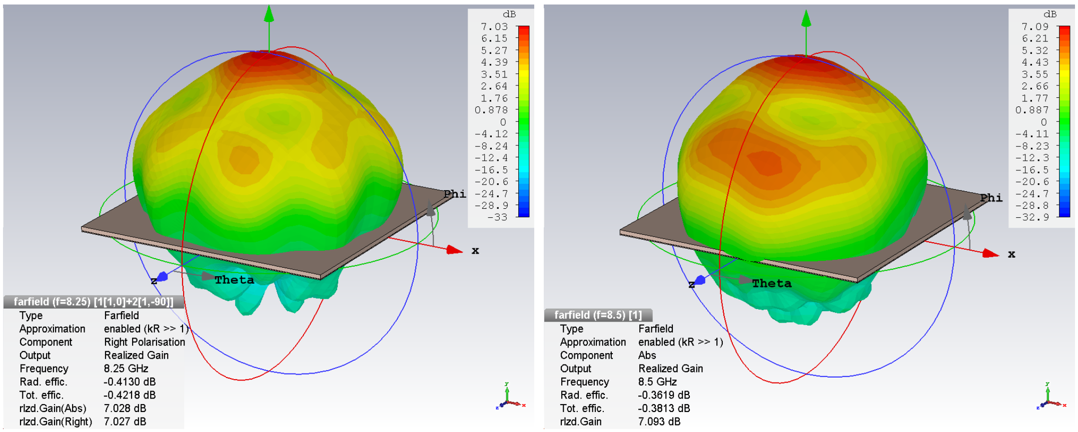

(a) Simulated radiation pattern fot the dual feed patch antenna.

(b) Simulated radiation pattern fot the corner feed patch antenna.

Figure A.4: Simulated radiation patterns.

Figure A.5 shows the S-parameters of the four antennas. The dual feed patch has a sharp impedance match. The remaining three methods provide wider bands, with the three methods giving a -10 dB impedance match covering more than the full 8.0 to 8.5 GHz frequency range. This wideband characteristics is achieved because the designs function as two resonators tuned to different frequencies.

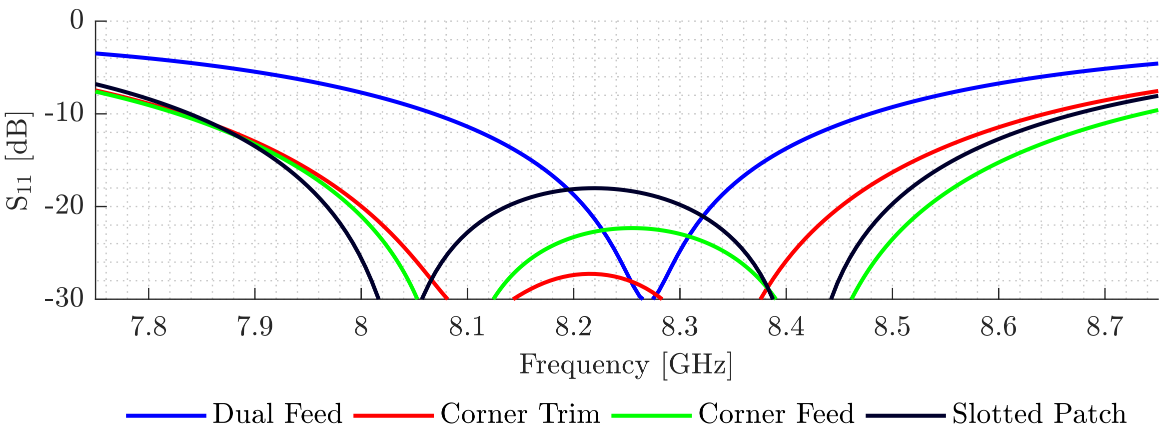

Figure A.5: Simulated S_{11} parameter of the four patch antennas.

Figure A.6 shows the broadside realized RHCP gain of the four antennas. The performance of the antennas is observed to be similar.

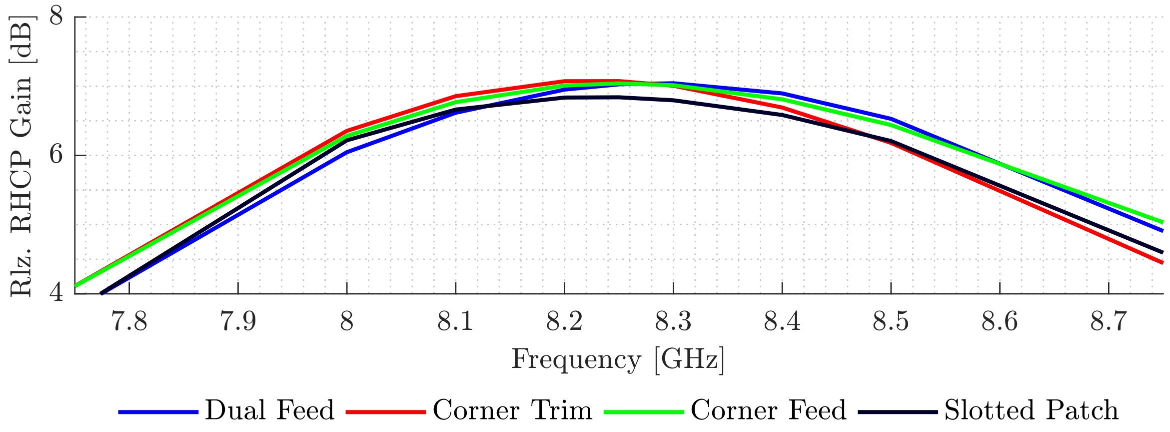

Figure A.6: Simulated broadside realized RHCP gain.

Figure A.7 shows the broadside axial ratio of the four patches. The axial ratio of the dual feed patch is low compared to the other designs. This is caused by the nature of witch the CST software combines the two ports in the simulation, if the power division of the design was made by a microstrip power divider, the axial ratio of the design is expected to follow the curvature of the other designs.

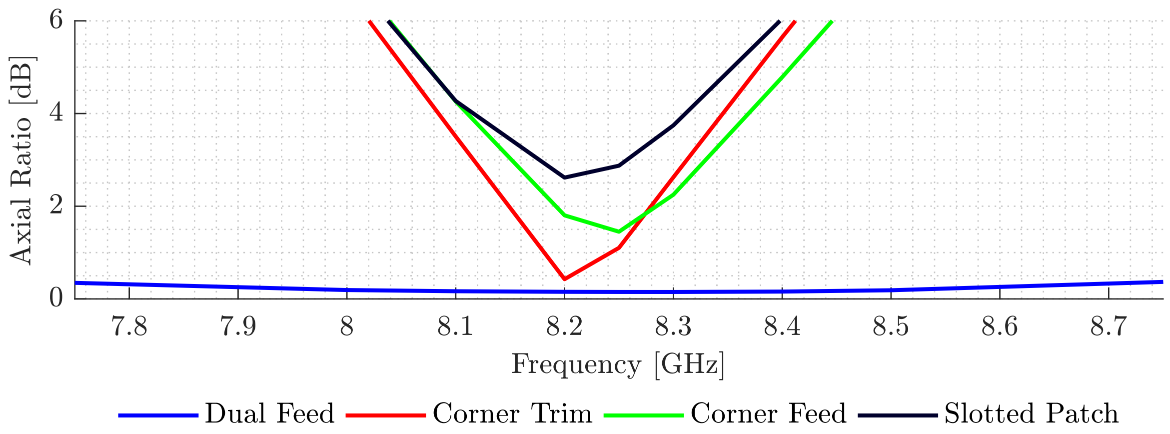

Figure A.7: Simulated broadside axial ratio.

B X-BAND PATCH ANTENNAS WITH DIFFERENT SUBSTRATE HEIGHTS

In this appendix the performance of a square linear polarized patch antenna with different substrate heights is investigated. For this purpose three different patch antennas are used. The three patches have substrate heights: 0.508, 1.524 and 3.048 mm.

The dimensions of the three patch antennas are seen in Table B.1. The CST models of the antennas is seen in Figure B.1.

From Table B.1 it is observed that the feeding point is moved further from the center on the higher substrate designs. The feeding point is moved to match the probe impedance to the patch input impedance.

Table B.1: Dimensions of the three antennas.

Substrate Height	0.508	1.524	3.048
Substrate Height(Feeding side)	0.305		
Feed Line Height	0.035		
Substrate Type	RO4003C		
Board Size	100	95	88
Patch Length	9.15	8.65	8.40
Patch Width	9.15	8.65	8.40
Feeding point (Distance from center)	1.05	1.50	2.75
Feed line Width	0.7		
Feed Pin radius	0.35		
Ground Cut out Radius	0.9		

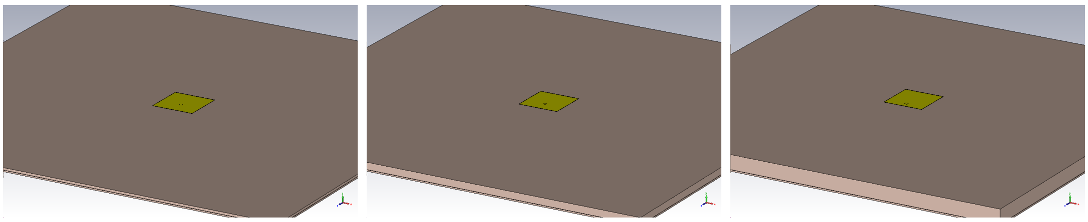

(a) CST model of the designed patch with 0.508 mm of substrate. (b) CST model of the designed patch with 1.524 mm of substrate. (c) CST model of the designed patch with 3.048 mm of substrate.

Figure B.1: CST models of the three designed patch antennas.

SIMULATION RESULTS

Figure B.2 shows the simulated S-parameters of the three antennas. It is seen that higher substrate increases the impedance bandwidth.

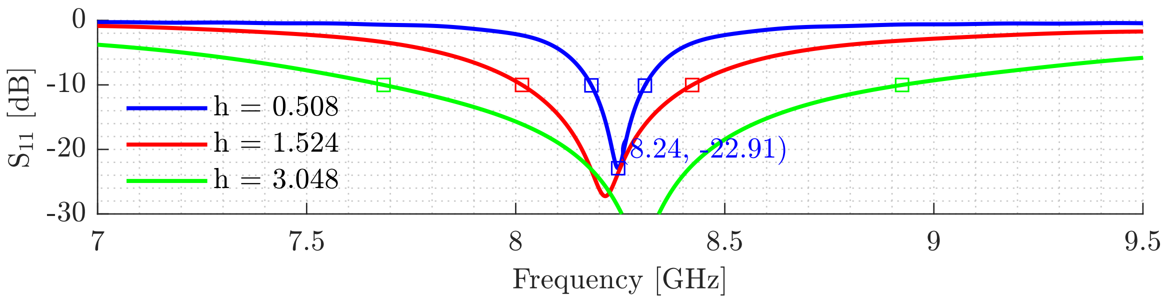

Figure B.2: Simulated S-parameter of the three antennas.

As seen from Figure B.2 the antenna do not seem to be matched to 8.25 GHz. This is because the patch antennas are matched such that they have equal gain at 8.0 GHz and 8.5 GHz, which causes a slight shift in the return loss characteristic. However, all three antenna designs still have a S_{11} below -20 dB.

Figure B.3 shows the radiation pattern of the three antennas. Figure B.4 shows the broadside realized gain of the three antennas.

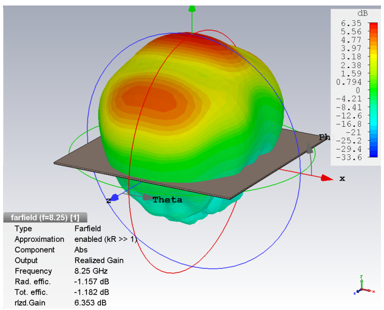

(a) Radiation pattern of the designed patch with 0.508 mm of substrate.

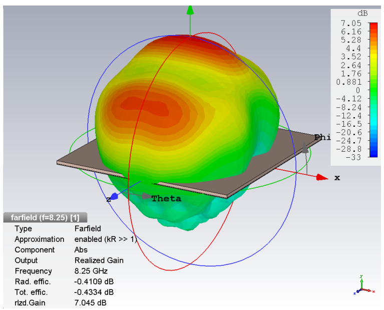

(b) Radiation pattern of the designed patch with 1.524 mm of substrate.

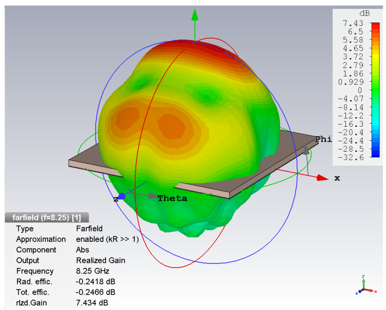

(c) Radiation pattern of the designed patch with 3.048 mm of substrate.

Figure B.3: Radiation pattern of the three designed patch antennas.

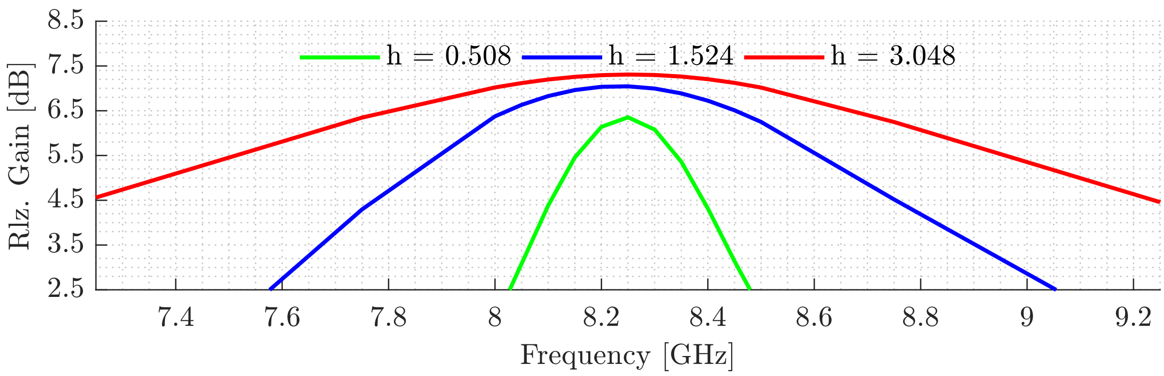

Figure B.4: Simulated broadside realized gain of the three antennas.

Figures B.3 and B.4 show that a higher substrate results in a higher gain and gain bandwidth.

C REDUCING THE WIDTH OF A S-BAND PATCH ANTENNA

In this appendix the effect of reducing the width of an rectangular patch antenna is investigated. A comparison of the impedance bandwidth and the realized antenna gain is conducted and the results are presented.

To investigate the effect of using a non full width rectangular patch antenna an S-band rectangular patch is simulated. The antenna is seen in Figure C.1a. This antenna serves as a reference point for the performance of a full width patch antenna.

For the comparison a reduced width patch antenna is also simulated. The reduced width patch antenna has a width of 16 mm and is tuned to the same frequency. The reduced width patch antenna is seen in Figure C.1b.

Table C.1 shows the dimensions of the two patch antennas.

Table C.1: Dimensions of the two patch antennas.

Name	Reference	Reduced Width
Patch Width	38.45	16
Patch Length	38.45	39.40
Feeding point (Distance from center)	5.20	3.00
Substrate Type	RO4003	
Substrate Height (Under Patch)	1.524	
Substrate Height(Feeding side)	0.305	
Board Size	82	
Copper Height	0.017	
Feed line Width	0.70	
Feed line length	To edge of board	
Feed Pin radius	0.35	
Ground Cut out Radius	0.70	

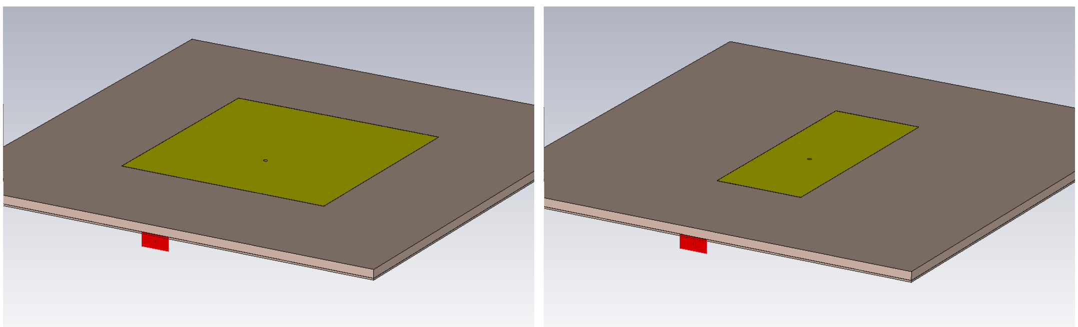

(a) CST model of the full width patch antenna.

(b) CST model of the reduced width patch antenna.

Figure C.1: CST models of the two patch antennas.

SIMULATION RESULTS

Figures C.2a and C.2b show the radiation pattern of the full and reduced width patch antennas respectively. The full width patch antenna has a realized gain of 5.60 dB and the reduced width patch antenna has a realized gain of 4.68 dB.

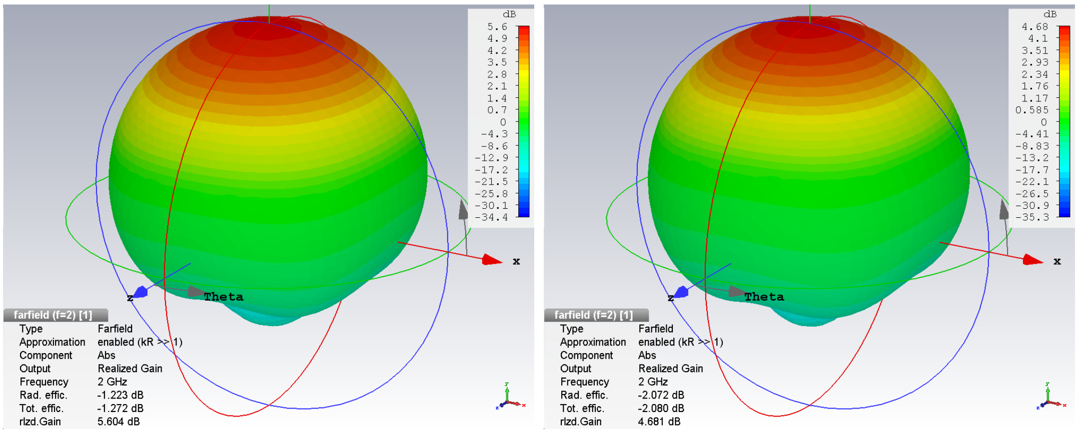

(a) Simulated radiation pattern of the full width patch antenna.

(b) Simulated radiation pattern of the reduced width patch antenna.

Figure C.2: Simmulated radiation pattern of the two patch antennas.

It is seen from the simulation results in Figure C.2 that the full width patch has a higher gain. This is expected since it has a larger physical aperture. The reduction in the patch width has caused a 0.92 dB gain loss.

Figure C.3 shows simulated broadside realized gain of the two S-band patch antennas. As expected the reduced width patch antenna has a lower gain than that of the full width reference. Additionally the 3 dB bandwidth of the full patch is ≈ 67 MHz whilst that of the reduced patch is ≈ 46 MHz

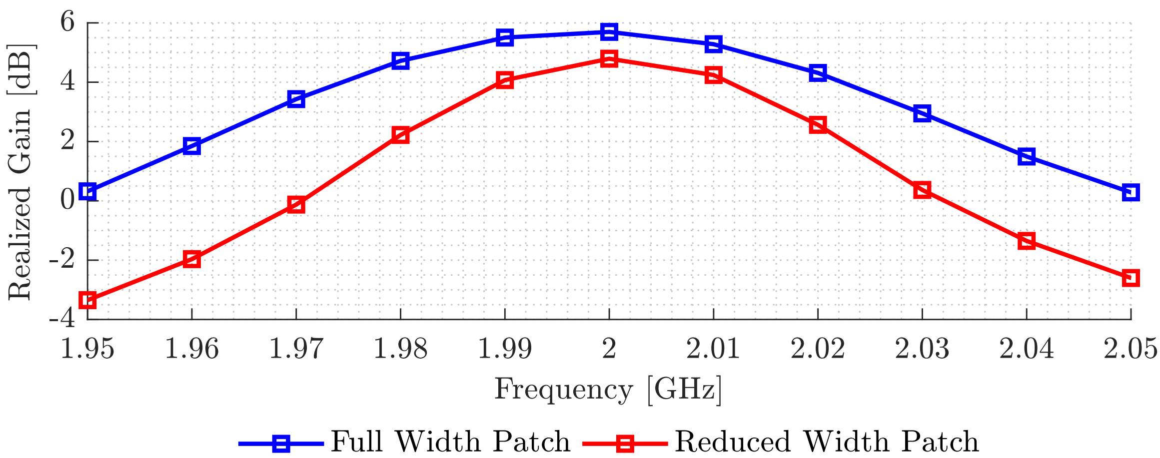

Figure C.3: Simulated broadside realized linear gain of the two patch antennas.

Figure C.4 shows the S-parameters of the two antennas. The impedance bandwidth of the full width patch is 24 MHz and the impedance bandwidth of the reduced width patch antenna is 16 MHz. The reduced width patch has 60 % of the bandwidth at only 42 % of the width.

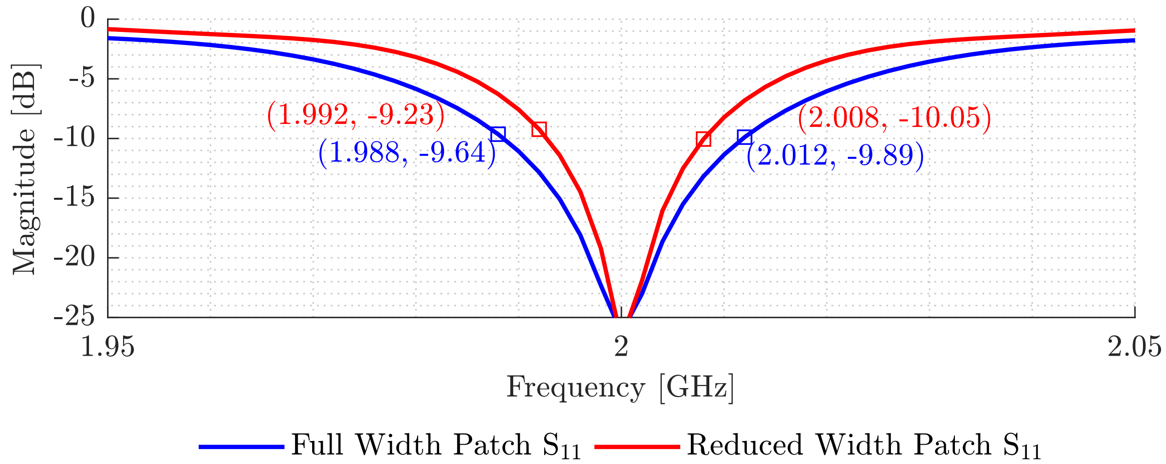

Figure C.4: Simulated S_{11} parameter of the two antennas.

D TRANSMISSION STRIPLINE LOSS

In this appendix the losses of a stripline is investigated. First, soft bends are compared to hard bends. Secondly, the effect of multiple sequential bends is investigated.

Figure D.1a shows the reference Stripline. The line has a width of 0.32 mm and a length of 100 mm, this results in 50 Ω impedance since the line is embedded between two 0.254 mm Rogers RT5870 substrates.

Figures D.1b and D.1c show the soft and hard bends which are introduced to the stripline. All lines have a simulated impedance between 53.03 to 53.04 Ω.

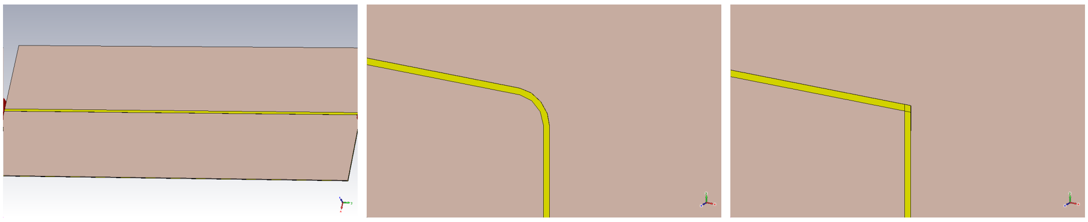

(a) Model of the reference stripline, with top substrate hidden.

(b) Model of the stripline with a soft bend, with top substrate hidden.

(c) Model of the stripline with a hard bend, with top substrate hidden.

Figure D.1: CST models of striplines lines.

Figure D.2 shows a stripline of the same length but with 10 sequential hard bends. The bends are arranged as a square-wave pattern with a step width of 5 mm.

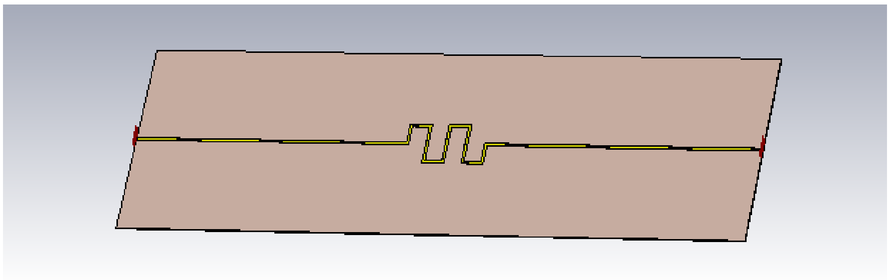

Figure D.2: Model of a stripline with multiple bends, with the top substrate hidden.

Figure D.3 shows the magnitude of the simulated S_{21} parameters of all four striplines. Figure D.4 shows the phase of the simulated S_{21} parameters.

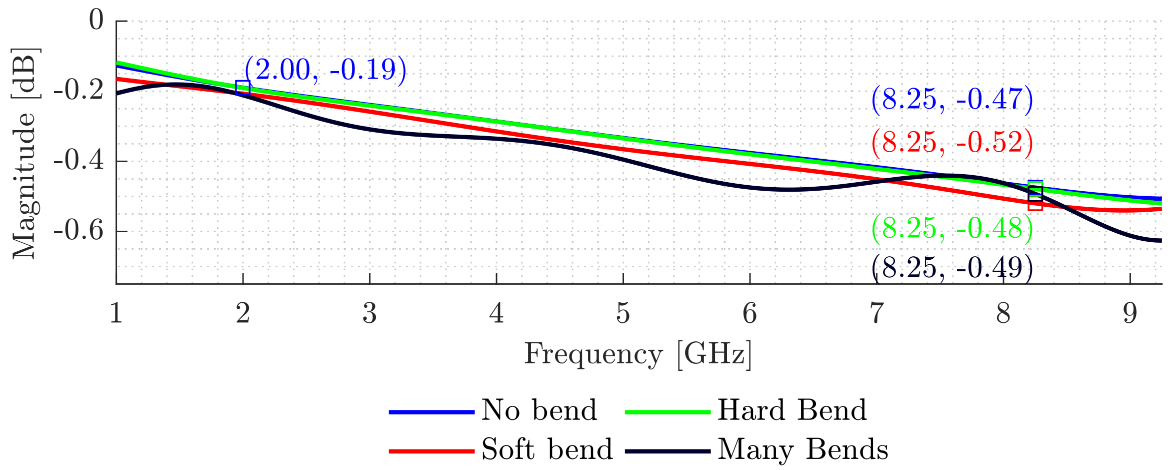

Figure D.3: Simulated S_{21} parameter magnitudes for the different striplines.

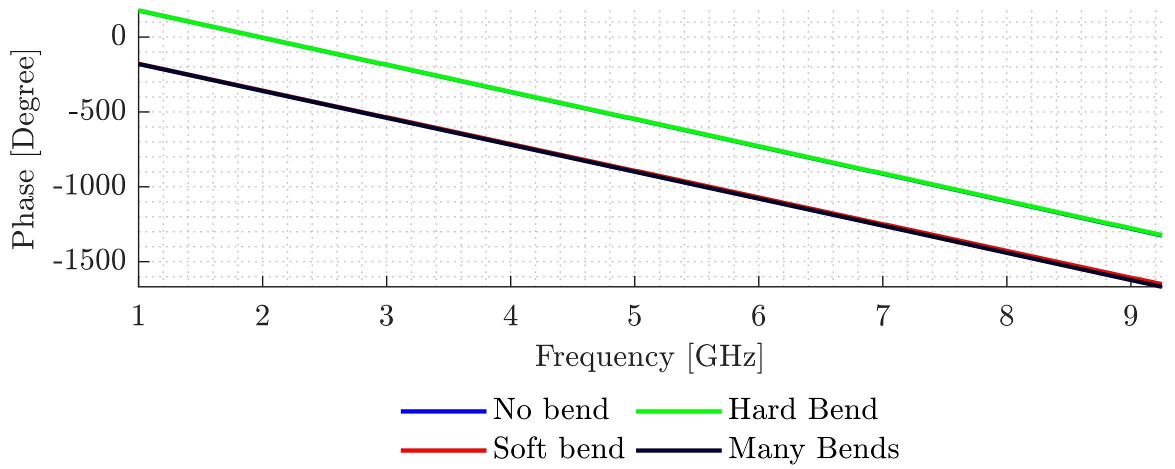

Figure D.4: Simulated S_{21} parameter phases for the different striplines.

CONCLUSION

The simulations show that multiple bends on a stripling might course a loss. With a length of 100 mm and 10 bends, however, no significant loss was observed.

The reference stripline has a loss of 0.19 dB at 2 GHz and 0.47 dB at 8.50 GHz.

E ARRAY INVESTIGATION

The purpose of this appendix is to investigate the array gain when combining four X-band patch antenna elements. It is desired to investigate different types and array combinations.

The following is investigated:

- Linear Patches combined to achieve a linear array gain
- Linear Patches combined to achieve circular polarisation
- Circular patches combined to have a circular gain (With two different array arrangements)

Two patches antennas are designed. One linear polarized patch antenna and one circular polarised. The linearly patch antenna is square. The circularly polarized patch antenna achieves RHCP by trimming the corners of the patch antenna. The dimensions of the two patch antennas is seen in Table E.1.

Table E.1: Dimentions of the two patch antennas.

Patch Polarization	Linear Patch	Circular Patch
Substrate	RO4003C	
Substrate Height (Under Patch)	1.524	
Substrate Height (Feeding side)	0.305	
Copper Height	0.035	
Board Size	95	
Patch Length	8.63	8.95
Patch Width	8.63	8.95
Feeding point Z-axis	1.5	2.0
Feeding point X-axis	-	0.5
Corner Trim	-	2.65
Feed line Width	0.7	
Feed Pin radius	0.35	
Ground Cut out Radius	0.9	
Feed Line length	20	

Figure E.1 shows the two patch antennas. Figure E.1a shows the linearly polarized antenna and Figure E.1b shows the circularly polarized antenna. These two antennas designs is used for the array investigation.

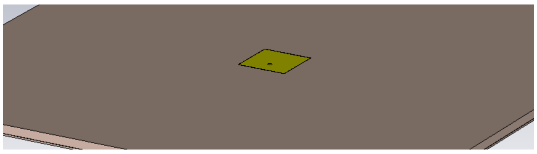

(a) The linearly polarized patch antenna.

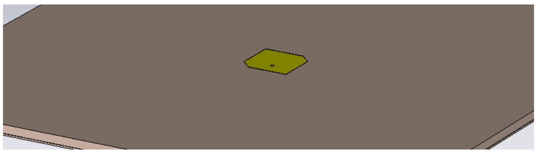

(b) The circularly polarized patch antenna.

Figure E.1: The two patch antennnas.

LINEAR PATCHES COMBINED TO ACHIEVE A LINEAR ARRAY GAIN

The patch antenna seen in Figure E.1a is used in a two-by-two array. The antennas are arranged as seen in Figure E.9a and the two upper patches are feed with a 180° out of phase. The array improves the linear gain of the patch by a theoretical array gain of 6 dB.

With antenna arrays an important design parameter is the distance between the antenna elements.

Figure E.2 shows the broadside realized gain. The plot contains both the simulation results for a single antenna port and the combined array. It is seen that the combined antenna is consistently approximately 6 dB higher than that of an individual antenna. The gain of the individual antenna vary with the antenna separation. It is observed from the simulations that a center to center antenna distance of approximately $0.7 \cdot \lambda = 25.45\,\mathrm{mm}$ results in the highest realized gain.

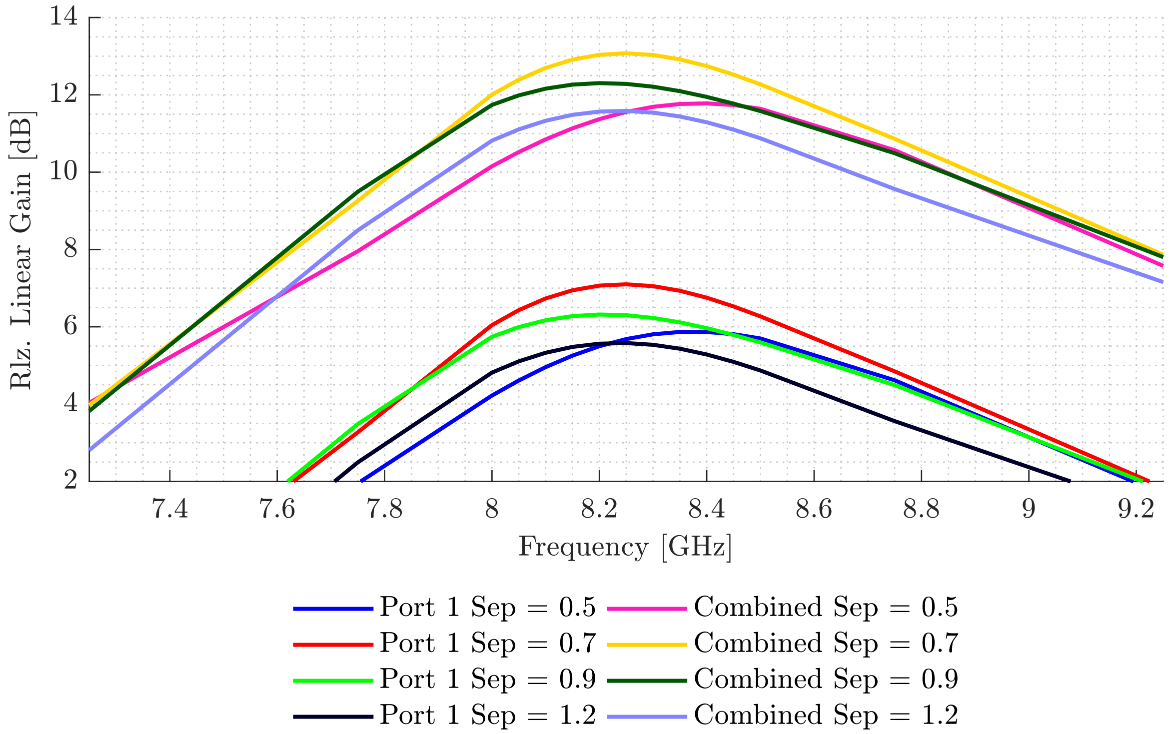

Figure E.2: Simulated broadside realized linear gain of the linear combined antenna array with different antenna seperation distances.

Figure E.3 shows the simulated S_{11} parameter of the antenna array seen in Figure E.9a with different antenna separations. The plot show both the S_{11} of a single port of the array and the combined array. The simulation shows that the antenna separation distance also effects the return loss of the antenna array.

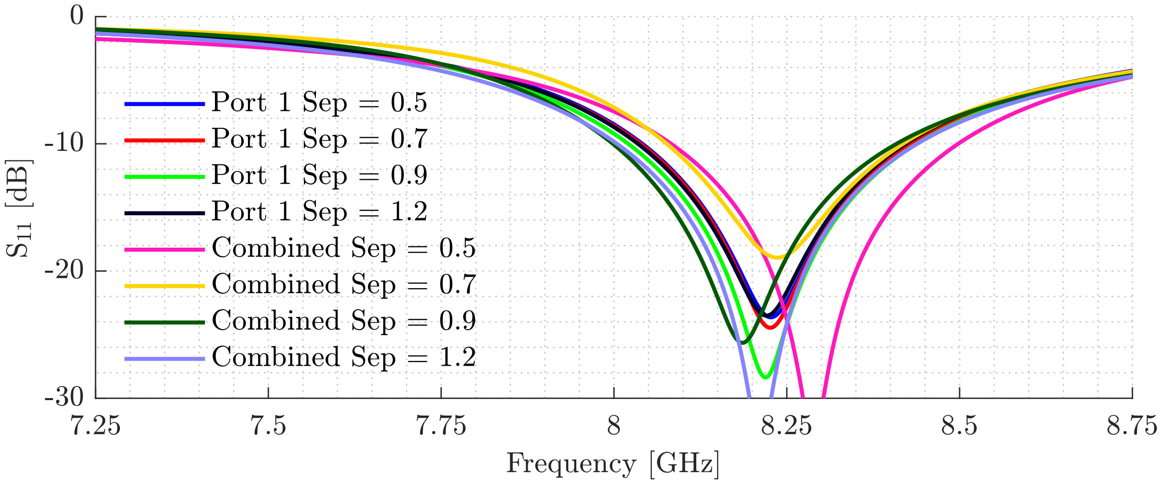

Figure E.3: Simulated S_{11} paramenter of the antenna array with different antenna separations.

From the simulation results it is observed that coupling is highest between opposite antennas. Figure E.4 shows the cross-coupling between element one and its opposite element (S_{21}) with different antenna separations. It is observed that a higher antenna separation causes a lower coupling.

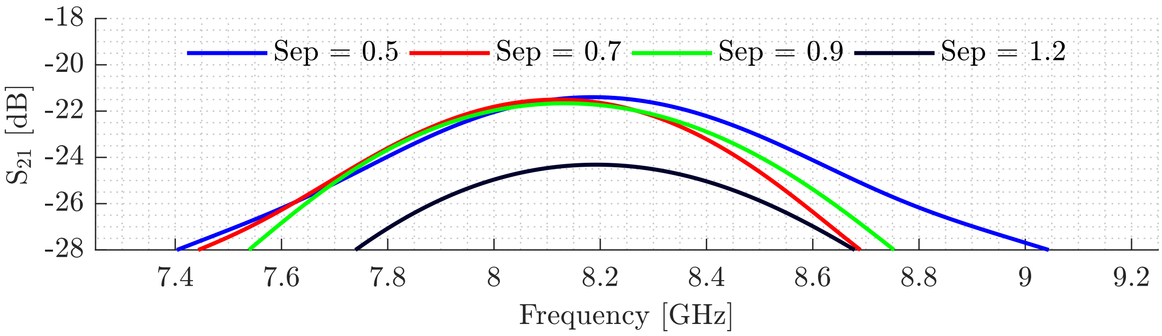

Figure E.4: Simulated S_{21} of the linear antenna array with different antenna separations.

Figure E.5 shows the simulated radiation patterns of the antenna array with the four different antenna separation distances. The figure shows how the antenna separation distance is effecting the radiation patten shape.

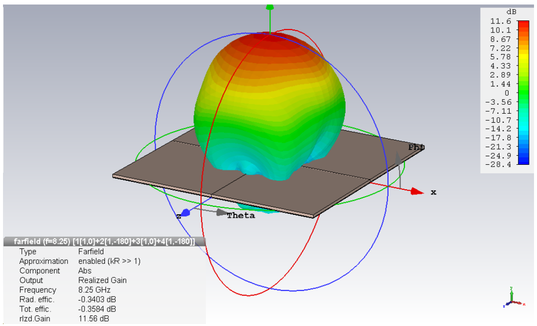

(a) Simulated radiation pattern of the antenna array with a seperation of $0.5 \cdot \lambda$.

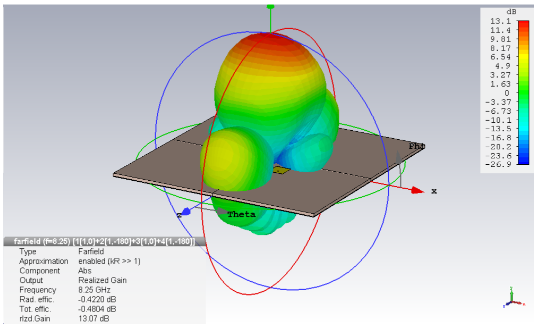

(b) Simulated radiation pattern of the antenna array with a seperation of $0.7 \cdot \lambda$.

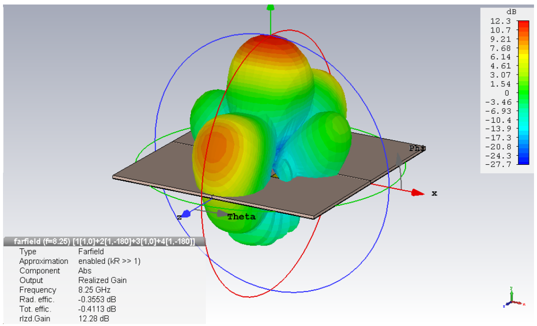

(c) Simulated radiation pattern of the antenna array with a seperation of $0.9 \cdot \lambda$.

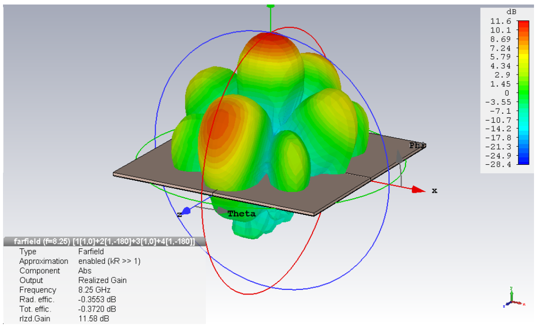

(d) Simulated radiation pattern of the antenna array with a seperation of $1.2 \cdot \lambda$.

Figure E.5: Simulated radiation patterns of the linear antenna array.

Figure E.6 shows the $\phi = 90°$ slices of the radiation patterns seen in Figure E.5. The antenna arrays with antenna separation higher than $0.5 \cdot \lambda$ separation has side-lobes. Increasing the antenna separation results in stronger side-lobes.

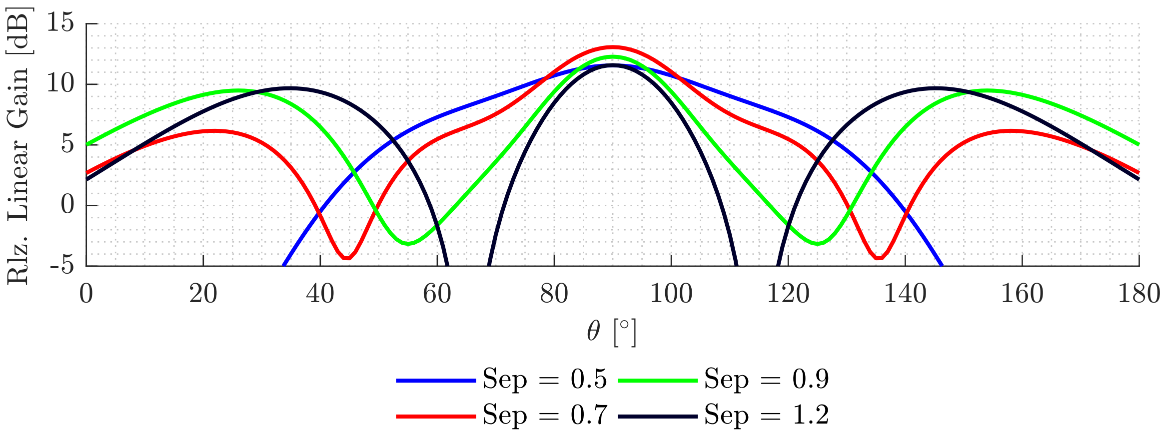

Figure E.6: $\phi = 90°$ slice of the radiation patterns seen in Figure E.5.

As seen from the simulations, the best center to center distance in the array is approximately 25.5 mm, which is roughly $0.7 \cdot \lambda$. Figure E.7 shows a comparison of the radiation patterns of a single element and a two-by-two array. Figure E.7a shows that the single element has a maximum realized gain of 7.05 dB, while Figure E.7b shows that the array has a gain of 13.1 dB. Thus the antenna array has an array factor gain of approximately 6 dB.

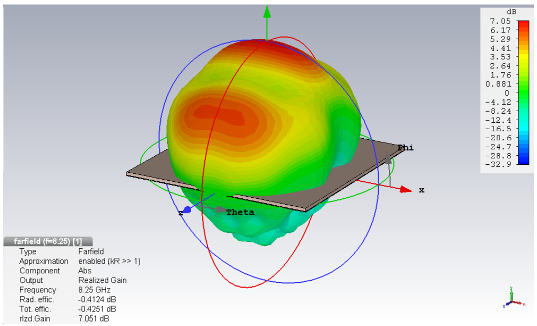

(a) Simulated radiation pattern of the Single linear patch seen in Figure E.9a.

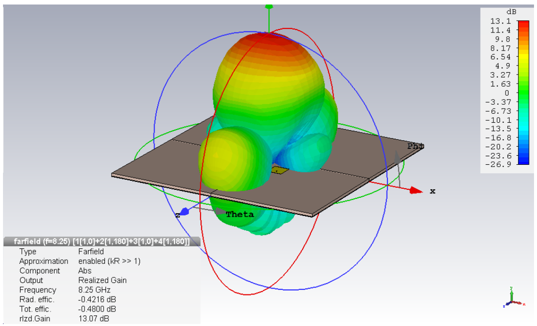

(b) Simulated radiation pattern of the two-by-two linear patch antenna array seen in Figure E.9b.

Figure E.7: Radiation patterns for a single patch and for an array of four patches.

Figure E.8 shows the broadside realized gain of the the single linear patch antenna seen in Figure E.9a. It also shows the realized gain of port 1 alone and the combined realized gain of the linear antenna array seen in Figure E.9a.

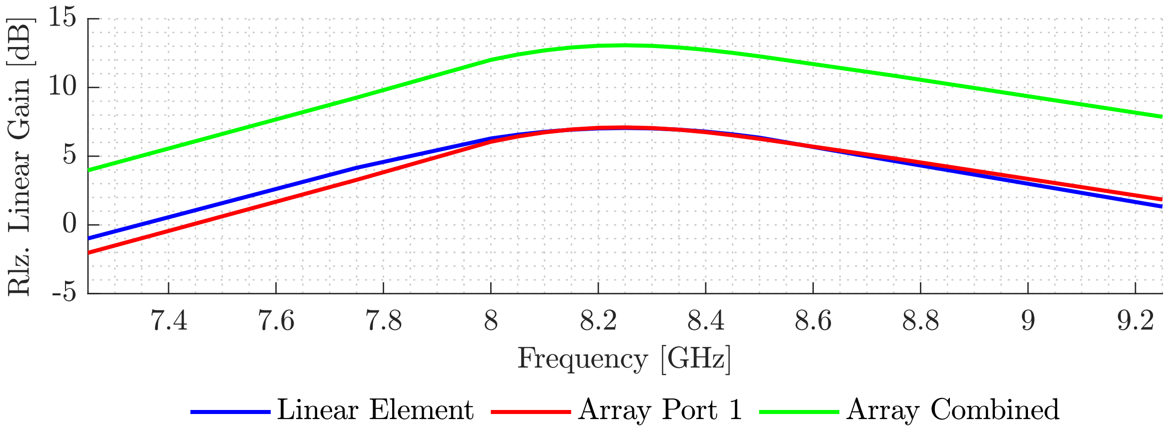

Figure E.8: Simulated broadside realized gain of a linear antenna array, a single array element, and an isolated patch antenna.

LINEAR PATCHES COMBINED TO ACHIEVE CIRCULAR POLARISATION

Linear antenna elements can also be used to achieve circular polarization. If the antennas seen in Figure E.1a is arranged as seen Figure E.9b, the array can achieve circular polarization. To achieve RHCP, the antennas must be feed with a $-90°$ phase shift in the counterclockwise direction.

Antenna element 1 and 2 are the two rightmost antenna elements. These two antennas combined can achieve circular polarisation if the topmost of the two antennas is exited with a $-90°$ phase shift. If the remaining two antennas are exited in a similar manner they contribute to a higher circular polarized gain.

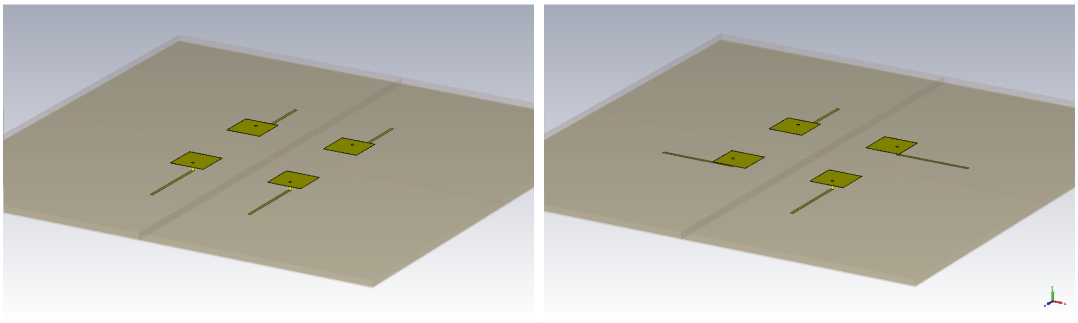

(a) Linear polarized 2-by-2 array.

(b) Circular polarized array made with linear patch antenna elements.

Figure E.9: Two different arrangements of linear patch antenna elements in an array.

Figure E.10a shows the simulated radiation pattern of the antenna array with port 1 and 2 exited to achieve circular polarization. The plot shows that the combination of the two ports achieves RHCP with a realized gain of $\geq 7.35\,\text{dB}$ in the Y direction. However, the maximum of gain are to be found at a slightly shifted direction.

Figure E.10b shows the resulting antenna radiation pattern when combining all four antenna elements. The figure shows that the antenna array achieves a realized RHCP gain of $10.4\,\text{dB}$.

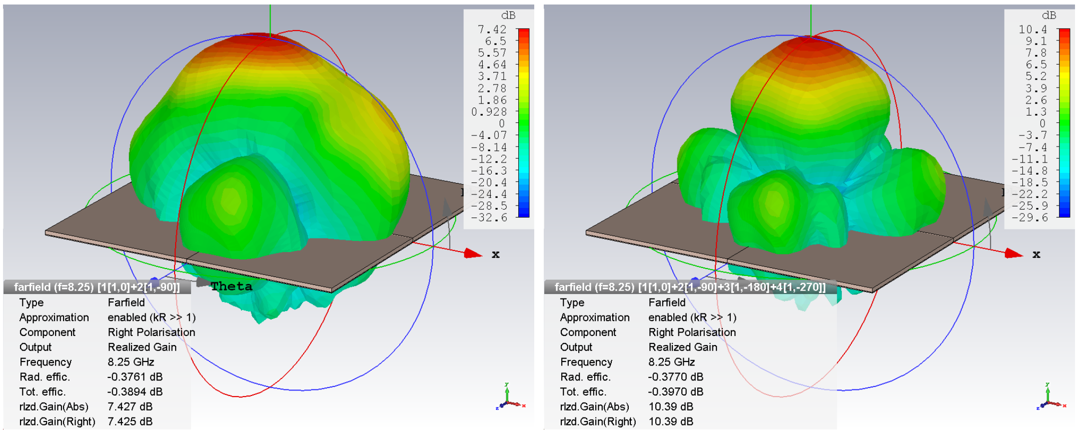

(a) Radiation pattern of the combination of port 1 and 2 of the antenna array seen in Figure E.9b.

(b) Radiation pattern of the fully combined antenna seen in Figure E.9b.

Figure E.10: Simulated radiation patterns.

Figure E.11 shows a plot of the frequency dependent gain of the different excitation options for the antenna seen in Figure E.9b. The first line is the realized linear polarized gain of Port 1 of the antenna array. The second line is the resulting realized RHCP gain of the combination of port 1 and 2. The third line is the resulting realized RHCP gain of the combination of all four antenna ports.

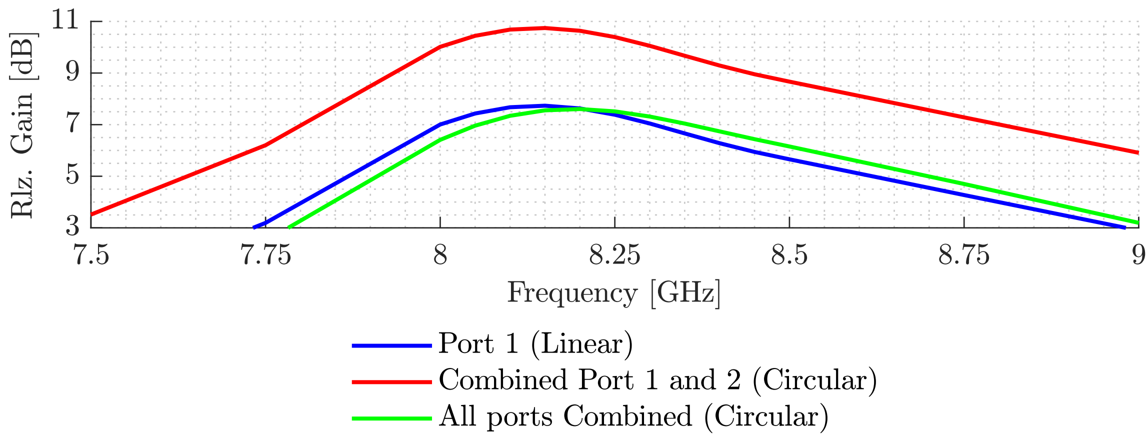

Figure E.11: Simulated broadside gain of the different combination options for the antenna seen in Figure E.9b.

CIRCULAR PATCHES COMBINED TO HAVE A CIRCULAR GAIN

Arrays can also be made from circular polarized patches to improve the circular gain. The patch seen in Figure E.1b is used in the two arrays seen in Figure E.12. With the array seen in Figure E.12a the optimal antenna element separation was found to be equivalent to that of the linear array, 25.5 mm. For the array seen in Figure E.12b, the optimal separation between the opposite arranged patches is found to be 32.75 mm, which is approximately $0.9\,\lambda$.

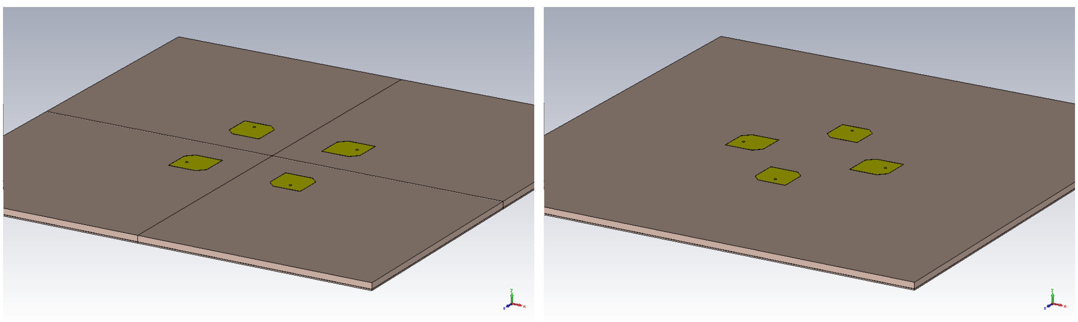

(a) Square array arrangement of a two-by-two antenna array.

(b) Cross arrangement of a two-by-two antenna array.

Figure E.12: Two different antenna array arrangements.

Figure E.13 shows the simulated radiation pattern of the two circular arrays seen in Figure E.12. It is observed from the figure that the position of the side-lobes is the main difference between the radiation patterns.

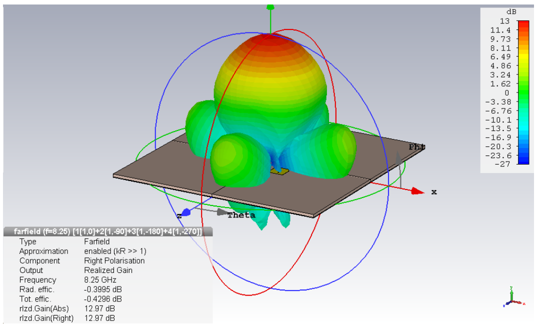

(a) Radiation pattern for the square arranged configuration.

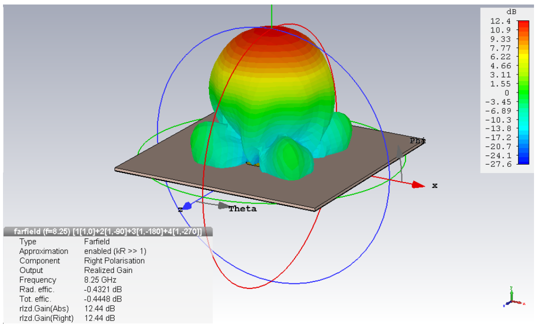

(b) Radiation pattern for the diamond arranged configuration.

Figure E.13: Simulated radiation patterns for the circular polarized patch antenna array.

Figure E.14 shows the broadside realized RHCP gain of the two arrays made from circular polarized patch antennas.

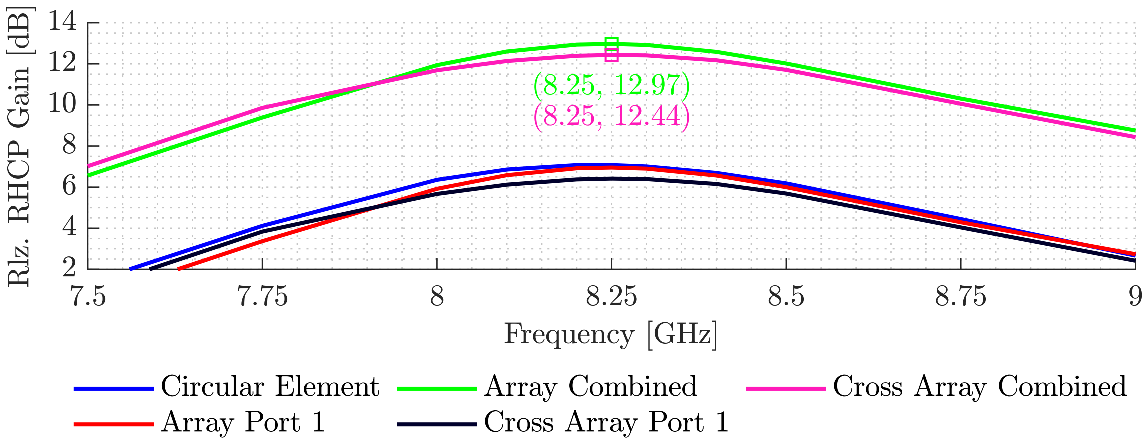

Figure E.14: Simulated broadside realized RHCP gain of the two arrays made from circular polarized patch antennas.

F X-BAND PATCH ANTENNA WITH DIFFERENT GROUND PLANES SIZES

The dimensions of a patch antenna is listed in Table F.1.

Table F.1: Dimensions of the a patch antenna.

Patch Polarization	Linear
Substrate	RO4003C
Substrate Height (Under Patch)	1.524
Substrate Height (Feeding side)	0.305
Copper Height	0.035
Patch Length	8.6
Patch Width	8.6
Feeding point Z-axis	1.5
Feeding point X-axis	-
Feed line Width	0.7
Feed Pin radius	0.35
Ground Cut out Radius	0.9
Feed Line length	10

Figure F.1 shows the simulated S_{11} parameter of the patch antenna with different ground plane sizes.

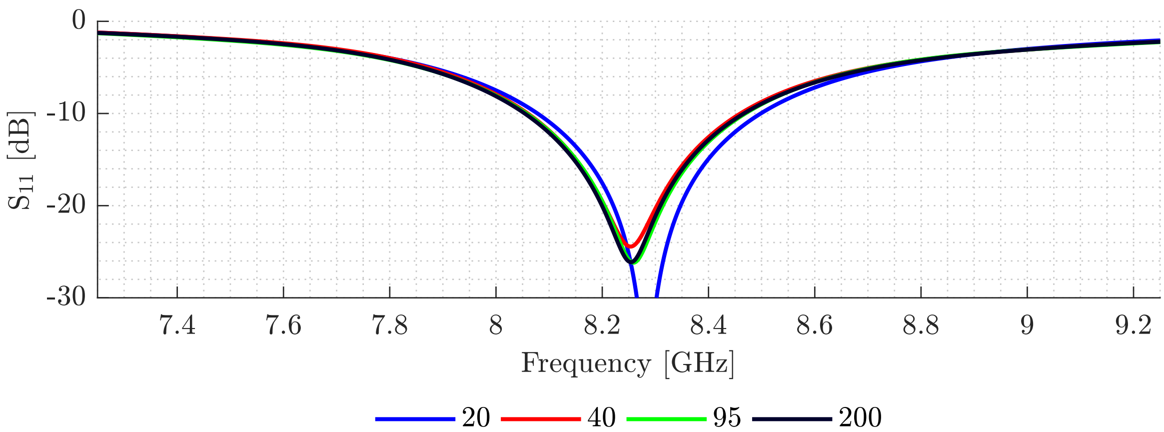

Figure F.1: Simulated S_{11} for a patch antenna with different ground plane sizes.

Figure F.2 shows the broadside realized gain of the patch antenna with different ground plane sizes.

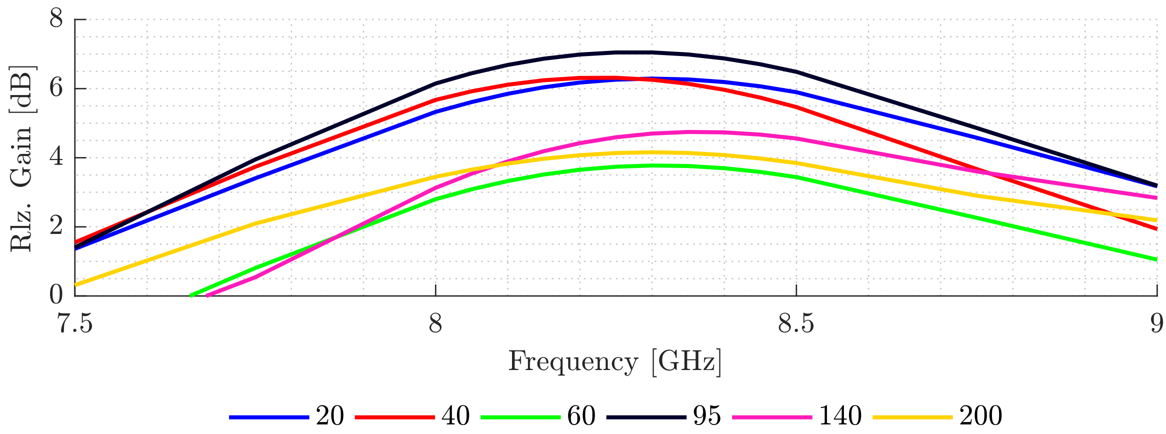

Figure F.2: Simulated broadside realized gain for the linear patch antenna with different ground plane sizes.

Figures F.3 and F.4 show the simulated radiation pattern of the patch antenna with four different ground plane sizes.

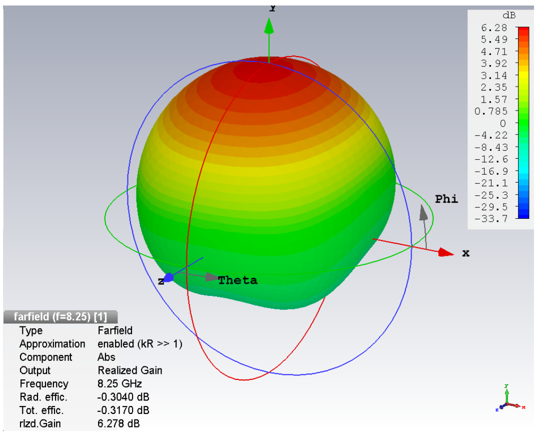

(a) Radiation pattern for the linear patch antenna with a 20 mm ground plane.

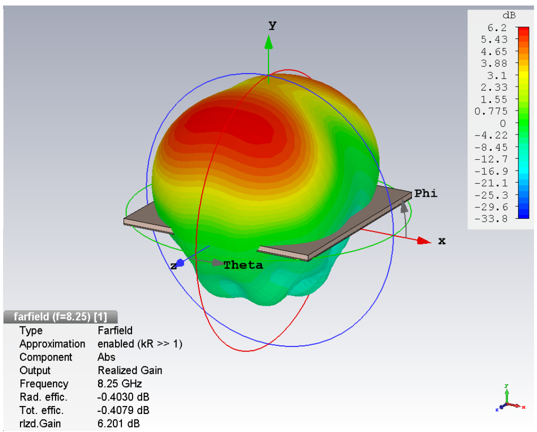

(b) Radiation pattern for the linear patch antenna with a 60 mm ground plane.

Figure F.3: Simulated radiation patters of the linear patch antenna with two different ground plane sizes.

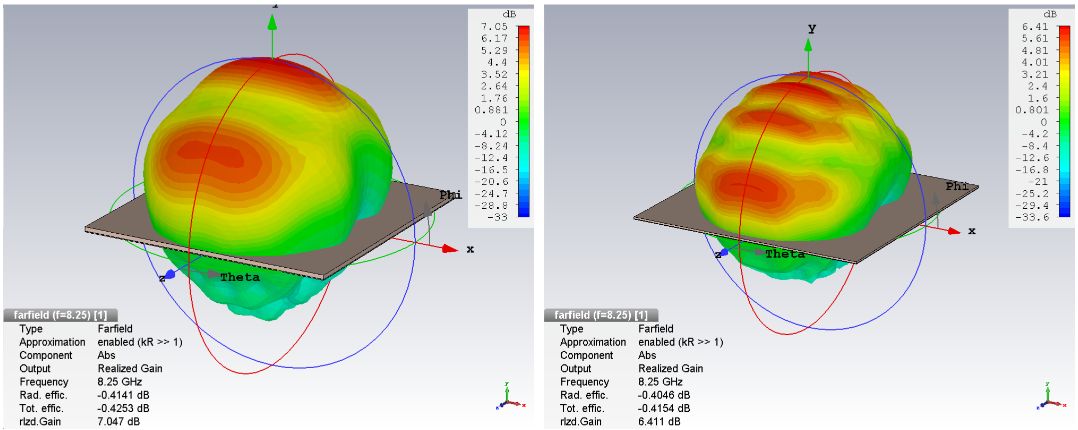

(a) Radiation pattern for the linear patch antenna with a 95 mm ground plane.

(b) Radiation pattern for the linear patch antenna with a 200 mm ground plane.

Figure F.4: Simulated radiation patters of the linear patch antenna with two different ground plane sizes.

Figure F.5 shows the broadside realized gain at 8.25 GHz, dependent on the ground plane size.

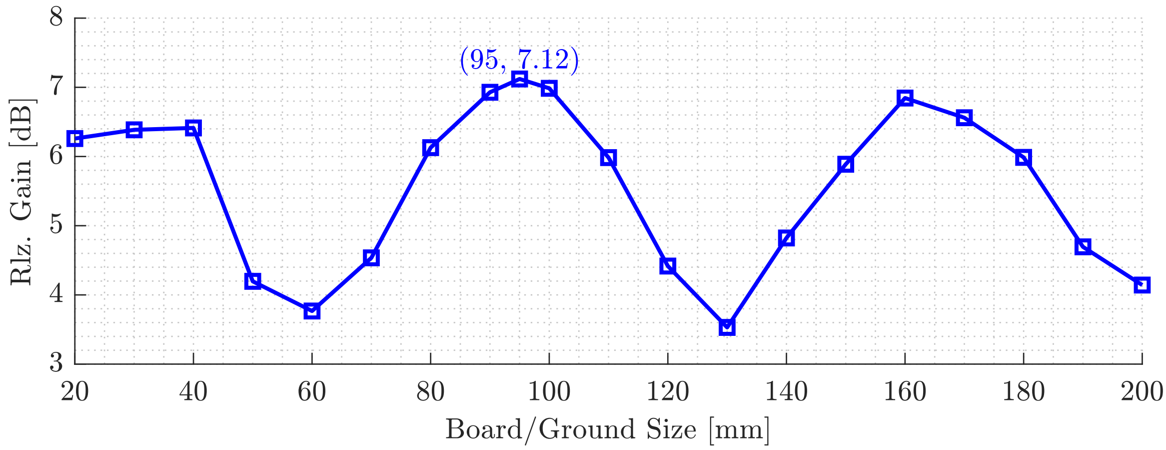

Figure F.5: Broadside realized gain of the patch antenna with different ground plane sizes.

Figure F.6 shows the $\phi = 90°$ slice of the patch at 8.25 GHz with different ground plane sizes.

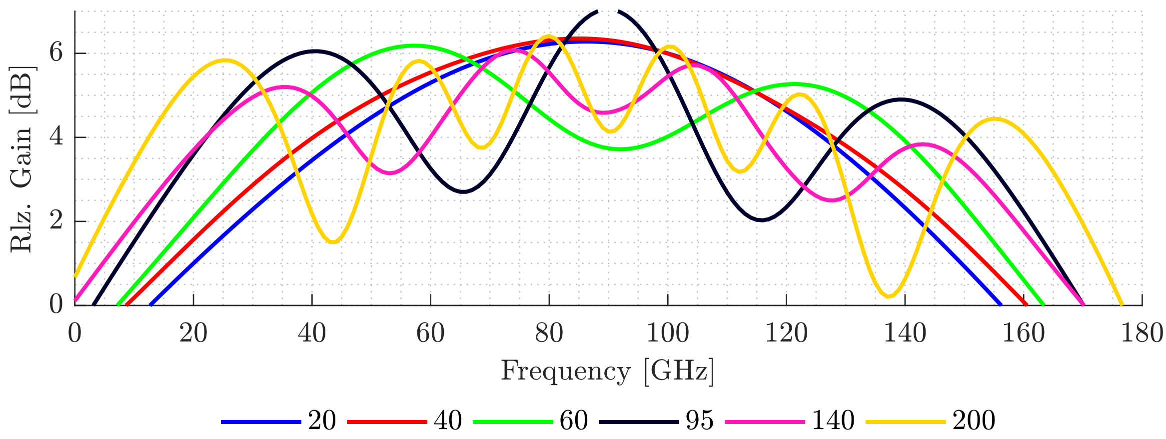

Figure F.6: $\phi = 90°$ slice of the patch at 8.25 GHz with different ground plane sizes.

CONCLUSION

It is clear from this appendix that the size of the ground plane is very important for the performance of a patch antenna.

If the ground plane becomes to large the radiation pattern shape becomes different. If the ground plane in increased beyond approximately 40 mm, with this substrate configuration, the expected directional tear drop pattern is not dominant any more.

If the ground plane is enlarged to 95 mm the broadside gain will reach its maximum. This however comes at the expense of a much narrower main-beam strong side-lobes.

G GUIDED X-BAND PATCH ANTENNA

The purpose of this appendix is to investigate the possibilities of guiding the radiation of a patch antenna on a large ground plane. As seen from Appendix F a X-band patch antennas on 60 mm ground plane has a low broadside realized gain causes by an unwanted radiation pattern shape.

This appendix shows the effect of adding ground metal guides around a patch antenna.

Figure G.1 shows a patch antenna on a 60 mm square ground plane and a patch antenna with "guides" along the edge of the substrate.

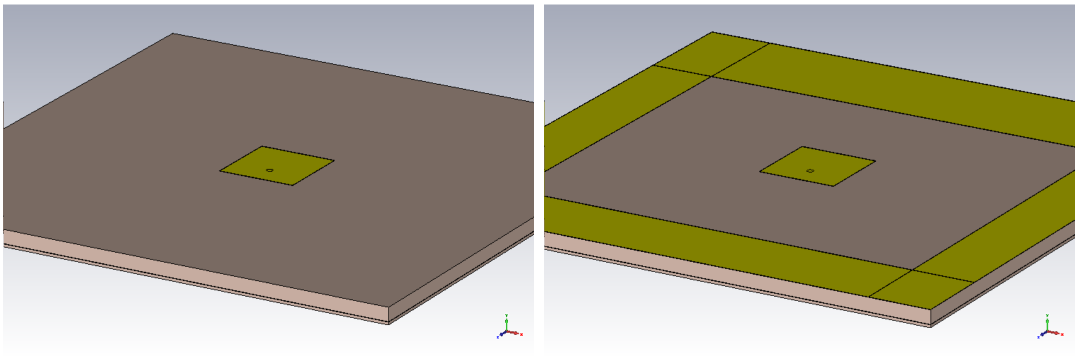

(a) Patch antenna on a 60 mm ground plane.

(b) Patch antenna on a 60 mm ground plane guided by side guides.

Figure G.1: CST models of a path antenna with and without ground guides at the board edges.

Figure G.2 shows the simulated 8.25 GHz radiation pattern of two antennas seen in Figure G.1.

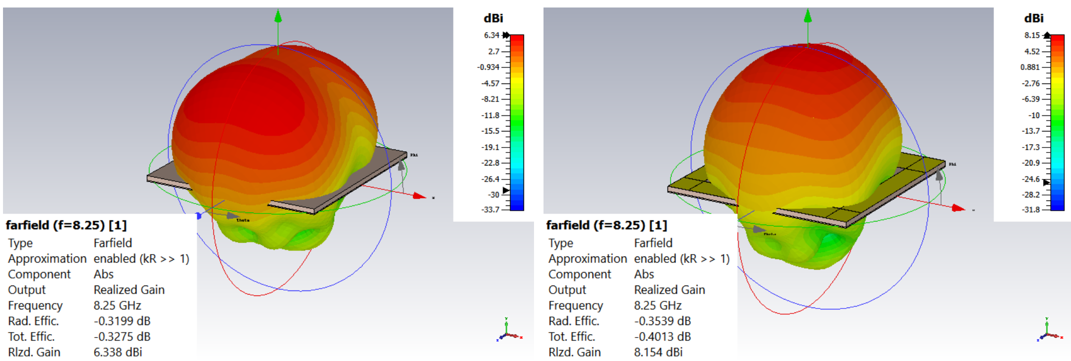

(a) Radiation pattern of the patch antenna on a 60 mm ground plane.

(b) Radiation pattern of the patch antenna guided by the side guides.

Figure G.2: Simulated radiation pattern of the two patch antennas.

Figure G.3 shows the broadside realized gain of the patch antennas with and without the guide.

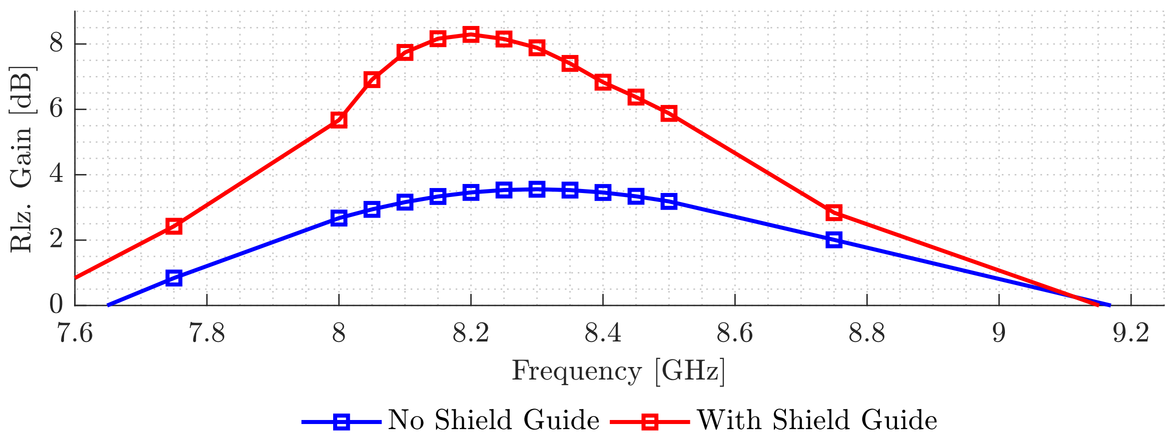

Figure G.3: Simulated broadside realized gain for the two patch antennas.

Figure G.4 shows the $\phi = 90°$ slice of the radiation pattern of the two patch antennas. From the figure it is clearly seen for the edge guided patch antenna is more directional.

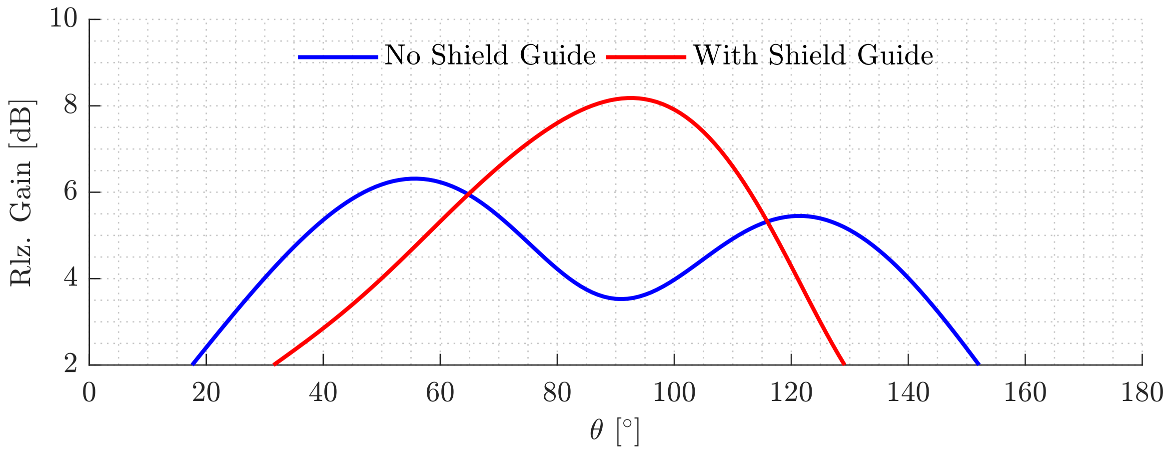

Figure G.4: Simulated $\phi = 90°$ realized gain slice for the two patch antennas.

The performance of the guided patch antennas is significantly better than that of the non-guided patch antenna. The guided patch antenna has a radiation pattern of the desired shape and therefore has a significantly higher gain.